TU Delft

Delft University of Technology

Acoustic and Electromagnetic Waves in MRI

Novel Strategies for Acoustic Noise Reduction, Transmit Field Characterization and Correction

Šiurytė, P.

DOI
10.4233/uuid:4cd8124b-ef3e-4e1e-8271-28899f149b18

Publication date
2025

Document Version
Final published version

Citation (APA)
Šiurytė, P. (2025). *Acoustic and Electromagnetic Waves in MRI: Novel Strategies for Acoustic Noise Reduction, Transmit Field Characterization and Correction*. [Dissertation (TU Delft), Delft University of Technology]. https://doi.org/10.4233/uuid:4cd8124b-ef3e-4e1e-8271-28899f149b18

Important note
To cite this publication, please use the final published version (if applicable).
Please check the document version above.

Copyright
Other than for strictly personal use, it is not permitted to download, forward or distribute the text or part of it, without the consent of the author(s) and/or copyright holder(s), unless the work is under an open content license such as Creative Commons.

Takedown policy
Please contact us and provide details if you believe this document breaches copyrights.
We will remove access to the work immediately and investigate your claim.

This work is downloaded from Delft University of Technology.
For technical reasons the number of authors shown on this cover page is limited to a maximum of 10.

Acoustic and Electromagnetic Waves in MRI

Novel Strategies for Acoustic Noise Reduction, Transmit Field Characterization and Correction

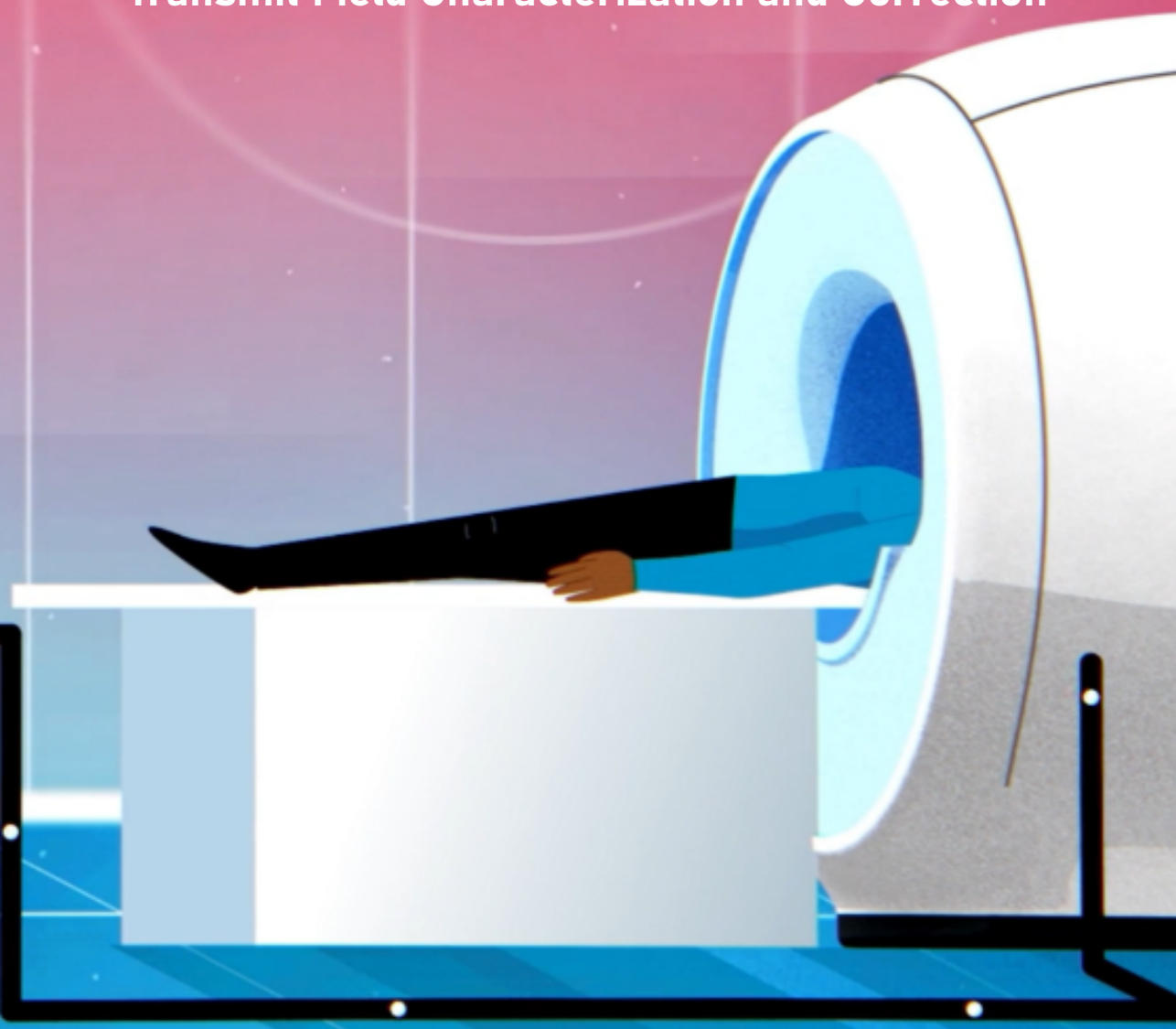

Paulina Šiurytė

Acoustic and Electromagnetic Waves in MRI

Novel Strategies for Acoustic Noise Reduction, Transmit Field Characterization and Correction

Acoustic and Electromagnetic Waves in MRI

Novel Strategies for Acoustic Noise Reduction, Transmit Field Characterization and Correction

Dissertation

for the purpose of obtaining the degree of doctor
at Delft University of Technology
by the authority of the Rector Magnificus,
prof. dr. ir. T.H.J.J. van der Hagen,
chair of the Board for Doctorates
to be defended publicly on
Thursday 9th, January 2025 at 10:00 o'clock

by

Paulina ŠIURYTĖ

Master of Science in Physics,
University of Surrey, United Kingdom
born in Jonava, Lithuania

This dissertation has been approved by the promotors.

Composition of the doctoral committee:

Prof. dr. ir. A.W. Heemink,	chairperson
Prof. dr. F.M. Vos,	Delft University of Technology, *promotor*
Dr. S. Weingärtner,	Delft University of Technology, *copromotor*
Independent members:	
Prof. dr. A. Webb	Delft University of Technology
Prof. dr. L. Wald	Harvard Medical School and Massachusetts General Hospital
Dr. ir. R.F. Remis	Delft University of Technology
Dr. ir. R.F. Remis	Delft University of Technology
Dr. J.C.W. Siero,	University Medical Center Utrecht
Prof. dr. S. Stallinga,	Delft University of Technology, reserve member
Other members:	
Dr. T.M. Correia,	The Algarve Centre of Marine Sciences

Keywords: MRI physics, MRI acoustic noise, RF field inhomogeneity, electrical properties

Printed by: ADC Nederland.

Cover by: Life Science Animation.

Copyright © 2024 by P. Šiurytė

ISBN 978-94-6366-998-6

An electronic copy of this dissertation is available at https://repository.tudelft.nl/.

CONTENTS

SUMMARY

Magnetic Resonance Imaging (MRI) is increasingly applied at high magnetic field strengths of 3T and above. This trend aids in achieving superior image quality, accelerated scan times, and enhanced diagnostic capabilities. However, the increased magnetic field strengths also amplify the acoustic and electromagnetic field interactions during MRI. This presents considerable challenges for comfortable and reliable imaging.

Firstly, the acoustic noise at high magnetic field strength MRI is greatly exacerbated. The sound may reach up to 130 dB, greatly exceeding the safe prolonged noise exposure limit at 90 dB. This causes anxiety in patients, elevate claustrophobic reactions, and are even associated with increased scan refusal rates. The sound pressure levels at modern scanners generally exceed the public safety threshold. Thus, if not adequately accounted for, it bears the risk of temporary or permanent hearing damage.

Secondly, achieving a homogeneous distribution of the transmitted radiofrequency (RF) field, which is used to create the magnetization signal, becomes increasingly challenging at high magnetic fields. The degree of constructive and destructive interference of the RF field components becomes exacerbated as the RF field wavelength shortens and starts to approximate the body dimensions in tissue. This results in spatial signal variation that cannot be universally predetermined, which can hinder diagnostic assessment in clinical imaging.

In this thesis, multiple challenges of high-field MRI were tackled by developing advanced devices and MR scanning methodologies. Firstly, a solution to the acoustic noise problem was proposed based on predicting the scanner sound and superimposing its anti-noise to reduce the sound pressure. The results indicate robust noise reduction of up to 13 dB with a proof-or-principle system across various scanning methods.

To tackle the transmitted field B_1^+ inhomogeneity, an adaptive shimming device was proposed, based on an array of electrically-coupled pads with high permittivity. Based on electromagnetic field simulations, the device prototype was constructed. Up to 11% modulation was measured in phantoms at 15 mm depth, with an ability to tune the location of shimming hotspot.

A novel scanning methodology to quantify B_1^+ magnitude in the heart was developed, using Bloch-Siegert shift-based preparations. The sequence has shown highly-robust 2D and 3D mapping in healthy subjects,

and achieved superior noise-resilience, when compared to more established mapping methods.

The proposed novel B_1^+ mapping sequence was then adapted to enable conductivity mapping in the myocardium. The method provided the first complex B_1^+ field-based conductivity reconstruction in healthy subjects, with robust results in agreement with previous literature.

Finally, another MRI scanning methodology was proposed for quantitative cardiac imaging robust to field inhomogeneities. T_2^* - a common biomarker used in MRI - was reconstructed using phase-cycled preparations. Compared to conventional sequence, higher noise resilience was achieved in healthy subjects, while enabling a wider range of sequence tailoring options.

1

INTRODUCTION

1

Almost 100 million Magnetic Resonance Imaging (MRI) scans are performed each year worldwide [1]. MRI is a safe and radiation-free imaging modality with excellent soft tissue contrast. Common target anatomies include the brain, musculoskeletal system, heart, and liver. MRI enables the acquisition of detailed anatomical images, providing structural and functional information, stemming from the nuclear spin relaxation properties, tissue, perfusion, diffusion, oxygenation levels, certain metabolite concentrations, or other contrast mechanisms. The versatility of possible MRI applications has resulted in its wide use in medical imaging for diagnostic purposes.

Over the past 4 decades, steady advances in MRI methodologies and engineering have brought about a revolution in image quality. To benefit from stronger polarization, induction and increased tissue contrast, a move to higher main magnetic fields has been a central component of these developments. Despite the advantage of the overall higher signal-to-noise ratio (SNR), this also comes with a range of challenges and disadvantages for MRI.

One of these disadvantages is the exposure to extremely high levels of acoustic noise during imaging. Clinically used 3T systems, for instance, may reach up to 130 dB, a sound pressure level (SPL) equivalent to the sound exposure of jet engine at short distance [2, 3]. With shorter system switching times and increasing main magnetic fields, the sound problem only exacerbates, leading to increased sound exposure in many modern systems. While this can be partially alleviated by hearing protection like earplugs, the deafening noise is a major contributor to high rates of patient anxiety and poses a risk of shifting the hearing threshold [4, 5].

Another issue arises due to exacerbated magnetic field imperfections at increased magnetic field strengths. The transmitted radiofrequency (RF) field inhomogeneity is particularly prominent in high-field MRI, resulting from the shortened RF field wavelength in tissue. As it approaches the order of body dimensions, the areas of constructive and destructive interference of the RF field components become exacerbated. This leads to skewed contrast due to uneven excitation across the imaging volume [6, 7]. For instance, body imaging at 3T suffers from up to 50% transmitted signal variation [8]. As a result, the task of acquiring artifact-free images becomes more difficult, hindering diagnostic accuracy. Therefore, the quantification and correction of the RF field in MRI (also referred to as B_1^+ field) with increased magnetic field strengths is essential.

1.1. RESEARCH GOALS AND THESIS OUTLINE

In this thesis, we explore novel solutions to shortcomings relating to both acoustic and electromagnetic wave fields that are encountered in

modern MRI. To provide substantial technical background, this chapter first briefly introduces the basic concepts of MRI. In addition, the origins of the acoustic and electromagnetic interactions in MRI are described, to provide the foundation for the methods and experiments described in the remainder of the thesis.

Following the introduction, the thesis is divided into two parts: hardware-based solutions and MRI pulse sequence design. Hardware-based solutions, described in Chapters 2 and 3, investigate possible add-on devices to mitigate the problems of excessive acoustic noise and RF inhomogeneity, without directly adjusting the MRI scanning procedure. In contrast, pulse sequence design solutions (Chapters 4-7) are direct alterations to the imaging methods.

The first hardware-based solution, described in Chapter 2, tackles acoustic noise. The goal of this was to develop a cost-efficient and universal way to reduce the noise of any MRI scanning procedure. Acoustic noise, originating in the constituent scanner hardware, was modeled for sound pressure wave prediction at a defined location within the scanner bore. The original noise was then superimposed with the prediction anti-noise via a MRI-compatible headphone prototype, to achieve live cancellation of the original scanner noise.

Another hardware-based solution was developed for mitigating the unwanted B_1^+ field inhomogeneity. Since currently affordable and versatile solutions are lacking, Chapter 3 explores the possibility of adaptive B_1^+ shimming by electrically coupling an array of small dielectric pads. Although the equivalent passive pouches with high permittivity are common in clinical applications, the possibility of remote switching between different shimming modes was explored to enhance the flexibility of such techniques.

Part II of this thesis is prefaced with an extended review of the emerging cardiac magnetic resonance (CMR) tissue characterization methods (Chapter 4). The goal of this chapter is to familiarize the reader with modern quantitative MRI approaches in, arguably, one of the most challenging anatomies. As an extension, this also lays further theoretical groundwork for pulse sequence design.

In order to measure B_1^+ field distribution during imaging in MRI, B_1^+ mapping methods are indispensable. A wide range of MRI pulse sequence methods have been developed for B_1^+ mapping, however, in the heart, the motion due to the respiration and cardiac contraction are ever-present. As a result, few methods are suitable for cardiac B_1^+ mapping. To diversify the available techniques, the next research goal was to design a robust B_1^+ mapping sequence and to evaluate it in phantom and in vivo experiments. The developed sequence is described in detail and evaluated in Chapter 5.

The goal of Chapter 6 was to adapt the proposed B_1^+ mapping sequence to enable the reconstruction of cardiac electrical properties

(EPs). To this end, electrical properties tomography (EPT) was performed. This technique uses the spatial distribution of the RF field within tissue in order to extract the electrical permittivity and conductivity. EPs are valuable biomarkers used in brain or breast imaging to detect and categorize cancer development [9], however, cardiac applications remain highly limited [10]. The chapter presents the results of the conductivity value reconstruction in saline phantom and in the myocardium of healthy subjects.

Chapter 7 presents another novel pulse sequence, designed for quantitative T_2^* mapping robust to magnetic field inhomogeneities. T_2^* is one of the nuclear spin relaxation properties and describes the rate of nuclear spin phase coherence loss following an excitation using the RF field. It can be used as a valuable biomarker to assess myocardial iron levels. In the current work, T_2^* was quantified and compared to a conventional method. The T_2^* mapping sequence was presented and evaluated in healthy subjects.

Finally, Chapter 8 presents an overall discussion of the achieved results, research impact and possible future directions.

1.2. NUCLEAR MAGNETIC RESONANCE

The signal in MR imaging originates from the nuclear magnetic resonance (NMR) phenomenon. Non-zero intrinsic spins of the atomic nuclei give rise to a magnetic moment, primarily described as dipole magnetic moment. In a semi-classical MRI interpretation, the magnetic dipole moments μ of these nuclei align either with or against the direction of the external applied magnetic field B_0 [11]. The magnetic dipole moments precess with a Larmor frequency $\omega_0 = \gamma B_0$, where γ denotes the gyromagnetic ratio of the nucleus. Within a sample volume, the population of spins will result in a net magnetization M_0, oriented along B_0 axis in equilibrium for $\gamma > 0$. For spin s = $\frac{1}{2}$ particles, such as single protons of H_1^1 nuclei:

$$M_0 \approx \frac{N\mu\gamma\hbar B_0}{2kT}, \tag{1.1}$$

where N denotes the number of spins within the sample volume, $\hbar$ the reduced Planck constant, k the Boltzmann constant and T the temperature [12].

To tip M_0 away from equilibrium, MRI utilizes pulsed secondary magnetic field B_1, perpendicular to and rotating around the B_0 axis close to the resonant Larmor frequency $\omega_1 \approx \omega_0$. Since at the typical magnetic field B_0 strengths (1.5 T in the majority clinical scanners [13]) the Larmor frequency falls within the radiofrequency range, the rotating field B_1 is also referred to as the RF field. Notably, the strength of this field is much weaker than B_0 and lies in the order of microtesla. However, when applied at the resonant frequency, B_1 tips the magnetization, which is often quantified by flip angle α between the M_0 and B_0:

$$\alpha = \int_0^\infty \gamma B_1(t) dt \tag{1.2}$$

After the B_1 field is turned off, the tipped net magnetization begins to precess around the axis of the main magnetic field B_0. This, in turn, creates a detectable change in the magnetic field, and can be measured using proximate coils. According to Faraday's law of induction, the changing magnetic flux induces voltage inside wire loops orthogonal to the magnetic field direction, which is used for MRI signal reception. Since only time-varying magnetization can be detected, the received signal is proportional to the transverse magnetization component, perpendicular to the B_0 axis. In turn, the non-precessing longitudinal magnetization component is undetected [11, 12].

In addition to precession, the tipped magnetization immediately begins to relax back to the equilibrium state along the B_0 axis. The relaxation can be described as an exponential process governed by the so-called

relaxation times, with the longitudinal and transverse magnetization components governed by the T_1 and T_2, respectively. As a result of phase decoherence of the precessing magnetization, the transverse component decays faster than the longitudinal component recovers. T_2 times can be further distinguished between the 'true' irreversible phase coherence loss due to spin-spin interactions, and T_2^*, which describes the cumulative, faster relaxation rate due to 'true' T_2, and, additionally, the reversible phase coherence loss due to the minor main magnetic field strength variations across the sample. The resulting MR signal is often modeled as an exponentially decaying sinusoid at a rate governed by T_2^*, and is referred to as a free-induction decay (FID) signal.

1.3. SPATIAL INFORMATION ENCODING

To spatially localize the signal to volume-pixels (voxels) in the acquired image, additional encoding of the received RF signal is required. For this purpose, intrinsic wave properties of frequency and phase are utilized. If a spatially-varying perturbation to the homogeneous B_0 field is created, the Larmor frequency, in turn, becomes modulated within the imaging area. The prescribed B_0 perturbations in MRI are called gradient fields. Linear variations along X/Y/Z spatial directions are commonly used, either individually or in combination in order to achieve oblique imaging orientations.

By creating a predictable magnetic field perturbation during the acquisition, the received MR signal origin location can be traced based on its frequency. This is achieved by performing signal Fourier Transform to deduce the magnitude of each frequency component. Similarly, the signal phase can be used as a second mechanism to encode spatial information in the received MR signal. When applied temporarily prior to the signal acquisition, gradient-induced shifts in Larmor frequency result in variation of the cumulated phase of the rotating magnetization transverse component. When sampled at various gradient field strengths, the signal phase cumulation rate can also be assessed via Fourier Transform. This helps to match the phase dynamics to the prescribed gradient field point location. In MR imaging, frequency and phase encoding are combined, using multiple phase-encoding repetitions sampled at various gradient strengths. The reconstruction of the resulting signal is then performed via 2D Fourier transform.

1.4. PULSE SEQUENCES

MR image acquisition design is defined by pulse sequences - time-series consisting of X/Y/Z magnetic field gradient strengths ($g_{X/Y/Z}(t)$), transmitted RF pulses and signal acquisition time windows. In general, pulse sequences could be described in terms of the following elements:

1. **Magnetization preparation.** This step employs various RF and gradient pulses prior to the main excitation, in order to manipulate the magnetization by, for instance, imposing a weighting to chosen variables, such as the relaxation rates. While magnetization preparation is not an obligatory step for MR imaging, it opens up an array of applications that cannot be offered by the excitation and readout alone.

2. **Excitation.** An integral part of an MRI pulse sequence, an excitation RF pulse tips the net magnetization away from the equilibrium along B_0 direction. This step is generally performed simultaneously with gradients orthogonal to the imaging plane (e.g. $g_Z(t)$), to selectively excite only a slice/volume of interest.

3. **Readout.** After the excitation, the resulting FID signal is manipulated with gradients to phase-encode spatial information (e.g. $g_Y(t)$). Optionally, other RF or gradient pulses are added to impose specific contrast mechanisms. This is followed by the readout - acquisition of the emitted signal in receive coils. This step is performed with frequency encoding gradients (e.g. $g_X(t)$).

The excitation and readout form a basic MRI sequence unit, with excitation-to-readout time defined as echo time (TE) and excitation-to-excitation time as repetition time (TR). An example of a pulse sequence diagram during a single TR is shown in Figure 1.1. A single MRI sequence has numerous TR repetitions to cover the variations of the phase-encoding gradients for image formation [11, 12]. The optional magnetization preparation modules are commonly performed only once prior to a group of TRs.

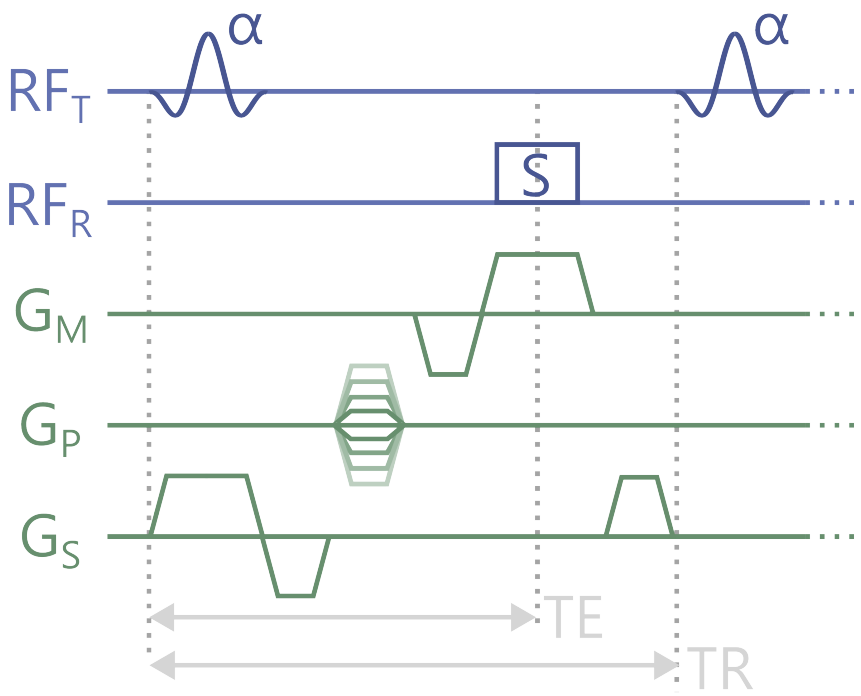

Figure 1.1.: MRI pulse sequence diagram example. The schematic shows a fast gradient-echo (GRE) sequence clip of a single repetition time (TR). The pulse sequence consists of the transmitted RF signal (RF_T) with excitation pulse tipping the magnetization by angle α, the acquisition window to receive the signal S (RF_R) and the gradients G_M (the measurement or frequency-encoding gradient), G_P (phase-encoding gradient) and G_S (slice-encoding gradient). Depending on the chosen imaging slice orientation, the load of M/P/S gradients is attributed to X/Y/Z gradients.

1.5. MRI HARDWARE COMPONENTS

MRI systems generally consist of three integral components: a strong magnet creating the main magnetic field, RF coils for generating the secondary magnetic field and receiving the MR signal, and gradient coils for the spatial modulation of the main magnetic field (See Figure 1.2).

Most clinical MRI systems use a cylindrical superconducting magnet at field strengths of B_0 = 1.5 or 3 T [12], by convention defined to be along the Z axis. At these field strengths, a loss-free magnetic field is enabled by passing an electrical current through superconducting solenoid coils kept below the critical temperature. Typically, this requires cryogenic suspension in liquid helium, and the magnet is permanently operated

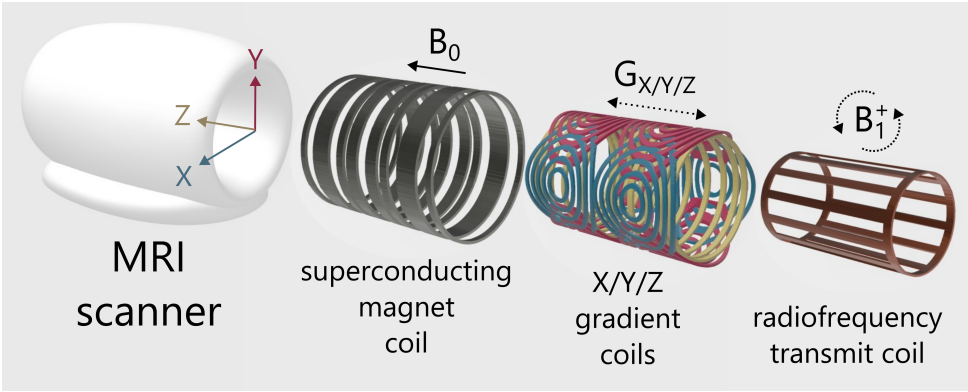

Figure 1.2.: A schematic showing the main hardware components of a typical MRI scanner with a superconducting magnet. The cylindrical housing holds three types of coils: the superconducting magnet coils, creating the main magnetic field B_0; the X/Y/Z gradient coils, creating targeted spatial perturbations in B_0; and the radiofrequency coils, creating the rotating magnetic field B_1, perpendicular to B_0, and receiving the induced MR signal.

after the initial installation.

Unlike the superconducting coils, RF coils are only active during imaging in timed pulses. The principal RF coil (or body coil) is typically positioned in the innermost layer of the cylindrical scanner bore, and can be used both as a transmit and receive coil. In transmit mode, it uses a birdcage design to pass an alternating current in the radiofrequency range. Phase offsets between multiple rungs of this coil create a circularly polarized magnetic field, B_1^+, orthogonal to B_0, and therefore rotating in the X-Y plane. In a receive mode, body coils generally have low sensitivity to the MR signal, and anatomy-specific coils are often appended to enhance either of the two RF coil functions.

Gradient coils are another integral component, used to spatially modulate the magnetic field, and are only active during imaging. They create a small non-rotating magnetic field along the B_0 axis. When superimposed with B_0, the gradient fields create a prescribed (commonly linear) perturbation in B_0 magnitude along one of the three spatial axes: X, Y or Z (See Figure 1.3). The three sets of coils are designed as pairs of either solenoids/Maxwell coils (Z axis) or saddles/Golay coils (X and Y axes) [11, 14]. Modern gradient coils can generate 20-200 mT/m perturbations in the order of (sub)milliseconds. The speed of switching is defined by slew rates - the change in the magnetic field strength per unit time. Switching of the coils results in substantial heat dissipation. To mitigate this, water cooling is utilized. The gradient coils are also subject to alternating Lorentz forces during imaging, creating

audible-frequency oscillations. The oscillations occur primarily along the radial axis, since only coil elements orthogonal to B_0 are subject to the Lorentz forces (see Figure 1.4) [15].

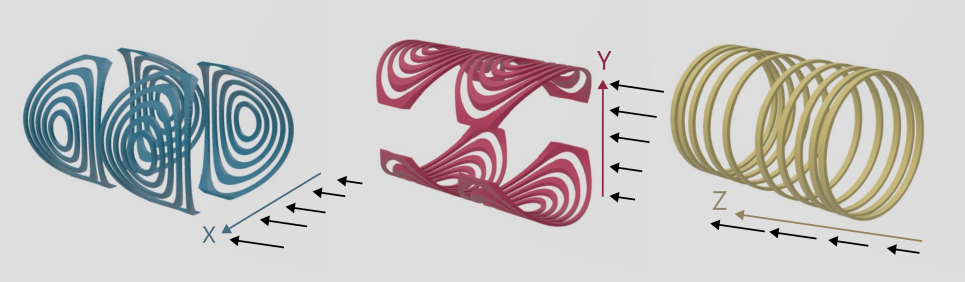

Figure 1.3.: A schematic showing X/Y/Z gradient coils of a typical clinical scanner, and the corresponding perturbed magnetic field (black). X and Y coils are designed as Golay coils, and are orthogonally oriented, while the Z coil uses a Maxwell coil pair. The magnetic fields created by all gradient coils point along or against the main magnetic field B_0 in the Z direction.

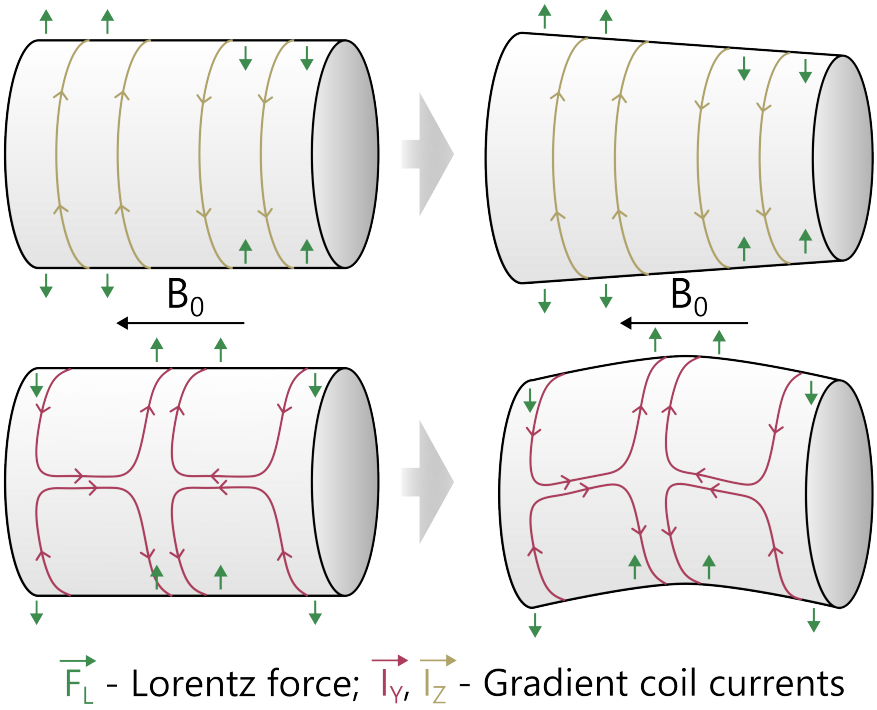

Figure 1.4.: A schematic illustrating two gradient coil vibration modes, when subject to the Lorentz forces (green). The top plots show conical deformation present in the Z coil, while the bottom plots show arching deformation present in X and Y coils (Y coil in the illustration) [16, 17]. As the direction of the gradient coil currents is rapidly switched during imaging, rapid gradient assembly oscillations occur.

1.6. THE ACOUSTICS OF MRI

The loud, jarring noise, along with the enclosed space, are the main factors contributing to patient discomfort during clinical MRI scans [18, 19]. In some cases, it causes extreme anxiety, and may even pose a risk of temporary hearing damage, if not properly accounted for [4, 20–22]. The safe limit for prolonged exposure lies at 90 dB [23], while MRI may reach up to 130 dB at 3T, regulated at 2 minute/day exposure [2, 3]. In the average MRI examination of 15-90 minutes [24], cumulative noise exposure generally exceeds the safety limits, if no additional safety precautions are taken.

The acoustic noise sources in MRI, in the order of increasing loudness, can be listed as: ventilation system, liquid helium pump and gradient coils. The ventilation system produces sound pressure levels (SPL) of

20-30 dB, the helium pump around 70 dB, and while both operate continuously, they are generally considered not bothersome. In contrast, gradient coils, actuated by rapidly switching currents during the pulse sequence execution, produce >100 dB noise (for 1.5-3T scanners) continuously, and are therefore the main source of acoustic noise in MRI [16, 25].

MRI advancement has been trending towards hardware with increased acoustic noise. Stronger static magnetic field B_0 strengths have shown a correlation with louder gradients due to increased Lorentz forces, with the exception of ultra-high fields (7 T and above) where the the increase in loudness is slower due to Lorentz damping [26]. The gradient coil amplifier capabilities have greatly advanced, producing gradients from 3-5 mT/m amplitudes and 3-5 T/m/s slew rates in the early 2000s, to up to 200 mT/m amplitudes and up to 200 T/m/s slew rates today [27]. In the absence of additional improvements in the damping of vibrations present in the gradient assembly, this leads to steep sound pressure level elevation.

MRI gradient sound, resulting directly from the gradient current waveforms, can be modeled as a linear time-invariant (LTI) system [28–32]. The model approximates sound pressure $p(r,t)$ at a given location r within the scanner as a superposition of the individual X/Y/Z gradient coil sound pressure components:

$$\begin{aligned} p(r,t) &= p_X(r,t) + p_Y(r,t) + p_Z(r,t) \\ &= g_X(t)' * h_X(r,t) + g_Y(t)' * h_Y(r,t) + g_Z(t)' * h_Z(r,t), \end{aligned} \tag{1.3}$$

where $g_{X/Y/Z}(t)$' denote the derivatives of the gradient inputs, '$*$' - convolution, and $h_{X/Y/Z}(r,t)$ – the acoustic transfer functions, i.e. the 'fingerprints' of each coil noise. The transfer functions vary greatly with r, subject anatomy or placement. This results in 10-20 dB variation in the total gradient noise inside the scanner [30, 33].

1.7. RADIOFREQUENCY WAVES

While B_1 is used to denote the rotating magnetic field in MRI, it can be separated into two constituent components: the B_1^+ field, rotating in the direction of nuclear precession, and the B_1^- field, rotating in the opposite direction. In this notation, B_1^+ represents the active component responsible for tipping the magnetization, while B_1^- is associated with unwanted losses. Historically, linearly polarized B_1 fields were employed, oscillating along a single axis. This lead to $B_1^+ \approx B_1^- \approx B_1/2$. Modern systems produce circularly polarized B_1 transmission, resulting in minor losses with $B_1^+ \approx B_1$ [11].

Under ideal conditions, a uniform magnetization flip angle during MR excitation is produced within a volume of interest. In practice, this is difficult to achieve, particularly at higher B_0 field strengths, where the wavelength of B_1^+ in tissue starts to approach the body dimensions, forming standing waves [6, 34]. For instance, with the relative permittivity $\epsilon_r = 80$, the wavelength at $B_0 = 1.5$, 3 and 7 T equals 53, 26 and 11 cm, respectively, the latter two comparable to human torso and head dimensions [35]. This leads to spatial variation of the B_1^+ field strength, and, in turn, imaging flip angle. As a result, acquired images often present local signal dropout or hyper-enhancement (See an example of cardiac image at 3T in Figure 1.5). The techniques to optimize the flip angle distribution are referred to as RF shimming.

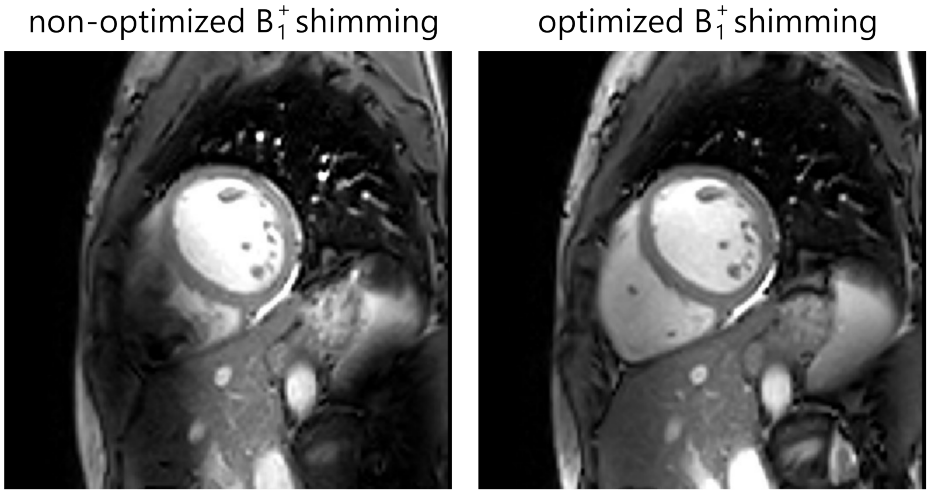

Figure 1.5.: Cardiac image examples with large present B_1^+ inhomogeneity (left) and optimized B_1^+ shimming (right).

Anatomy regions comprise many tissues with different electrical properties and geometries, making the prediction of B_1^+ inhomogeneity distribution non-trivial and computationally expensive. This can obstruct MR image interpretation, introduce bias in quantitative measurements, and impair signal-to-noise ratio (SNR) [36]. Instead of attempts to predetermine the B_1^+ inhomogeneity pattern, B_1^+ mapping sequences are usually performed at the beginning of MRI scanning protocols, to acquire voxel-wise B_1^+ distribution. B_1^+ maps are then used for quantitative measurement corrections, for homogeneity correction via B_1^+ shimming, or for deriving tissue electrical properties [37, 38].

Currently, a wide range of B_1^+ mapping methods has been developed, however, no single standard is established for all applications [37].

The optimal sequence choice is highly dependent on the expected B_1^+ magnitude dynamic range, required resolution, sequence sensitivity to motion, or time constraints. Since B_1^+ describes a rotating magnetic field, both field magnitude and phase can be considered.

An example of a common B_1^+ magnitude ($|B_1^+|$) sequence is actual flip angle mapping [39]. The sequence uses two baseline images with distinct repetition times to reconstruct the B_1^+ magnitude.

The phase of the transmit field may be required in addition to $|B_1^+|$ for corrections of phase-based quantitative methods, such as quantitative susceptibility mapping (QSM) and MR thermometry [40]. Unlike the B_1^+ magnitude, the phase ϕ^+ cannot be derived from MRI sequences directly, if only a single transmit coil is available. Instead, only the transceive phase $\phi^\pm$ is obtainable, for instance, as measured from a simple spin echo (SE) or balanced steady-state free precession (bSSFP) sequence [10, 40]. This reflects a sum of the RF transmit and receive phases $\phi^\pm = \phi^+ + \phi^-$. The transmit phase may be approximated as half of the transceive phase $\phi^+ \approx \phi^\pm/2$, which is known as transceive phase approximation (TPA) [41].

1.8. FROM ARTIFACT TO CONTRAST MECHANISM: ELECTRICAL PROPERTIES TOMOGRAPHY

While B_1^+ field inhomogeneity is frequently considered an unwanted effect in imaging, it can be exploited to derive valuable tissue biomarkers. The distribution of the transmitted RF field in the body is closely related to the electric properties, namely conductivity σ and permittivity ϵ, expressed jointly by the complex permittivity $\kappa = \epsilon - i\sigma/\omega_0$. In clinical use, EP reconstruction has been applied for the identification and classification of cancerous tissue, particularly in breast and neuroimaging [42]. From the Maxwell equations, one can derive the following Helmholtz equation for the transmitted magnetic field:

$$-\nabla^2 B_1^+ = \frac{\nabla\kappa}{\kappa} \times (\nabla \times B_1^+) + \kappa\omega_0^2\mu_0 B_1^+, \tag{1.4}$$

where μ_0 denotes the permeability of free space, and B_1^+ is expressed in a complex form, constituting both magnitude and phase components: $B_1^+ = |B_1^+|e^{-i\phi^+}$ [43]. Notably, dissecting the above equation into the real and imaginary components, it can be derived that $|B_1^+|$ distribution is primarily affected by tissue permittivity, while ϕ^+ distribution is more dependent on the conductivity [44]. Given the measured spatial distribution of the complex B_1^+ in the image, various reconstruction approaches have been developed to derive σ and ϵ. For instance, assuming $\nabla\kappa = 0$, the Equation (1.4) becomes:

$$\kappa = -\frac{\nabla^2 B_1^+}{\omega_0^2 \mu_0 B_1^+}. \tag{1.5}$$

This provides the simplest means of κ reconstruction in MRI based on the B_1^+ map, referred to as Electrical Properties Tomography (EPT). Note that this approach will produce errors at tissue boundaries due to the negligible $\Delta\kappa$ assumption. An array of methods has been developed for alternative EPT reconstruction, and most require B_1^+ derivatives of first or second order [44]. This makes EPT particularly sensitive to noise. Unlike B_1^+ mapping for calibration purposes, where low resolution is sufficient, EPT requires extremely robust and high-resolution mapping, in order to reconstruct voxel-wise conductivity of permittivity maps.

1.9. ENERGY DEPOSITION

Radiofrequency energy exposure during MR imaging is measured by the specific absorption rate (SAR) – a measure of energy deposition over time per given mass of tissue. The International Electrotechnical Commission (IEC) limits the mean SAR to not exceed 4 W/kg for a whole body over 15 minutes [45], to minimise the risk of tissue heating. SAR depends on a number of anatomical characteristics, such as body size, electrical tissue conductivity and resistance. In addition, SAR is quadratically proportional to both B_0 and B_1 amplitudes:

$$SAR \propto B_0^2 \tag{1.6}$$

$$SAR \propto \int B_1^2 dt \tag{1.7}$$

As a result, MRI sequence development in high magnetic field strengths becomes increasingly restricted, and SAR-efficient imaging remains an active research area of interest, aiming for an optimal trade-off between minimal scanning time and good SNR.

1.10. CARDIAC IMAGING

In addition to regular imaging challenges in static anatomies, cardiac magnetic resonance (CMR) poses further difficulties in imaging. The perpetual presence of cardiac and respiratory motion induces gross artifacts in imaging, if not accounted for. To tackle this, CMR images are often gated to the same cardiac cycle phase, as determined from the electrocardiogram (ECG) signal [46]. The respiration-induced motion can be mitigated via acquisition during breath-holds or the use of navigators - low-resolution images monitoring the diaphragm position - to trigger the acquisition based on the respiration cycle phase [47, 48]. In addition

to prospective motion correction strategies, advanced post-processing can be used to mitigate residual motion.

I

PART ONE
HARDWARE SOLUTIONS

2

LOWERING THE ACOUSTIC NOISE BURDEN IN MRI WITH PREDICTIVE NOISE CANCELING

This chapter is published as a pre-print: Šiurytė, P. and Weingärtner, S. (2024).Lowering the acoustic noise burden in MRI with Predictive Noise Canceling. medRxiv, 2024-04. doi.org/10.1101/2024.04.28.24305337

2.1. ABSTRACT

Although Magnetic Resonance Imaging (MRI) is performed in almost 100 million scans each year, patient comfort and acceptance rates are compromised by loud acoustic noise. Here we present an acoustic noise cancellation system using anti-noise predicted from scanner sounds. In this approach, termed predictive noise canceling (PNC), the acoustic fingerprint of an MRI system is obtained during a 60 s calibration, and used to predict anti-noise for arbitrary scans. PNC achieves acoustic noise attenuation of up to 13 dB across a wide range of clinical MRI sequences, with spectral noise peak reduction of up to 96.76 % occurring at 0.6-1.2 kHz. These results suggest that PNC can achieve substantial in-bore noise cancellation, providing a cheap and scanner-independent solution for improved patient comfort.

2.2. INTRODUCTION

The average person in the USA will have undergone seven medical Magnetic Resonance Imaging (MRI) scans by the end of their life - an increasing figure due to population aging [1]. Despite being known as safe and radiation-free, MRI exposes patients to extreme sound pressure levels (SPL) of up to 130 dB for prolonged time periods [2, 3]. This far exceeds public health recommendations [49] and puts patients at risk of temporary or permanent shift of the hearing threshold [4, 20–22]. Patient discomfort and anxiety, caused by the noise burden, further contribute to poor patient acceptance ratings, well below those of more damaging imaging modalities such as computed tomography [50]. Thus, novel solutions for reducing acoustic noise levels in clinical scanning sites worldwide are essential to ensure both patient comfort and safety.

Here, we evaluate a novel approach to active noise canceling (ANC) in MRI that allows for versatile noise reduction compatible with any MRI system and scan procedure. In the proposed approach, termed predictive noise canceling (PNC), anti-noise is generated prior to the scan procedure, based on the gradient input and a pre-calibrated acoustic noise correlation (see the animated abstract in Supplementary Video S1). We demonstrate live acoustic noise reduction inside a clinical 3T MRI scanner using a pneumatic headphone-imitating setup. The effectiveness of PNC is shown for a range of MRI sequences representative of a clinical scan portfolio. The impact of various MRI sequence parameters on the noise reduction capabilities is systematically studied and sources of noise cancelation imperfection are dissected.[1]

[1] Note the methods are detailed after the results section.

2.3. RESULTS

The main source of acoustic noise during MRI scans is the vibration caused by rapidly switching currents in the magnetic field gradient coils (see Figure 2.1A-B) [51]. In clinical MRI systems, the acoustic noise lies predominantly in the 0-3 kHz range [52], where the human ear is highly sensitive [3] (see Figure 2.1C). Potential methods for alleviating the noise burden include passive noise damping with headphones or earplugs [53], as well as hardware advances such as vacuum-mounted gradient coils [54] or ultra-fast gradient switching [55]. Passive noise reduction is mandatory in clinical use but leaves the most problematic lower frequencies vulnerable when used alone [23, 49, 53] (see Figure 2.1C-D). Hardware upgrades are no sustainable solution, as they are often incompatible with existing systems and are too costly for widespread use. ANC has received interest for suppressing low frequency noise. However, the strong magnetic fields in MRI restrict the acoustic equipment that can be used, greatly hindering the effectiveness of ANC [56–58]. For example, pneumatic sound transfer, as most commonly used in commercial MRI intercommunication systems [59, 60], incurs considerable latency, leading to a diminished frequency range for ANC effectiveness. As a result, recently introduced commercial ANC devices [61], report 30 dB reduction for ANC combined with passive cancellation, which is in line with the effectiveness of passive-only solutions [62].

2.3.1. MRI-COMPATIBLE NOISE CANCELING SETUP

To demonstrate latency-invariant noise reduction using prediction-based anti-noise, an experimental setup was constructed. An optical fiber microphone is placed inside the MRI scanner (Ingenia 3T, Philips Healthcare, Amsterdam, The Netherlands). Sound is transmitted to the in-bore position from an amplifier-driven speaker outside the scanner room through a pneumatic hose and funnel. Precise sound waves are generated by an arbitrary function generator (AFG) that powers the amplifier. The AFG is controlled using an external TTL (transistor-transistor logic) trigger from the MRI control system, to synchronize the MRI noise and the anti-noise with high temporal precision. A detailed description of the components and specifications of the setup is provided in the materials and methods section and Figure 2.1A.

A linear time-invariant (LTI) model is used to predict the total X/Y/Z gradient coil noise from the derivative of the gradient current inputs. Details evaluating the suitability of the LTI model are provided in the Supplementary Text and Figure S2.1. To construct the LTI model, individual transfer functions are derived for each of the three gradient coils, from a 60 s calibration procedure with triangular gradient pulses. This calibration procedure is setup-specific for a given subject positioning and needs to be performed only once for a conventional

scanning session.

All noise cancellation experiments are assessed in two frequency ranges: a broader spectrum (0.3-4 kHz), encompassing the majority of MRI sequence noise [3], and a narrower range (0.5-2 kHz), targeting the most intense sound pressure level (SPL) regions [63]. The noise reduction is described in the wide frequency range if not specified otherwise.

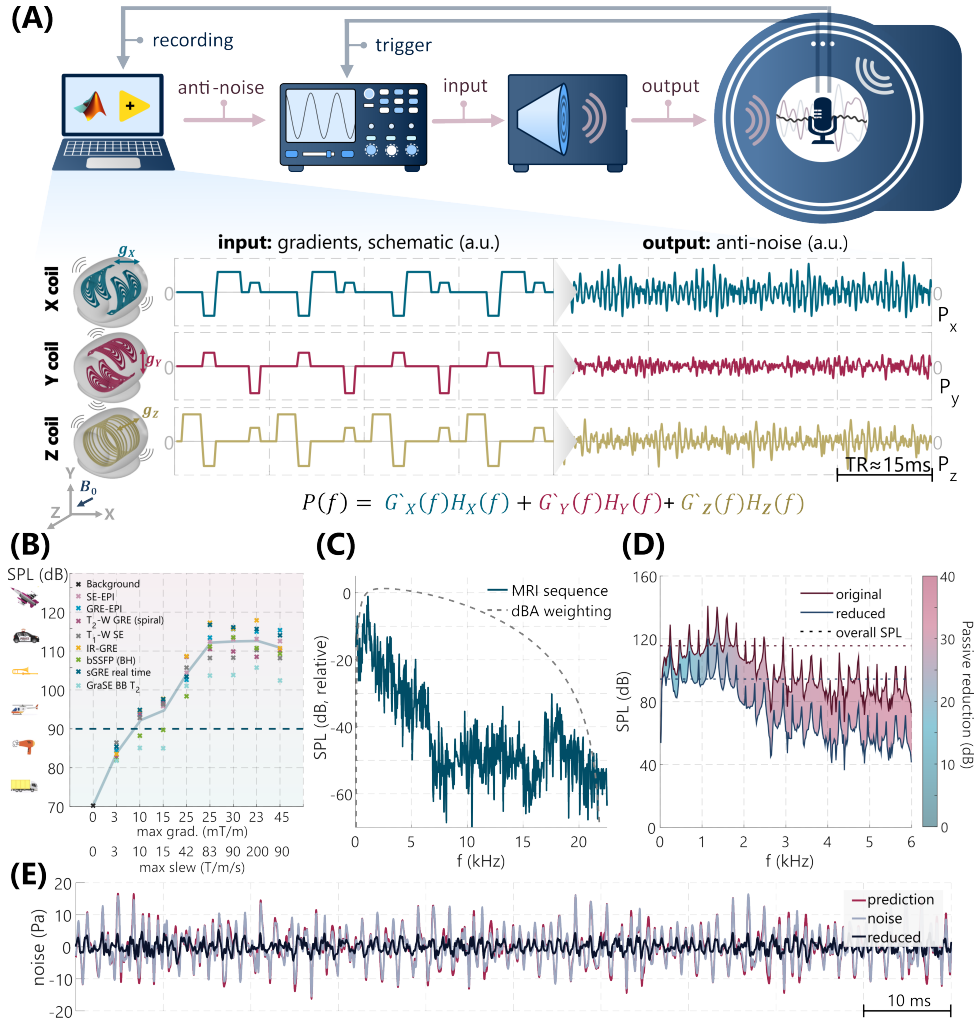

Figure 2.1.: Predictive Noise Canceling (PNC) pipeline and MRI acoustic noise characterization. (Continued on the following page.)

Figure 2.1.: (**A**) PNC pipeline (top), comprising a control PC, an arbitrary function generator (AFG) for signal synchronization, a sound playback system, and the MRI scanner. Optical microphone recordings are collected and processed for obtaining the acoustic fingerprint of the scanner. During output, synchronization between the AFG output and the MRI scanner is ensured using a transistor-transistor logic (TTL) trigger. Schematic representation (bottom) shows representative coil input $g_{X/Y/Z}$ during exemplary MRI sequence (TR ≈ 15 ms), and corresponding sequence noise prediction $p_{X/Y/Z}$. (**B**) Exacerbating noise burden of selected sequences for increasing gradient coil performance. The dashed line at 90 dB indicates the safe limit for prolonged exposure. Gradient system limits are based on historical scanner specifications [27]. (**C**) Example spectrum of MRI sequence noise (blue) and dBA weighting, approximating human hearing sensitivity (dashed line). (**D**) Example sequence noise spectrum before (pink line) and after (blue line) the application of passive reduction (earplugs), indicating the weakest reduction at lower frequencies. The dashed lines indicate overall sound pressure levels (SPL). (**E**) An aligned overlay of MRI sequence noise prediction and the original noise, as well as estimated reduced noise.

2.3.2. FEED-FORWARD SIGNAL CORRECTIONS

Feed-forward corrections are applied to the anti-noise prediction for pre-emptive compensation of inaccuracies in the sound playback system. For our setup, three dominant error sources are considered: 1) channel distortion, 2) output latency, and 3) recorder clock mismatch. All corrections are derived from on the 60 s calibration procedure only.

Channel distortion, as a result of the frequency response of the speaker and the sound transmission through the pneumatic hose, causes a mismatch between the intended and actual output (Figure 2.2A). Equalization (EQ) of the output was performed in multiple iterations using linear inverse-distortion filters derived from gradient blips in the calibration sequence (Figure 2.2B). Without EQ, live noise reduction showed negligible 0.23±0.62 dB noise cancellation across all three gradient coils. Applying EQ with an increasing number of iterations lead to improved live noise reduction, approaching a plateau at 18.62±1.11 dB with three EQ iterations (Figure 2.2C). Thus, three-iteration EQ was used for the remainder of the study.

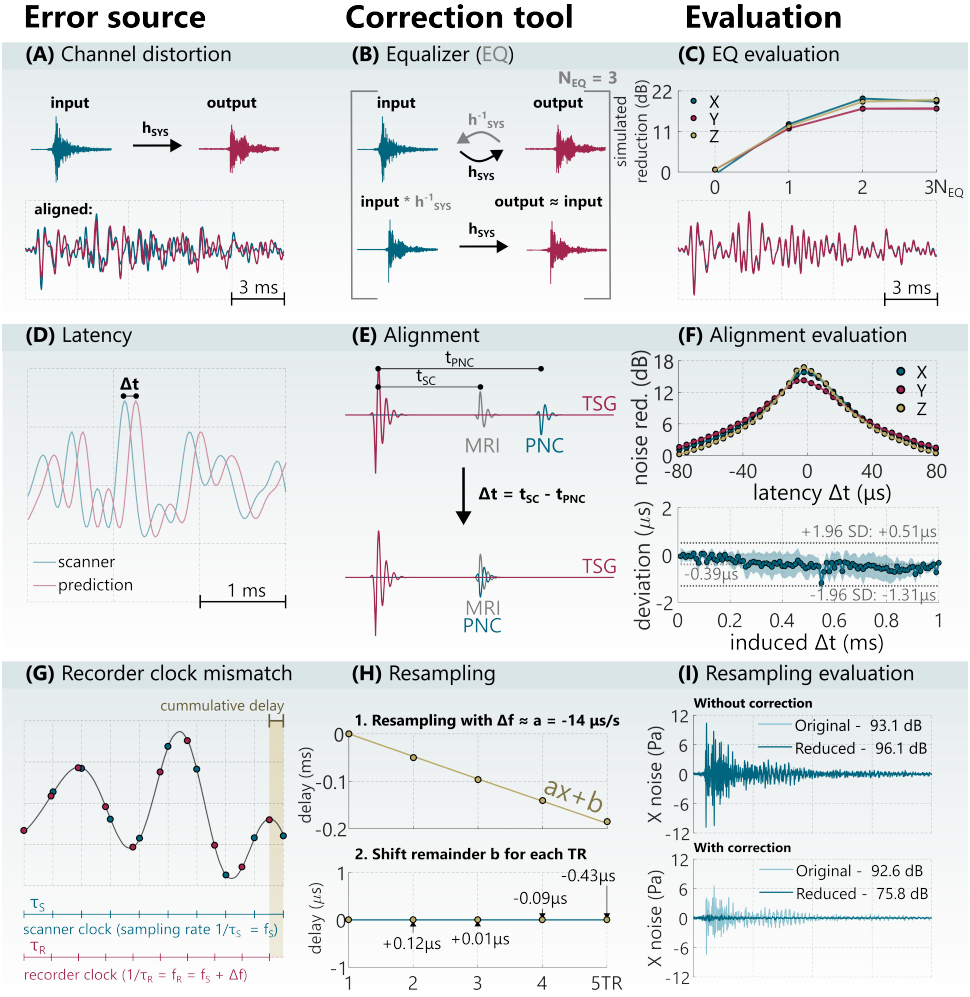

Figure 2.2.: Feed-forward corrections for effective noise cancellation. (Continued on the following page.)

Figure 2.2.: (**A**) Channel distortion modeled as a transfer function, h_{sys} (top), leads to deviation from the desired output (bottom). (**B**) Equalization (EQ) via inverse-distortion filters, h_{sys}^{-1}. (**C**) Exemplary noise reduction for different EQ iterations shows convergence at three iterations (top), leading to minimal output distortion (bottom). (**D**) Latency incurred during processing, sound production, and transport. (**E**) Latency Δt is estimated from the relative delay between the TTL synchronized gradient (TSG) sound and MRI gradient blip or the equalized PNC output. (**F**) Pronounced latency leads to poor noise reduction of triangular gradient pulses (0.14 ms rise time and 20 mT/m amplitude) (top), but retrospectively induced latency shows that it can be accurately estimated and corrected for (bottom). (**G**) recorder clock mismatch is apparent from the difference in the sampling rate of PC recordings (pink) and the scanner clock (blue). (**H**) The mismatch is corrected by linear resampling (top), followed by individual sample point shifts. (**I**) Live reduction examples with/without the correction (top/bottom) for a triangular X gradient (0.14 ms rise time and 20 mT/m amplitude) pulse, showing that sampling correction is necessary for effective noise cancellation.

Digital processing delays and sound travel times induce latency in the sound system. Pre-emptive latency correction was performed by measuring the delay between the scanner pulse and equivalent equalized output, following a TTL-trigger synchronized gradient blip (TSG) (Figure 2.2E). To evaluate the effect of latency on live noise reduction, delays from -80 to 80 μs were induced in the anti-noise predicted for X/Y/Z gradient pulses. PNC reduction efficiency in decibels was halved for 30.70±4.29 μs latency in triangular gradient blip experiments (Figure 2.2F). In a separate experiment, increasing delay was induced between the TSG and a gradient blip, ranging from 10 to 1000 μs in steps of 10 μs. Bland-Altman analysis of the induced and retrospectively measured delays shows less than 1.19 μs deviation. This suggests less than 0.5 dB expected loss in noise reduction efficiency due to residual latency effects.

Finally, the sampling rate of the recorder clock shows deviations from the scanner clock, leading to a cumulative delay (Figure 2.2G). Linear resampling was applied globally to all recorded signals, based on the recording drift of repeated TSG pulses (Figure 2.2H, top). Additionally, the residual short-term recorder clock variations in the calibration sequence were eliminated by shifting the samples of the individual gradient blip sounds (Figure 2.2H, bottom). Live noise reduction for X coil gradient blips without the clock-mismatch correction achieved poor

reduction performance (3.08±0.03 dB) due to dephasing of averaged calibration pulses. With correction, 16.87±0.04 dB live reduction was achieved (Figure 2.2I).

2.3.3. UP TO 13 DB NOISE REDUCTION IN MRI SEQUENCES

A test protocol of ten MRI sequences (2D steady-state free precession sequences, see Table S2.1), chosen to be representative of modern clinical MRI scan methods, was performed with and without PNC. Experiments were repeated in six scanning sessions, each acquiring one reference without PNC, one prediction-only recording, and five repetitions with PNC for each sequence.

PNC achieves consistent sound pressure reduction for all sequences, as illustrated in representative noise recordings in the time and frequency domain in Figure 2.3A (audio-visual illustration in Supplementary Videos S2-11). Up to 12.65 dB reduction in the wide frequency range and up to 13.55 dB in the narrow range were observed in individual sequence experiment iterations. The frequency spectrum of the sequences shows peak SPL between 600 and 1170 Hz, where noise reduction achieves 55.91-96.76% sound pressure reduction. Across all sequences and all scanning sessions, the mean reduction was 9.21±1.23 dB for the wide frequency range and 9.97±1.48 dB for the narrow range. For individual sequences, this ranged from 7.98±0.58 to 10.01±1.04 dB and from 8.75±1.73 to 11.00±1.39 dB in wide and narrow considered ranges, respectively (Figure 2.3B).

To dissect the noise cancellation results, four experimental error sources were isolated step-wise:

Step 1: measured live noise reduction;

Step 2: simulated reduction without timing error, using retrospective noise/anti-noise alignment;

Step 3: simulated reduction as in Step 2, but without playback error, using pre-output prediction as anti-noise;

Step 4: simulated reduction as in Step 3, but without the LTI model error, using pre-recorded sequence noise as prediction.

The most significant reduction in live noise occurs within the mid-frequency range (700-1700 Hz), with statistically significant differences compared to both low frequencies (300-700 Hz, $p \leq 0.002$) and high frequencies (1700-4000 Hz, $p \leq 0.0004$). Residual latency minimally affected noise reduction (Step 2), indicating highly effective latency control. Imperfect channel equalization (Step 2, compared to Step 3) reduced the effectiveness of PNC mostly at higher frequencies by 5.27±0.57 dB. Simulated noise reduction under idealized conditions

(Step 4) yields up to 40 dB (Figure 2.3C), indicating the largest efficiency loss is due to the LTI model imperfections. The same conclusions can be drawn from the noise reduction analysis for isolated gradient sounds, as shown in Figure S2.2.

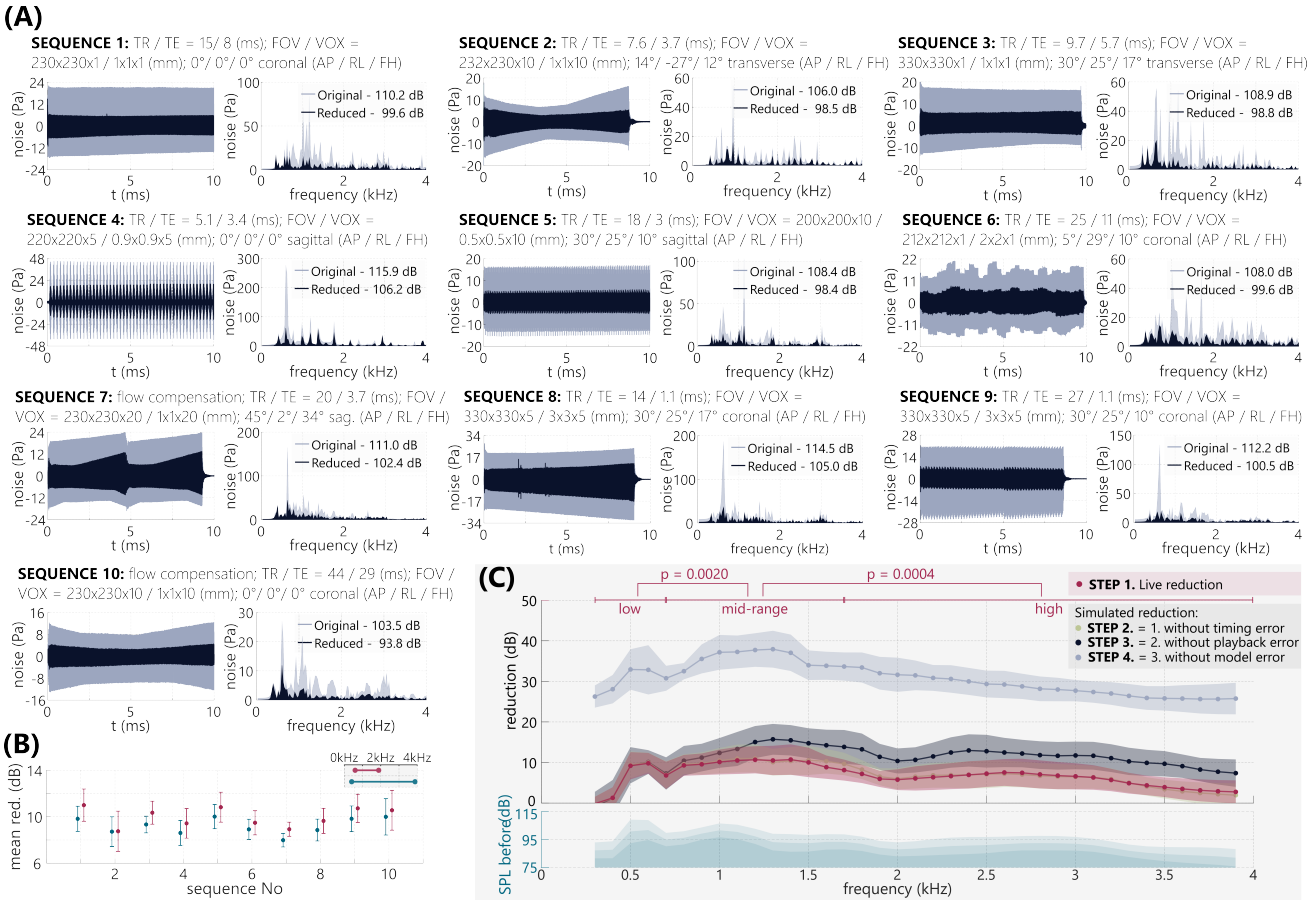

Figure 2.3.: Acoustic noise reduction in representative MRI sequences. (Continued on the following page.)

Figure 2.3.: (**A**) Sound pressure levels of the acoustic noise in time (left) and frequency domains (right) with and without PNC application. Sequences are characterized by repetition and echo time (TR/TE), field of view and voxel size (FOV/VOX), orientation, and anterior-posterior/right-left/feet-head angulation (AP/RL/FH). The legends indicate the overall reduction in the 0.3-4 kHz range. (**B**) A representative sequence noise reduction results, evaluated in the wide 0.3-4 kHz range (blue) and narrow 0.5-2 kHz range (pink). (**C**) Dissection of the acoustic noise reduction in the frequency spectrum, showing live noise reduction and simulated reduction, when virtually eliminating error sources related to timing, sound playback, and model limitations. Data points represent 100 Hz bins. PNC shows significantly higher noise reduction in the mid-frequency range compared with low/high frequencies.

2.3.4. LIVE REDUCTION IS ROBUST TO SEQUENCE MODIFICATIONS

Trends in the performance of PNC were tested by varying a range of acoustically relevant sequence parameters: repetition time (TR = 6.45 - 550.40 ms), slice-thickness (0.5 - 10 mm), bandwidth (BW = 271.7 - 617.3 Hz/Px), and slice angulation (angle = 0° - 162°). An exemplary balanced Steady State Free Precession (bSSFP) was used as base sequence (see Supplementary Table S2.1). For each parameter setting, noise reduction in wide and narrow frequency ranges was obtained from recordings with PNC in five repetitions and one reference measurement without PNC.

Thicker slices, leading to weaker slice selection gradients, show increased noise reduction with up to 11.00±0.12 dB (Figure 2.4A, 10 mm). At very thin slices (0.5 mm), noise reduction was compromised with 6.23±0.12 dB compared to 10.58±0.64 across 1-10 mm slices.

The readout gradient was modified by adjusting the acquisition bandwidth (Figure 2.4B). A slight drop in noise reduction was observed for mid-range bandwidths (300 - 450 Hz/Px) with 7.82±0.43 dB, while the best noise reduction was achieved at high bandwidths (> 550 Hz/Px) with 9.23±0.31 dB, where the readout gradient causes a higher overall SPL of the sequence.

Sequence TR was modified to alter the spacing of the gradient pulses, and, therefore, the primary noise frequency. Increasing TR lead to increased noise reduction with 10.75±0.36 dB at the longest considered TR of 550.4 ms (see Figure 2.4C). Compromised noise reduction was observed at ultra-short TRs with 5.87±0.01 dB.

Finally, rotating the imaging slice around a double-oblique axis varies the gradient input load across the three physical gradient coils. The

observed effect on live noise reduction showed minor variations of up to 1.74±0.29 dB across the orientations. The overall SPL of the sequence without noise reduction was lowest for 108°-144° indicating a differential acoustic response of the three gradient coils (see Figure 2.4D).

2.3.5. NOISE REDUCTION REMAINS STABLE ACROSS TIME

Next, PNC performance stability across time was analyzed with three 2-minute acquisitions: 1) A single-TR clip (12 ms) repeated with 250 ms spacing in 480 repetitions; 2) The corresponding clinical 2D bSSFP sequence (TR = 12 ms) with 21 repetitions of each phase-encoding step; 3) an equivalent length 3D bSSFP sequence (TR = 12 ms) (details in Table S2.1). The single-TR clip was selected as the phase encoding step with maximum gradient strength (see schematic in Figure 2.4E).

For an isolated single-TR clip, the mean reduction across the four steps was 10.07±0.37, 10.33±0.31, 15.28±0.15 and 26.48±0.22 dB at Steps 1 to 4, respectively, in the wide frequency range (see Figure 2.4F). Visualizing the noise reduction within the TR with a 10 ms sliding time window analysis shows that the reduction is most effective at the time point of the peak gradient noise response. Up to 10.96±0.60 and 13.07±0.31 dB reduction was measured in the wide and narrow frequency ranges with a 10 ms sliding window, respectively (Figure 2.4G). For the 2-minute experiments, good temporal stability of noise reduction was observed over a 1 s sliding window (Figure 2.4H-J). Mean sequence reduction in the first 10 seconds was averaging 11.42±0.18 / 14.69±0.15 dB, 10.00±0.57 / 11.39±0.51 dB and 8.43±0.04 / 10.06±0.18 dB in the wide/narrow ranges for the fixed-phase, 2D and 3D sequences, respectively. Comparatively, in the last 10 seconds, the average reduction was 11.22±0.10 / 14.19±0.09 dB, 9.41±0.54 / 10.76±0.44 dB and 9.70±0.07 / 10.67±0.04 dB. The overall comparable noise performance indicates high temporal stability, with most effective attenuation in SPL-intensive frequency regions.

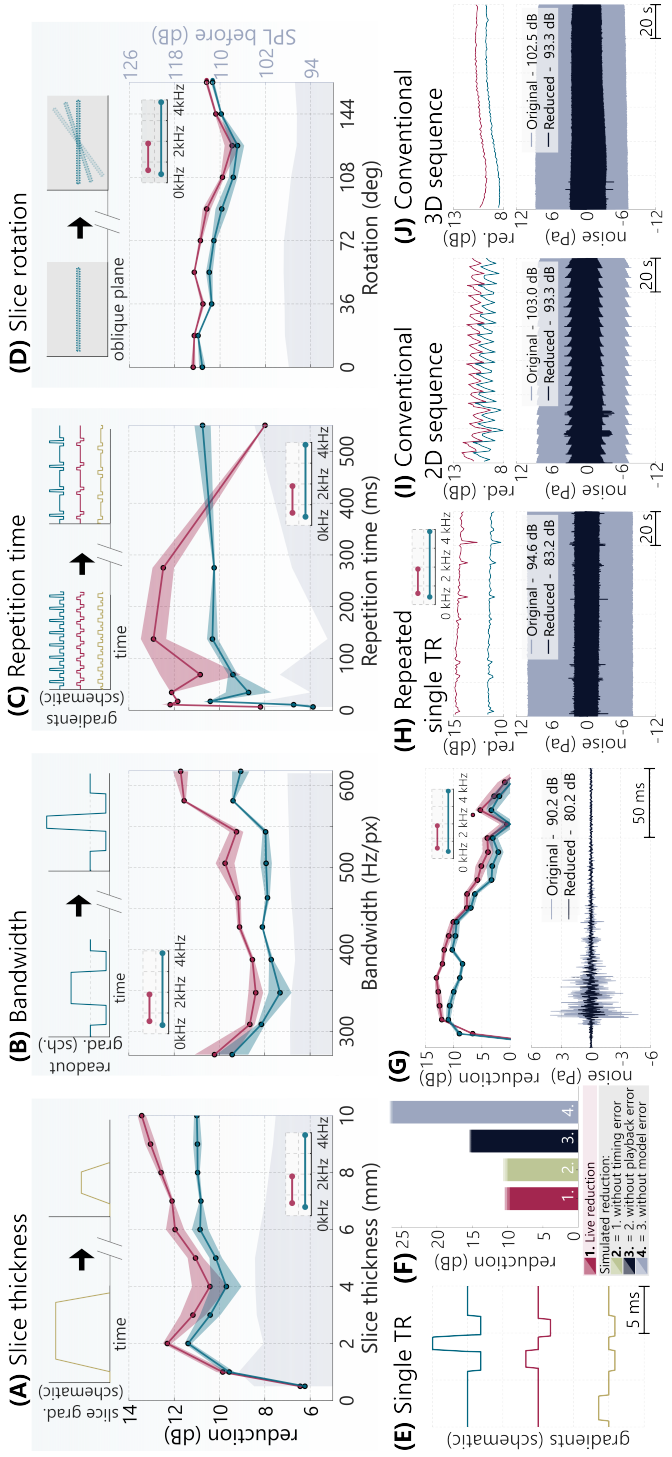

Figure 2.4.: Noise reduction for variations of acoustically relevant MRI sequence parameters. (Continued on the following page.)

Figure 2.4.: (**A-D**) Noise reduction in 0.3-4 kHz (blue) and 0.5-2 kHz (pink), with shading indicating the standard deviation. Gray shading depicts the sound pressure level (SPL) without reduction. (**A**) Slice thickness, affecting slice selection gradient; (**B**) bandwidth, affecting the readout gradient; (**C**) repetition time, affecting gradient spacing over time; (**D**) slice rotation, affecting gradient load distribution across physical coils. All gradient waveforms are schematic representations. (**E-G**) Noise reduction analysis on short time scale, showing (**E**) representative schematic single-TR gradients of a conventional MRI sequence; (**F**) short time scale analysis of a single TR clip, with live noise reduction and simulated reduction when eliminating individual error sources; (**G**) live noise reduction results over 10 ms sliding window. (**H-J**) Noise reduction across long time scales, evaluated over 1 s sliding window (top) in 0.3-4 and 0.5-2 kHz ranges, and an overlay of original and reduced noise over time (bottom). (**H**) Identical single TR clip from (E) repeated over 2 minutes, (**I**) regular 2D MRI sequence repeated in multiple dynamic repetitions over 2 minutes, (**J**) regular 3D MRI scan with a 2-minute duration. All long acquisitions show temporally stable noise reduction.

2.4. DISCUSSION

In this study, predictive generation of anti-noise, based on the gradient coil inputs, was used in a model setup, demonstrating versatile attenuation of MRI sequence sounds of up to 13 dB. Across a wide range of sequences, up to 96.76% sound pressure peak reduction was achieved in live noise reduction experiments. The method showed adaptability to changes in the sequence input and length, requiring only a single calibration for a set patient position per scan session.

The noise prediction in PNC is based on the acoustic modeling of scanner sounds. LTI models have previously been shown to be good candidates for approximation of the gradient coil noise in MRI, in the context of SPL prediction for sequence design [28–32]. Our results demonstrate that an LTI model provides a viable starting point for the predictive anti-noise application, where time domain sound wave match is critical. At the same time, the dissection of the noise reduction performance shows that model limitations are the primary factor of incomplete noise reduction. While good linearity of individual gradient pulses has been shown, gradient superposition and time-invariance violations, such as those induced by gradient heating, may limit the noise reduction capabilities when using LTI models. Thus, the use of

non-linear, data-driven, or thermal [64] modeling may provide an avenue to more accurately predict the gradient noise in scan setup-specific ways and further improve the noise reduction capabilities of PNC.

In our experiments, a comprehensive 60 s calibration procedure was designed to enable thorough corrections of error sources in a proof-of-principle setup. Triangular gradient pulses have been used to yield maximum acoustic response across a broad frequency range. For practical use, shorter calibration sequences can be evaluated, for example, using shorter pulse separation, employing a sequence-specific pre-scan, or re-purposing already present pre-scans for noise canceling calibration. Repeated calibration may also be useful in the presence of motion. Due to differences in the wavefield, displacement of the head in the centimeter range may lead to significant reduction, which can be alleviated with re-calibration.

To demonstrate the effectiveness of PNC in situ, a pneumatic single-channel headphone model was constructed. This resulted in additional unwanted errors in the signal output. The four-step reduction cascade analysis revealed that after including LTI model, channel distortion was the biggest experimental contributor to reduced noise canceling. While careful equalizer (EQ) calibration achieved up to 18.62±1.11 dB simulated reduction, deep nulls in sound transmission may be present, for instance, as a result of the wave transduction through the hose. Steady improvements in high-fidelity hardware have enabled MRI-compatible acoustic devices with excellent acoustic properties. For example, piezo-electric speakers [65], electro-dynamic devices [66] or micro-electro-mechanical system (MEMS) [62] have been proposed for clear sound production in two-channel headphones. The integration of PNC with these hardware developments bears great promise for improved reduction capabilities and warrants investigation in future studies.

In clinical MRI, the predominant cylindrical scanner shape acts as a waveguide and causes resonances at certain frequencies [52]. In addition, room dimensions result in acoustic echoes, presenting secondary sound waves. PNC can offer a location-specific solution adaptive to the overall room acoustics. Notably, while the main contribution to the perceived sound in MRI happens through air sound pressure waves, a portion of sound is transmitted through vibrations in bone and tissue. This pathway is regularly less dominant, however, if the air transmission suppression is strong enough, bone conduction becomes a dominant contribution [25]. Additionally, it can be enhanced at low frequencies with the use of earplugs via the occlusion effect [67]. Headphone-based application of anti-noise primarily targets the air transmission pathway, and therefore may have limited effect on reducing the noise burden experienced from bone conduction. However, a subject-specific adaptation of the anti-noise has previously

been reported to lower the psycho-acoustic noise burden from bone conduction [68]. Furthermore, in PNC, the creation of larger silent zones may be attainable if speaker arrays are used, instead of headphones. Creating silent zones around the skull or relevant patient areas in other applications, such as neonatal imaging, may therefore be a promising pathway to tackle residual bone conduction in a PNC setting.

PNC showed up to 13 dB reduction In the 0.3-4 kHz range in our experiments. While hardware-related approaches to noise reduction boast up to 30 dB [54, 55] and sequence-tailoring may reach 20-40 dBA reduction [3], these approaches require either costly upgrades or trade-offs in acquisition quality. PNC could offer an affordable add-on solution to substantially reduce the acoustic noise in MRI without altering the imaging process. While the pneumatic system with PNC in this work achieved on average lower reduction than reported ANC values of 10-30 dB [63], it showed peak performance in the SPL-intense mid-frequencies. ANC approach attenuation is most suitable for low frequencies below 700 Hz [3], offering less overlap with the SPL-intense regions of MRI sequence noise. Combining PNC with ANC and passive reduction methods could provide a particularly balanced reduction spectrum, with effective attenuation throughout low, mid-range and high frequencies.

PNC is intrinsically compatible with a wide range of scan systems. Gradient noise is known to scale up with the main magnetic field due to increased Lorentz forces [69, 70] despite Lorentz damping [52], leading to concerns about SPL in emerging ultra-high field applications. Gradient amplifier improvements enable increasingly higher slew rate and amplitude capabilities. In the absence of better gradient assembly damping, this leads to louder acoustic output (Fig. 1B). The resulting noise burden strongly contributes to severe anxiety and claustrophobic reactions, which occur in 5-10 % of patients [71]. Thus, implementation of acoustic noise reduction methods is indispensable and timely, and together with other comfort-oriented solutions may reduce claustrophobic incidents by up to threefold [72]. In this light, predictive noise canceling bears great promise as a flexible and cost-effective solution for lowering the acoustic noise burden in existing and new MRI sites.

2.5. METHODS

2.5.1. EXPERIMENTAL SETUP DETAILS

All experiments were performed in 3T MRI scanner (Ingenia 3T, Philips Healthcare, Amsterdam, The Netherlands). The headphone model consisted of a single-channel optical fiber microphone (Phonoptics, France), placed inside the bore next to a pneumatic rubber hose (3.5 cm inner diameter, 7 m long) with a widening plastic funnel end of 20 cm in diameter (see Figure S2.3). To maintain microphone position

stability across scanning sessions, a half-cone frame-shaped holder was printed with polylactic acid (PLA) and mounted on the funnel. The microphone was manually positioned at the isocenter of the MRI scanner. In the control room, the hose was connected to a widening funnel inside a custom-built speaker box with a fitted 20 cm diameter woofer. The speaker box was connected to a signal amplifier (Technics, Japan). The microphone signal was recorded with a PC system (Windows 11, 11th Gen Intel(R) Core(TM) i7-1165G7 CPU) at 44.1 kHz sampling rate. Anti-noise was played through an AFG (AFG31002, Tektronix, US), providing high temporal resolution (250 MHz sampling frequency). For time synchronization with the MRI, an external TTL signal was passed and received by the AFG to trigger the output using the Functional Brain Imaging Box (Philips Healthcare, Amsterdam, The Netherlands).

All experiments were performed with 22.5 mT/m and 200 T/m/s gradient system limits. During recordings, regular helium pump operation was maintained, while bore ventilation was turned off, resulting in ≈ 70 dB background noise.

2.5.2. SIGNAL PROCESSING

All experiments were controlled using a custom-built Labview application (National Instruments, Austin, TX, US) which contained AFG drivers and Matlab (Mathworks, Natwick, MA, US) plug-in scripts. This application was used for receiving recorded signals, processing the data, and sending control commands for the output. To diminish background noise, all recorded signals were band-pass filtered to the relevant sequence noise using a 0.3-4 kHz passband. To facilitate retrospective recording alignment, 1 s TSG blip noise was used.

2.5.3. LINEAR TIME-INVARIANT MODEL

To predict gradient noise, a linear time-invariant (LTI) model was used. The model convolves the derivative of the gradient input $g_{X/Y/Z}(t)$ with corresponding transfer functions $h_{X/Y/Z}(t)$, to derive noise prediction components $p_{X/Y/Z}(t)$. These are superimposed to estimate total gradient noise: $p(t) = g'_X(t) * h_X(t) + g'_Y(t) * h_Y(t) + g'_Z(t) * h_Z(t)$. The homogeneity and superposition assumptions of the linear model were experimentally tested by pulse amplitude scaling and by comparing the superposition of single gradient pulse noise to double gradient pulses. The test results are detailed in the Supplementary Text and Figure S2.1.

2.5.4. CALIBRATION SEQUENCE

A calibration pulse sequence was designed to obtain transfer functions and perform experimental error corrections (see Supplementary Text). The sequence comprised 20 consecutive TSG pulses (triangular blips

with 20 mT/m amplitude and 0.14 ms rise time, played on all coils) with TR = 3 s, interleaved with the calibration pulses with a 2 s delay. Triangular calibration gradients were played across different axes to obtain individual coil transfer functions (see Figure S2.4A). The chosen gradient parameters were 20 mT/m amplitude and 0.14 ms rise time, resulting in well-characterized sound predictions in the 0.3-4 kHz range (Figure S2.4B). The calibration gradients were averaged over 5 repetitions. This number was chosen based on experiments indicating plateauing simulated noise reduction under ideal playback conditions (Figure S2.4C).

2.5.5. FEED-FORWARD SIGNAL CORRECTIONS AND EVALUATION METRICS

For the equalizer implementation, the inverse 10001 point filter was fitted by deconvolution using a Toeplitz matrix, with 500 point non-causal element. The EQ inputs/outputs were defined as the playback and original recording of a gradient blip. To evaluate the reduction with different EQ orders, live reduction values for each EQ iteration were estimated over five repetitions for each coil gradient blip (20 mT/m amplitude and 0.14 ms rise time), over a 100 ms window.

For latency correction, the signals were over-sampled by a factor of 100, and maximum cross-correlation was used to identify the delay time. The final signal was obtained by down-sampling to the original sample rate. To evaluate the latency effects in the -80 to 80 μs range, 36 equally spaced steps were used. Five repetitions were used, measuring the reduction over a 100 ms window with the highest SPL.

The recorder clock mismatch was estimated from the accumulating displacement of TSG noise clips in the calibration sequence. To evaluate the clock-mismatch correction, five live reduction repetitions of X gradient coil blips were acquired, and noise reduction was evaluated over a 100 ms window.

2.5.6. NOISE REDUCTION METRICS

A variety of 2D steady-state free precession (FISP) sequences were used with different sequence settings. The number of serial averages was chosen to achieve a total duration of ≈10 s for each sequence. Complete sequence parameters are listed in Table S2.1.

Step 1-3 data were derived from the same 6 scanning sessions, while Step 4 data (simulated reduction under ideal timing, playback, and model conditions) were acquired in a separate scanning session, where each sequence noise was acquired with 5 repetitions. For Steps 3 and 4, only one repetition of scanner-only and prediction-only noise was acquired per sequence per session. Hence, the data represents a mean

over 10 sequences and 6 scanning sessions. All noise reduction values in Figure 2.3 were estimated over a time window corresponding to active gradient coils (8-10 s). The frequency analysis was performed in 100 Hz bins. Pairwise p-values for low, mid-range, and high frequencies (300-700, 700-1700, and 1700-4000 Hz) were derived from t-tests of band-passed live reduction (Step 1) data, averaged over all sequences and scanning sessions.

For studying robustness to sequence modifications, 2D balanced steady-state free precession (bSSFP) sequence variations were used (sequence parameters in Table S2.1). Four acoustically significant sequence parameters were individually changed in four scanning sessions. Reduction values were estimated over a time window corresponding to active gradient coils (9-39 s).

For temporal stability analysis, the noise reduction cascade for the single-TR sequence was estimated by acquiring 15 noise repetitions for each step. The data are represented as the mean reduction over a 200 ms most SPL-intense window with error bars indicating ±SD in Figure 2.4F. Single-TR sequence reduction as a mean over a 10 ms sliding window is represented as a mean of 15 time-aligned repetitions, with ±SD error bars.

2.6. ADDITIONAL INFORMATION

All experimental acoustic noise data, animated abstract and other supplementary videos can be found at https://gitlab.tudelft.nl/mars-lab/predictive-noise-canceling.

2.7. SUPPLEMENTARY INFORMATION

2.7.1. HOMOGENEITY AND SUPERPOSITION TESTING IN LTI SYSTEM

To verify the linearity and time-invariance assumptions in the system, homogeneity and superposition properties were experimentally verified. To assess homogeneity, triangular gradient pulses were played with 1 to 22 mT/m amplitudes at three rise times (0.14 ms, 0.34 ms and 0.54 ms). The root-mean-square (RMS) sound pressure was measured over a 100 ms window containing the majority of the noise output. Five repetitions were acquired for X, Y and Z gradient coil pulses, as well as for a simultaneous triple coil gradient pulse. In all cases, excellent linearity was confirmed (Pearson-correlation coefficient R^2 >0.999, Figure S2.1A).

To evaluate superposition, triangular gradient pulses (0.14 ms rise time) were played simultaneously on two gradient coils at a time. The amplitude was varied linearly between the two gradient coils in eleven steps, starting from 0 mT/m to 20 mT/m amplitude on one coil and 20 mT/m to 0 mT/m on the other coil (Figure S2.1B). The double gradient noise was recorded with five averages for all three combinations of gradient coils (XY, YZ, ZX). This noise was then compared to retrospectively superimposed single gradient coil pulse noise, for each amplitude mixing ratio. Single gradient coil pulses were also acquired with five averages. Simulated reduction under ideal timing and playback conditions for the double-coil gradient pulses was then evaluated in two modes: using the superimposed single-coil gradients; and using the double-gradient noise as a baseline. For the latter, simulated reduction values excluded the pairs of identical signals. Up to 2.4 dB higher error is observed at high mixing ratios, indicating moderate superposition-induced deviations.

2.7.2. CALIBRATION AND ERROR CORRECTION INTEGRATION

During the noise canceling experiments, transfer function calibration sequence (Figure S2.4A) recordings were repurposed to derive the feed-forward corrections for efficiency.

Recorded TSG train noise was used to estimate the recorder-induced clock mismatch, and the signals were resampled accordingly. Using the first five TSG repetitions, an initial guess was derived for the inverse frequency distortion filter h_{sys}^{-1} (1^{st} order EQ filter). The recorded TSG noise was passed as an EQ input, and the output was recorded during the first five TRs of the calibration sequence. An inverse distortion filter (≈ 230 ms) was calculated in the time domain using deconvolution by Toeplitz matrix construction. The subsequent noise prediction signals were convolved with h_{sys}^{-1} prior to output.

After the first calibration sequence iteration, the sequence was repeated for output tuning (calibration step 2). On the scanner, only

TSG pulses were played, and the calibration pulses were replaced by the noise prediction output, convolved with an inverse distortion filter. After performing the two-step recorder clock-mismatch correction, output latency was estimated by averaging the latency of five X/Y/Z pulses, relative to the scanner noise in the first calibration step.

During this step, a higher-order EQ filter was derived by using X/Y/Z noise prediction as EQ input and the corresponding recorded noise as EQ output (averaged over 5 repetitions each). 2^{nd} order inverse distortion filter was estimated for the three coils separately and subsequently averaged. The total inverse frequency distortion filter h_{sys}^{-1} was updated by convolving the 1^{st} and 2^{nd} order inverse distortion filters. This procedure was repeated in another iteration of calibration step 2, to achieve a 3^{rd} order EQ correction.

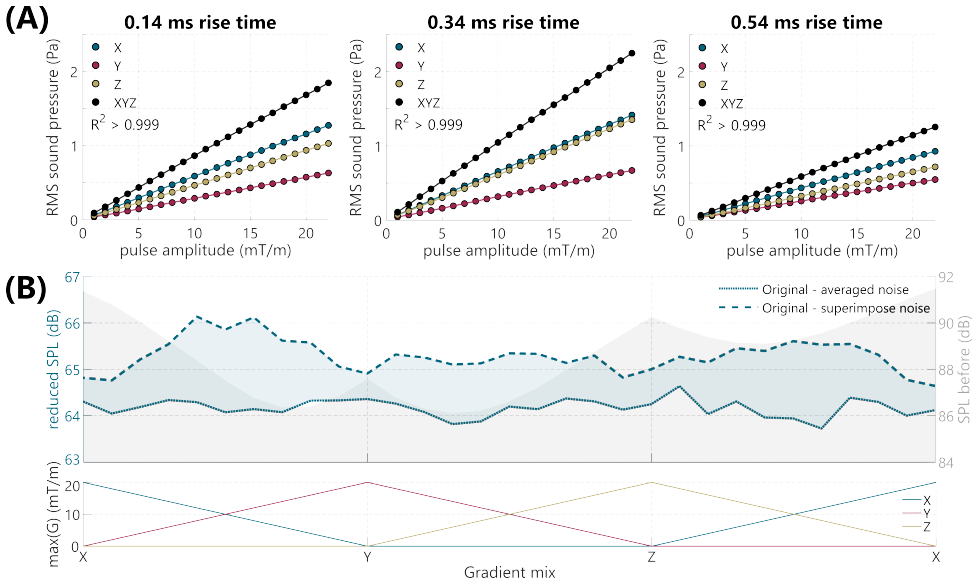

Figure S2.1.: System linearity evaluation. (**A**) Linearity test - total root mean square (RMS) sound pressure measured for triangular gradients for each gradient coil separately or all three gradient coils combined. The gradient amplitude was varied for 0.14/0.34/0.54 ms rise times. Excellent linearity is observed for each gradient coil and rise time (R^2 >0.999). (**B**) Superposition test. For linear combinations of two-coil triangular gradients (0.14 ms rise time), the reduction modes were simulated under ideal timing and playback conditions, using two models: retrospectively superimposed averaged single-coil gradient noise (dashed line) and averaged double-coil gradient noise (dotted line, equivalent to Step 4). The blue shaded area represents the superposition error that reaches up to 2.4 dB at high mixing ratios, indicating moderate deviations from the linear time-invariant (LTI) model. The gray shaded area represents gradient SPL before simulated noise reduction.

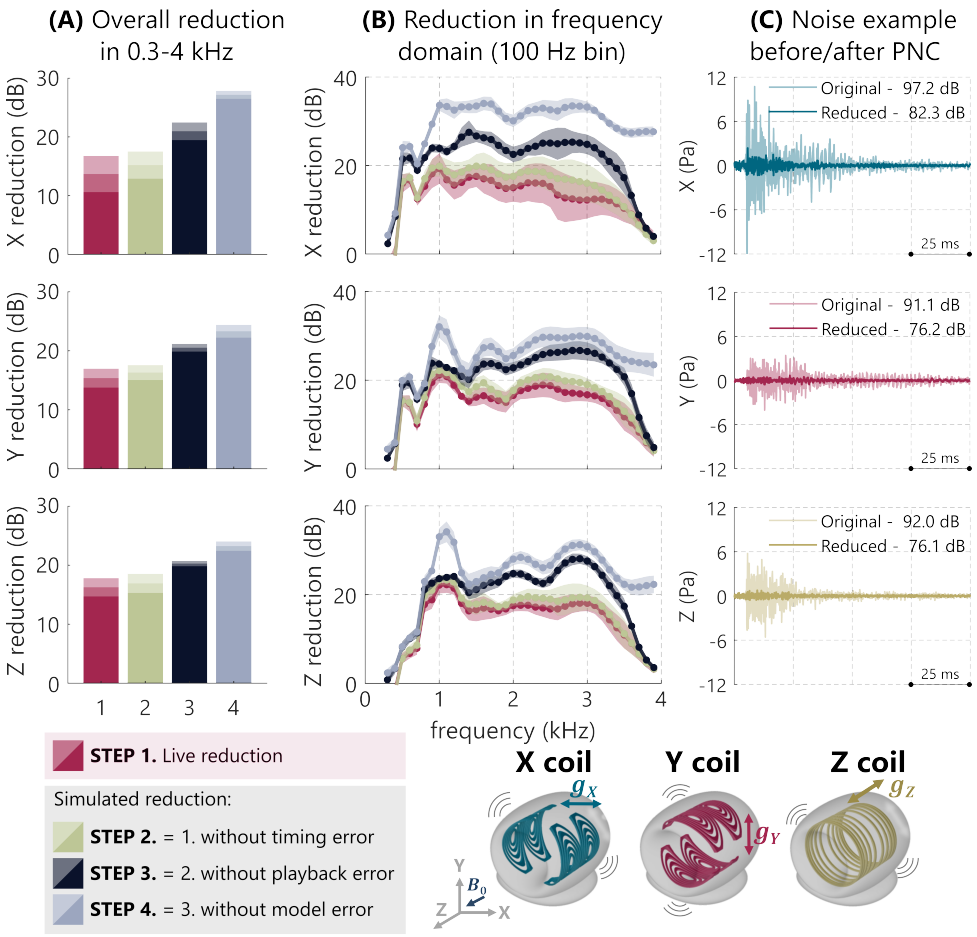

Figure S2.2.: Triangular pulse reduction cascade for X/Y/Z gradient coils. (**A**) Triangular gradient pulse live noise reduction and simulated reduction when virtually excluding experimental error sources in the four steps for the wider frequency range of 0.3-4 kHz. ± standard deviation is indicated as shading in the error bars. (**B**) Step 1-4 reduction cascade in the frequency domain over 100 Hz bins. (**C**) Example live noise reduction (Step 1) in the time domain for a single triangular gradient pulse.

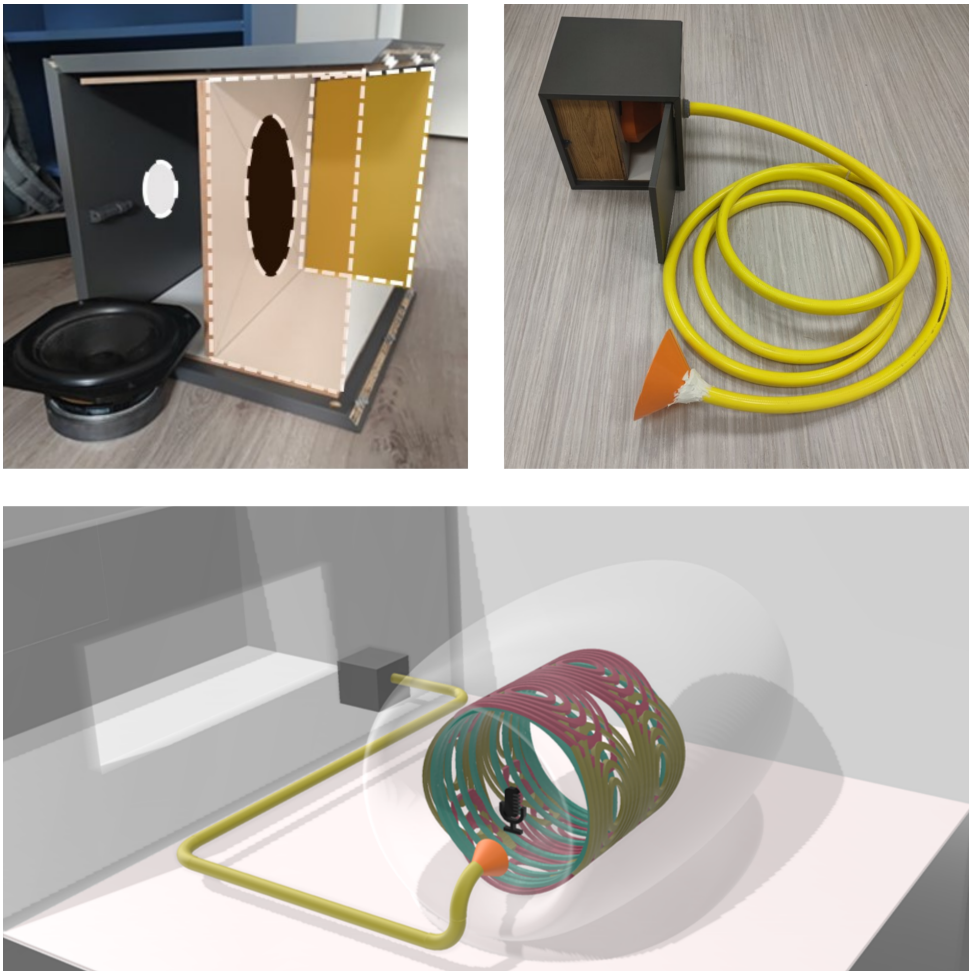

Figure S2.3.: Experimental headphone model setup. Top left illustration shows the two-compartment structure of the custom-made speaker box, with one compartment dedicated for the isolated woofer, and another one for the narrowing plastic funnel. Top right picture shows the speaker box connectivity to a long hose for pneumatic sound transfer. The bottom schematic shows the speaker box (gray) placement in the control room during the experiments, with another hose end (orange) positioned in the scanner bore next to the microphone.

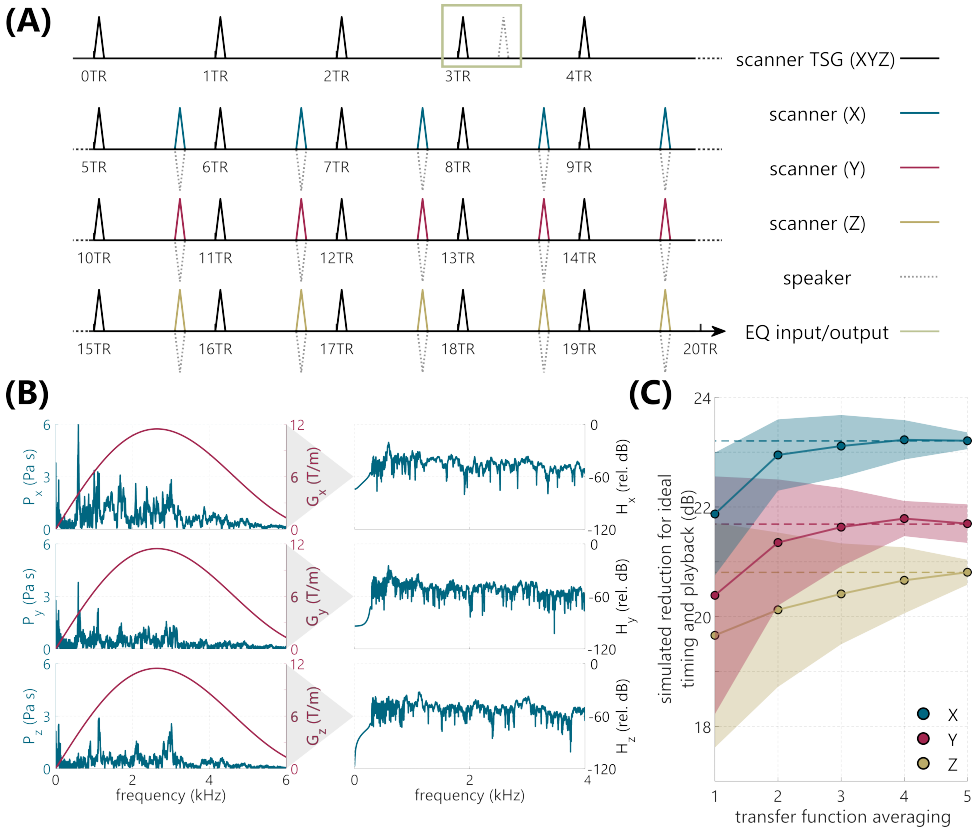

Figure S2.4.: Calibration sequence scheme details. (**A**) Triangular gradient pulse live noise reduction and simulated reduction when virtually excluding experimental error sources in the four steps for the wider frequency range of 0.3-4 kHz. ± standard deviation is indicated as shading in the error bars. (**B**) Step 1-4 reduction cascade in the frequency domain over 100 Hz bins. (**C**) Example live noise reduction (Step 1) in the time domain for a single triangular gradient pulse.

Table S2.1.: MRI sequence parameter list (caption continued in the next page).

Experiment name	Sequence type	TR (ms)	TE (ms)	BW (Hz/px)	FOV (mm^3)	voxel (mm^3)	plane	ang.(°AP/ RL/FH)
Sequence 1	2D FISP	15	8	913.2	230×230×1	1×1×1	coronal	0/0/0
Sequence 2	2D FISP	7.6	3.7	189.7	230×230×10	1×1×10	transverse	14/-27/12
Sequence 3	2D FISP	9.7	5.7	918.3	330×330×1	1×1×1	transverse	30/25/10
Sequence 4	2D FISP (22 shots)	5.1	3.4	826.2	220×220×5	0.9×0.9×5	saggital	0/0/0
Sequence 5	2D FISP (80 shots)	18	3	473.5	200×200×10	0.5×0.5×10	saggital	30/25/10
Sequence 6	2D FISP	25	11	86.9	212×212×1	2×2×1	coronal	5/29/10
Sequence 7	2D FISP with flow comp.; EPI factor 3	20	3.7	913.2	230×230×20	1×1×20	saggital	45/2/34
Sequence 8	2D FISP	14	1.07	2790.2	330×330×5	3×3×5	coronal	30/25/17
Sequence 9	2D FISP (22 shots)	27	1.07	2790.2	330×330×5	3×3×5	coronal	30/25/10
Sequence 10	2D FISP with flow comp.; EPI factor 3	44	29	35	230×230×10	1×1×10	coronal	0/0/0
Slice thickness study	2D bSSFP	12	5.7	757.6	400×400× **(0.5,1:10)**	0.8×0.8× **(0.5,1:10)**	coronal	30/36/-20
Bandwidth study	2D bSSFP	9.3	4.6	**A***	400×400×10	0.8×0.8×10	coronal	30/36/-20
Rep. time study	2D bSSFP	**B***	2.1	757.6	400×400×10	0.8×0.8×10	coronal	30/36/-20
Rotation study	2D bSSFP	12	5.7	217	400×400×10	1×1×10	coronal	10/-15/ **-142:18:20**
Long seq. 1, single-TR	2D bSSFP	250	5.7	757.6	400×400×10	0.8×0.8×10	transverse	0/0/0
Long seq. 2	2D bSSFP	12	5.7	757.6	400×400×10	0.8×0.8×10	transverse	0/0/0
Long seq. 3	3D bSSFP; 22 slices	12	5.7	757.6	400×400×1	0.8×0.8×1	transverse	0/0/0

***A** - 271.7, 308.6, 347.2, 387.6, 427.4, 463.0, 505.1, 543.5, 581.4, 617.3 Hz/px
***B** - 6.5, 10.8, 17.2, 34.4, 68.8, 137.6, 275.2, 550.4 ms

Table S2.1.: FISP - fast imaging with steady-state free precession; bSSFP - balanced steady state free precession; EPI - echo-planar imaging; TR - repetition time; TE - echo time; BW - bandwidth; FOV - field of view; AP/RL/FH - angulation values from orientation plane - anterior-posterior/right-left/feet-head.

3

ADAPTIVE RADIOFREQUENCY SHIMMING IN MRI USING RECONFIGURABLE DIELECTRIC MATERIALS

This chapter is currently under review for publication to Scientific Reports: Šiurytė, P., van de Velde, R., van Leeuwen, J., Brink, W., Weingärtner, S. (2024). Adaptive radiofrequency shimming in MRI using reconfigurable dielectric materials.

3.1. ABSTRACT

Inhomogeneity of the transmitted radiofrequency field (B_1^+) is a major factor hindering the image quality in Magnetic Resonance Imaging (MRI) at high field strengths. Here, a novel approach is presented, to locally modulate the B_1^+ utilizing an array of high permittivity materials with switchable connections. A 3×3 array of barium titanate suspension elements was constructed, with two PIN diode-based switchable connectors per element. Electromagnetic simulations were performed to determine configurations that produce strong B_1^+ modulation. Remote B_1^+ field switching was tested in a disk- and and a torso-shaped phantom at 3T by applying different bias voltages to the PIN diodes. The attained B_1^+ modulation was assessed at various switching pattern positions and various depths within the phantoms. The configuration with the strongest effect size has produced up to 11% modulation in simulations at 15 mm depth, with excellent translation properties. The effects were successfully replicated in phantoms, with a 5 V bias voltage producing up to 11.6±0.2% modulation. At the relative depth of the human heart, up to 6% of modulation was observed in the torso phantom. The presented method may provide a promising direction for cost-effective, and adaptive B_1^+ shimming without changes to the scanner hardware.

3.2. INTRODUCTION

In Magnetic Resonance Imaging (MRI), high static magnetic field strengths (B_0) of 3T and above have been increasingly used due to the gains in available signal-to-noise ratio (SNR) [73]. However, image quality at high-field MRI can suffer from artifacts caused by inhomogeneities in the transmitted radiofrequency (RF) field, B_1^+ [74]. These artifacts become apparent when the RF wavelength approaches the dimensions of the anatomy of interest, such as in body imaging at 3T or neuroimaging at 7T and above [74, 75]. In these configurations, the formation of standing waves decreases the transmit field homogeneity, giving rise to image shading and contrast non-uniformities. In cardiac MRI, this can lead to signal variations of up to 50% across the heart [8], reducing image quality and hindering clinical interpretation [76].

Several methods have emerged to improve B_1^+ field homogeneity, a process referred to as shimming. Parallel RF transmission (pTx) can be used when multiple RF transmit channels are available [77]. The amplitude and phase of each channel can be configured to improve the homogeneity of the resulting superimposed B_1^+ field. This has become the technological standard in many body imaging applications at 3T [78]. Additionally, individual control of the transmitted waveform can enable short-time scale variation of RF pulses to improve magnetization homogeneity further [79, 80]. However, in both cases, the shimming capabilities are limited by the available software and hardware [81].

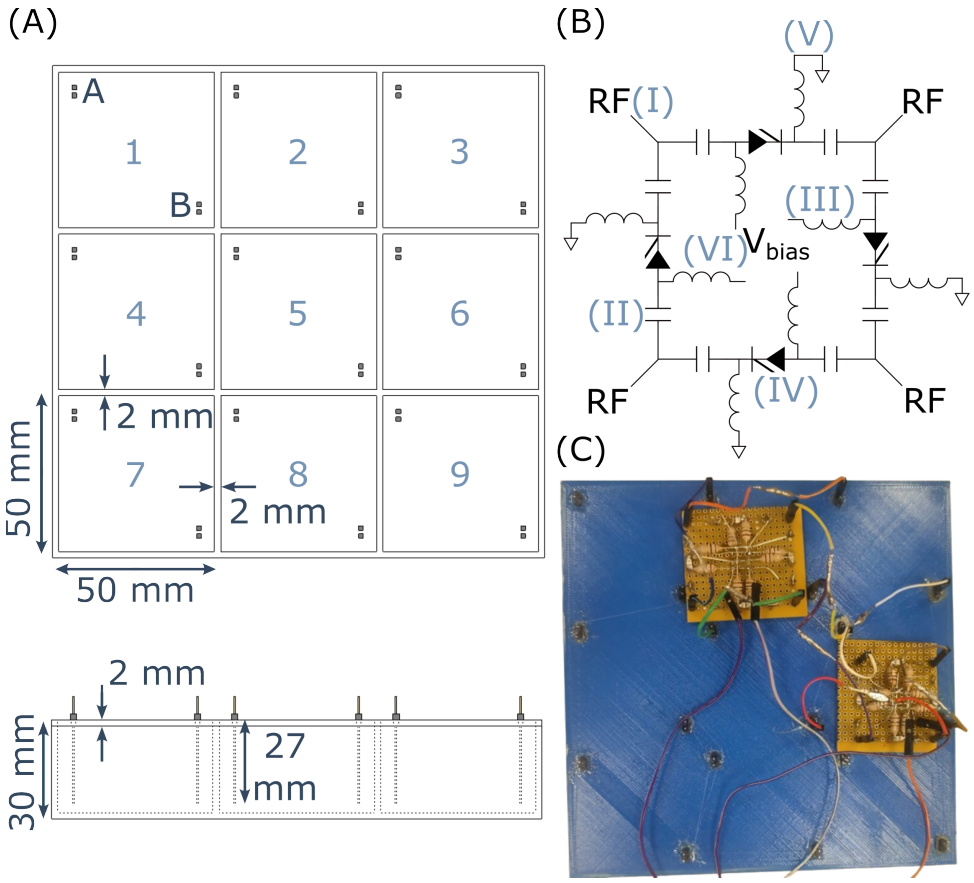

Figure 3.1.: Switchable dielectric shimming prototype. (**A**) Schematic overview of the 3×3 array of dielectric elements with a single element width of 50 mm, height 30 mm, electrode length 27 mm, and inter-element gap width of 2 mm. The array elements and connectors are labeled (1-9, A-B) in blue for reference purposes. (**B**) Schematic diagram of the RF switching circuit for interconnecting four elements of the dielectric array. (I) Header pin connector. (II) DC choke. (III) RF choke. (IV) PIN diode. (V) Ground. (VI) Bias voltage (V_{bias}). (**C**) 3D-printed polylactic acid container, filled with a 25% v/v barium titanate slurry (estimated relative permittivity of 165). An epoxy layer was applied on the inside for waterproofing, and the container was sealed using universal adhesive. The switching mechanism is shown connecting four adjacent elements in parallel (2A-3A-6A-5A-2A and 2B-3B-6B-5B-2B). The bias voltage is applied to each printed circuit board using a pair of jumper wires (visible at the bottom).

As dual-channel transmit systems are offered by most vendors as part of top-of-the-line system architecture and require expensive upgrades or replacements in conventional implementations, pTx does not always provide a sustainable solution for existing and older systems.

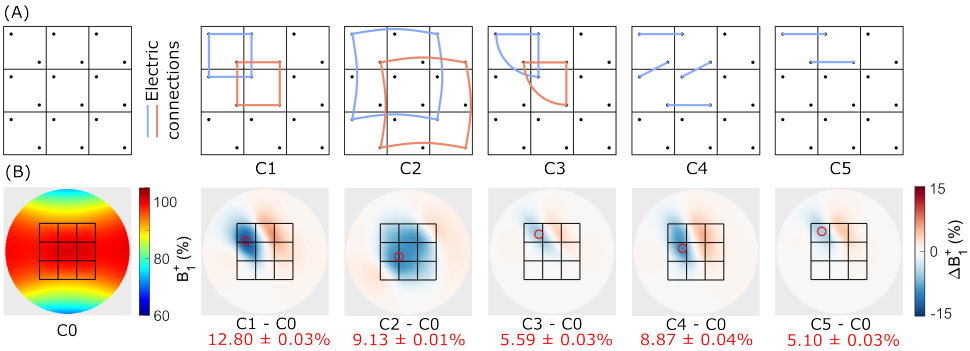

Figure 3.2.: Simulated B_1^+ modulation for several interconnection configurations. (**A**) Schematic representation of a 3×3 array of dielectric elements with different interconnection configurations. C0 represents the reference case without any interconnections. (**B**) B_1^+ difference maps evaluated at a depth of 15 mm inside the cylindrical phantom. The first subplot shows an absolute B_1^+ map for the reference configuration (C0, center value defined as 100%). Subsequent subplots show the B_1^+ difference of each of the interconnected configurations (C1-C5) compared to the reference (C0). The outline of the dielectric array is shown in black, and the measurement regions of interest (ROIs) are indicated by a red circle.

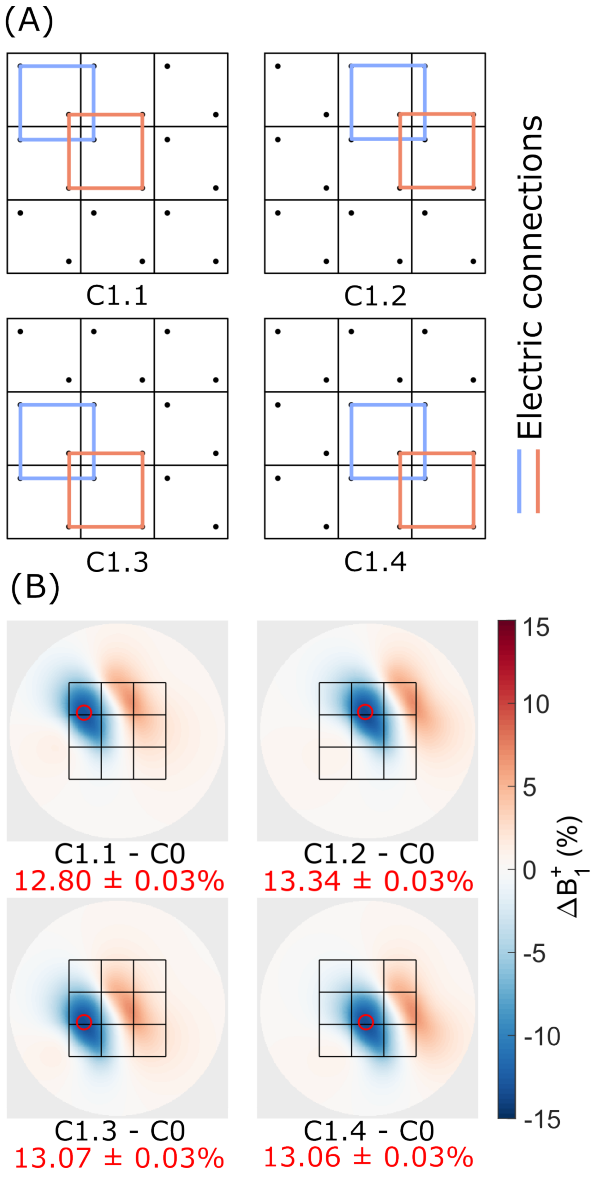

Figure 3.3.: Simulated B_1^+ modulation produced by the C1 configuration translated within the array of dielectric blocks. (**A**) Schematic representation of C1 evaluated for four subsets of 2×2 blocks in the array. (**B**) Normalized modulation of the B_1^+ field plotted as a difference between the coupled configuration and the uncoupled reference C0.

An alternative for B_1^+ shimming is the use of dielectric materials, often termed "dielectric pads" or "dielectric shimming". These pads typically consist of materials with high relative permittivity (ϵ_r) such as water, titanate suspensions [82, 83] or solid ceramics [84, 85]. These pads are placed on the subject close to the area of interest. During RF transmission a displacement current is induced in the high permittivity material, which in turn, gives rise to a secondary magnetic field. This field is superimposed onto the field generated by the RF transmit coil, improving the B_1^+ field homogeneity in the artifact-affected areas [86]. Several studies have demonstrated promising improvements of the B_1^+ homogeneity using barium titanate suspension pads in body MRI at 3T [87, 88]. Although dielectric pads offer a cheap solution to improve B_1^+ homogeneity, the optimal design of the pad geometry and dielectric properties is application- and, ultimately, subject-specific. As a result, the clinical use of the dielectric pads is limited to the use of a single "one-size-fits-all" design, involving compromises on the RF shimming performance.

In this work, we aim to improve the adaptability of dielectric shimming using an array of small dielectric elements that are electrically interconnected. The connections between the elements can be switched using PIN diodes to change the B_1^+ field modulation. Electromagnetic (EM) simulations were performed to optimize the configuration and to study the effect of varying the dielectric permittivity. A 3D-printed array of cavities filled with a high permittivity titanate suspension was used for in-situ B_1^+ shimming experiments at 3T. The B_1^+ field modulation was measured in two different phantoms, using various connection patterns and multiple depths below the phantom surface.

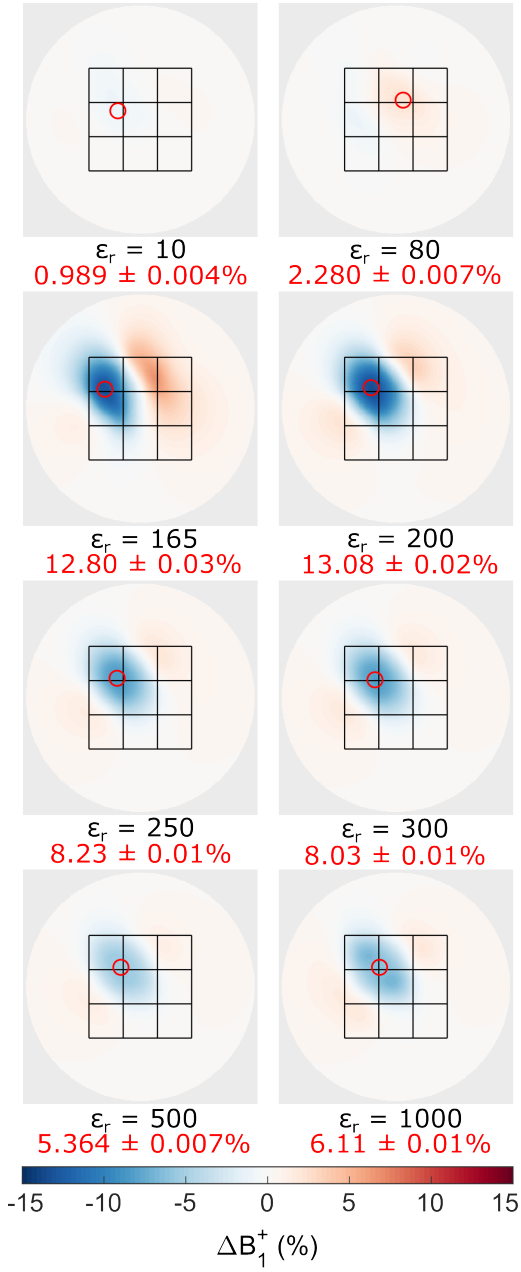

Figure 3.4.: Simulated B_1^+ modulation showing the difference between configuration C1.1 and an uncoupled case C0 for various relative permittivity values of the dielectric elements.

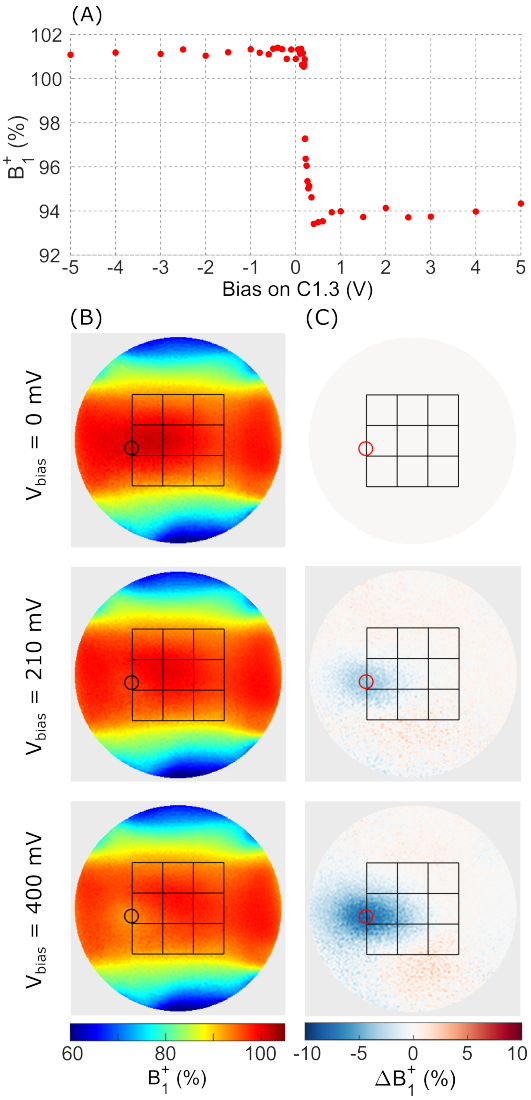

Figure 3.5.: Adaptive B_1^+ modulation of the dielectric array measured in a disk-shaped phantom using C1.3 configuration. (**A**) B_1^+ (percentage of nominal value) in a circular ROI plotted as a function of applied bias voltage V_{bias}, showing increased B_1^+ modulation at high V_{bias} as the resistance across the PIN diodes decreases. (**B**) the absolute and (**C**) normalized B_1^+ maps for three bias voltages. The circular ROI used to extract the data in (**A**) is indicated in black. (**C**) Relative B_1^+ maps showing the difference between the B_1^+ maps of (**B**) and a reference case of 0 V bias voltage, with the ROI indicated by a red circle.

3.3. METHODS

The proposed approach is based on multiple small, sub-wavelength-sized dielectric elements, which can be electrically coupled using switchable connections to modulate the B_1^+ field. To this end, a prototype device was designed as a 3×3 array of cubical cavities (50 mm×50 mm×30 mm^3, 2 mm separation, Figure 3.1A). Each cavity is electrically insulated and filled with a high permittivity material. Sets of two electrode connectors (A and B) are brought into contact with each element to enable inter-element connections.

3.3.1. EM SIMULATIONS

Electromagnetic simulations were performed in CST (CST Studio Suite 2023, Dassault Systèmes, France) to model the B_1^+ field of a 3T MRI system. A 16-rung high-pass birdcage coil (diameter = 73 cm, length = 56 cm) was driven in circular polarization mode (i.e. applying a 22.5° phase shift between each successive rung). The coil was shielded by a copper cylindrical sheet (diameter = 79 cm, length = 100 cm).

A disk-shaped mineral oil phantom (diameter = 36 cm, height = 10 cm, ϵ_r = 2.1, σ = 0.001 S/m)) was placed horizontally in the center of the coil. A 3×3 array of dielectric blocks (width = 50 mm, height 30 mm) was placed on top of the phantom, aligned with the center. The default relative permittivity of the dielectric material was set to 165 unless stated otherwise, whereas the conductivity was set to σ = 0.25 S/m in all simulations. For electrode connections, two copper rods (diameter = 2.5 mm, length = 37.5 mm) were placed in the top-left and bottom-right corner of each dielectric block at a 5 mm offset from the edge and extending down to 3 mm above the bottom of each block.

A time domain solver was set up to solve for the electromagnetic fields at 128 MHz in the simulation model. A non-uniform hexahedral mesh with minimal spacing of 3.5 mm around the phantom and coarser spacing outside the phantom was used for sufficient sampling of the gaps between the dielectric elements while minimizing the computation times. The simulated B_1^+ field was normalized to 1000 W of stimulated power and evaluated at 15 mm below the phantom surface.

Five different serial and parallel circuits between subsets of the dielectric array were studied to determine which interconnections produce a strong modulation of the B_1^+ field. Circuit connections were simulated by using perfectly conducting wires with a length of 6-11 cm (minimal connector-to-connector length, rounded to the nearest larger integer) and a radius of 0.2 mm. For parallel circuits, three versions were investigated: one connecting three adjacent elements (1A-2A-5A-1A and 1B-2B-5B-1B connections); four adjacent elements (1A-2A-5A-4A-1A and 1B-2B-5B-4B-1B); and four non-adjacent elements, with an additional gap (1A-3A-9A-7A-1A and 1B-3B-9B-7B-1B). For serial

circuits, two versions were simulated: adjacent four-element connection (1A-2A, 2B-5A, 5B-4B, and 4A-1B) and adjacent two-element connection (1A-2A and 1B-2B). Longer wire lengths were also studied by simulating 4 cm, 8 cm and 12 cm extensions to the individual connections.

To quantify the modulation strength, B_1^+ differences were measured between the wired configurations and one reference configuration without any connections. For each configuration, a circular region-of-interest (ROI) was defined, centered at the point with maximum absolute modulation, with a radius of 11.7 mm to match the further phantom experiments. The configuration that induced the maximal change in B_1^+ was selected for use in further simulations and phantom experiments.

Subsequently, different subsets of array elements were connected using the optimized interconnections and compared to the uncoupled case in order to determine if the shimming effect can be spatially shifted. Finally, the relative permittivity of the dielectric was studied in order to evaluate the impact of dielectric properties on the device performance. In particular, ϵ_r was varied to resemble water (ϵ_r = 80), 25% volume barium titanate suspension in water (v/v) (ϵ_r = 165)[82, 83], compressed metal titanates (ϵ_r = 500) [89], and ceramics (ϵ_r = 1000) [84, 85]. Finally, a low relative permittivity (ϵ_r = 10) and a few intermediate values (ϵ_r = 210, 255, 300) were evaluated.

3.3.2. EXPERIMENTAL PROTOTYPE

A prototype device was constructed using polylactic acid (PLA) on a commercially available 3D-printer (Sigma D25, BCN3D Technologies, Spain). A thin layer of epoxy resin was applied to the inner faces of the container to prevent water evaporation. Each cavity was filled with a 25% v/v suspension of barium titanate in distilled water. This ratio was chosen for its known dielectric properties at 3T (ϵ_r = 165), close to the saturation limit [83].

After filling, the container was sealed with a 2 mm thick 3D-printed PLA lid that was mounted using a universal adhesive. The inner side of the lid was also coated with epoxy resin for waterproofing. A pair of header pins (PRPC040SACN-RC, Sullins Connector Solutions, United States) was inserted at two opposing corners of each dielectric element, at a distance of 5 mm to the lateral edges. A 27 mm copper wire was lowered into the dielectric to enable the electrical connections. The prototype is depicted in Figure 3.1C.

3.3.3. RF SWITCHING

MRI-compatible RF switches were designed to modulate the RF current generated in an interconnected subset of the dielectric elements. MR-compatible PIN diodes (MA4P7470F-1072T, MACOM Technology Solutions) were used to switch interconnections based on the applied

bias voltage. RF chokes (1 μH, 05CCM-1R0M-01, Fastron Group, Germany) and DC blocking capacitors (10 nF, VJ0402Y103KCAAC, Vishay, United States) were used to minimize RF coupling to the circuitry and direct the bias voltage to a single diode. The bias voltage was provided from the control room by a function generator (AFG31022, Tektronix, United States) connected to the RF switches in the scanner.

To study the optimized configuration, the RF switch was designed to interconnect four connecting points on the prototype. Each switch featured four PIN diodes, four header pins, eight DC chokes, and eight RF chokes (Figure 3.1B). The four PIN diode connections were grouped for simultaneous application of the bias voltage. The four header pins were connected to the container using 10 cm AWG 26 jumper wires. For connecting 2×2 shim array subsets of adjacent elements in a parallel circuit (e.g. 1A-2A-5A-4A-1A and 1B-2B-5B-4B-1B for connecting elements 1, 2, 4, and 5), two switches were used.

3.3.4. B_1^+ MAPPING

Phantom experiments were performed on a 3T MR system (Ingenia, Philips Healthcare, the Netherlands). B_1^+ maps were obtained using a Dual Refocusing Echo Acquisition Mode (DREAM) sequence (3x3 mm^2 in-plane resolution, 10 mm slice thickness, FOV = 450×450 mm^2, TR/TE = 4.6/1.9 ms, Imaging/STEAM flip angle = 15/60 °) [90]. RF shimming was evaluated in a disk-shaped phantom (diameter = 36 cm, height = 10 cm) filled with mineral oil (SpectraSyn 4, ExxonMobil, United States) and a ballistic gel torso (51×46×23 cm^3, $T_1 \approx 169$ ms, $T_2 \approx 39.2$ ms, Clear Ballistics, Unites States), which was used to mimic the human torso dimensions. B_1^+ maps were acquired approximately 15 mm below the surface of both phantoms.

First, the effect of the bias voltage was studied, acquiring B_1^+ maps in the cylindrical phantom for the bottom-left 2×2 block connection, corresponding to dielectric elements 4, 5, 7, and 8. The bias voltage was varied between -5 V and 5 V, with 41 sampling steps, with a higher sampling density around the PIN diode activation between 0-1 V. One repetition per bias voltage was performed, and the B_1^+ modulation was evaluated in a small circular ROI with 11.7 mm radius (equivalent to 10 voxels in the reconstructed image).

Next, translation of the interconnection was studied by testing different circuit placements: connecting elements 1, 2, 4, and 5; elements 2, 3, 5, and 6; elements 4, 5, 7, and 8; elements 5, 6, 8, and 9. For this, a 5 V bias voltage was applied, comparing B_1^+ modulation to a reference case of 0 V. The maps were acquired with ten repetitions for each bias voltage in a cylindrical phantom and gel-torso, and the shimming effect was evaluated in each case over the small circular ROIs displaying the strongest modulation. The translatability was evaluated

by estimating 2D correlation coefficient for the B_1^+ modulation area right below the connected 2×2 array subset. Additionally, paired sample t-tests were performed for mean modulation within the ROIs, considering the Bonferroni correction-adjusted significant level of 0.01.

Finally, the B_1^+ modulation was studied as a function of depth in the gel-torso. B_1^+ maps were acquired at 5, 10, 15, 20, 25, 30, 35, 45, 55, 65, 75, 85, and 95 mm depths with a 5 V bias voltage applied to the PIN diodes. A reference map with 0 V bias voltage was also obtained for each slice. Three repetitions per slice were acquired for each bias voltage and depth. The maps were acquired using elements 2, 3, 5, and 6 connection as a representative configuration. For every slice, the B_1^+ modulation was evaluated for a small circular ROI.

3.4. RESULTS

3.4.1. EM SIMULATIONS

EM simulations for several interconnection configurations show statistically significant B_1^+ field modulation ($p<0.001$, see Figure 3.2). A peak modulation of up to 12.8% is observed for four neighboring elements connected in a parallel circuit (C1). Alternative configurations with adjacent element connections (C3-C5) achieved a relatively weak modulation of up to 5.6%, 8.9%, and 5.1%, respectively. Parallel configuration with non-adjacent connections of four blocks (C2) achieved 9.2% modulation, albeit much less localized. Notably, the modulation produced by all configurations studied was predominantly negative. Simulations with extended connection wire lengths showed a reduced B_1^+ field modulation, indicating that interconnecting wire length should be kept minimal (See Figure S3.1.

The optimized circuit (C1) was shifted to multiple positions across the dielectric array, to study the spatial translation of the B_1^+ modulation as shown in Figure 3.3. Upon moving the circuit connection to a different 2×2 subset of blocks (C1.1-C1.4), good translation of B_1^+ modulation pattern was observed. When comparing the B_1^+ modulation obtained in C1.1 directly below the corresponding elements (i.e. the area below elements 1, 2, 4, and 5) with that obtained in C1.2 - C1.4, the correlation coefficients are 0.9982, 0.9998, and 0.9988, respectively. The area of maximum B_1^+ field modulation was observed directly underneath the coupled blocks, reaching 12.8%, 13.3%, 13.1%, and 13.1% modulation for C1.1-C1.4 configurations, respectively.

The B_1^+ modulation achieved by the shimming array showed a strong dependence on the relative permittivity of the dielectric material, as illustrated for the C1.1 configuration in Figure 3.4. A low-permittivity ($\epsilon_r = 10$) and water model ($\epsilon_r = 80$) result in a weak B_1^+ modulation of 0.99% and 2.28%, respectively. Maximum modulations of 13.1% and

12.8% are achieved by $\epsilon_r = 200$ and $\epsilon_r = 165$. Increasing the relative permittivity value above 250 resulted in a decreased modulation.

3.4.2. PHANTOM RESULTS

The B_1^+ modulation was evaluated as a function of the bias voltage V_{bias} in the disk-shaped phantom by gradually increasing the bias voltage V_{bias} across the PIN diodes (see Figure 3.5C). A steep onset was observed around V_{bias} =200-400 mV, reaching a plateau at around 800 mV with mean B_1^+ of 93.94±0.04%. Negligible variation is observed for negative bias voltages (mean normalized B_1^+ of 101.18±0.03%). Accordingly, the configuration C1.3 achieves up to 7.24±0.03% B_1^+ modulation.

Similar to simulations, the B_1^+ modulation in both the disk-shaped and gel-torso phantoms showed consistent spatial translation, when different 2×2 subsets of blocks were connected in configuration C1. Larger differences in the modulation patterns between the different subsets were observed in the experiments compared to simulations. Accordingly, a lower correlation coefficients between the modulation patterns for C1.2-C1.4 and C1.1 as reference was observed in the cylindrical phantom (C1.2 vs C1.1: 0.896, C1.3 vs C1.1: 0.961, and C1.4 vs C1.1: 0.762). In C1.1-C1.4, maximum B_1^+ modulation of 6.13±0.03%, 6.40±0.04%, 10.72±0.02%, and 3.35±0.02% was observed for the disk-shaped phantom, respectively (see Figure 3.6A, $p<0.001$). In the gel-torso phantom, comparable B_1^+ modulation was achieved reaching 6.75±0.13%, 11.58±0.22%, 7.11±0.14%, and 3.35±0.16% for C1.1-C1.4 (see Figure 3.6B, $p<0.001$). Correlation coefficients upon translation of C1.2-C1.4 with respect to C1.1 were 0.887, 0.986, and 0.929, respectively.

The B_1^+ variation with depth within the gel-torso phantom showed a gradual decay of the B_1^+ modulation when moving further away from the dielectric array (see Figure 3.7). The B_1^+ modulation reaches up to 25.0±2.9% near the phantom surface, and is still measurable at 95 mm below the surface (1.12±0.05%). At 25-40 mm depth, which is typical for cardiac anatomy, 4-8% modulation is achieved.

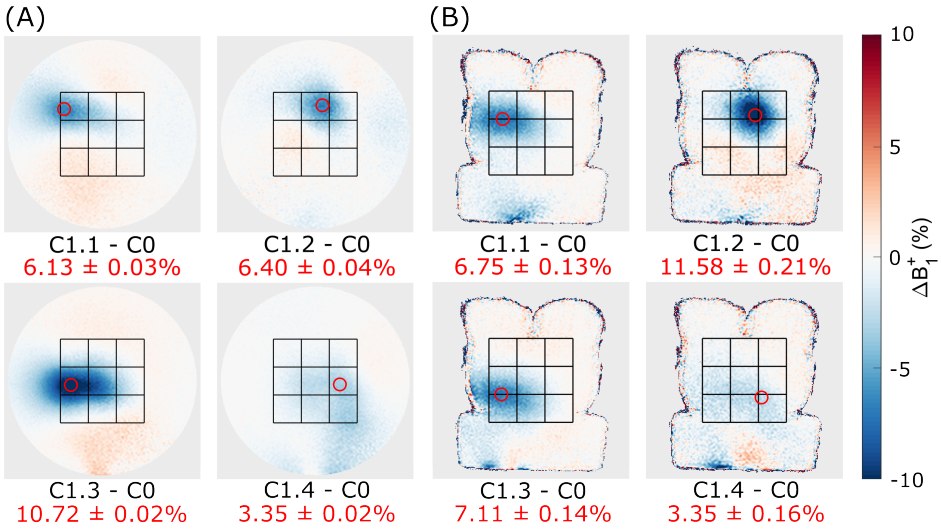

Figure 3.6.: Modulation of the B_1^+ field in the two phantoms produced by the C1 configuration translated within the dielectric shimming array. The maps are shown as a difference between the 5 V bias and a 0 V reference state (C0). (**A**) Modulation patterns in the disk-shaped phantom. (**B**) Modulation patterns in the torso phantom. The coupling configuration and modulation in the ROIs (red circle) is stated below each subplot.

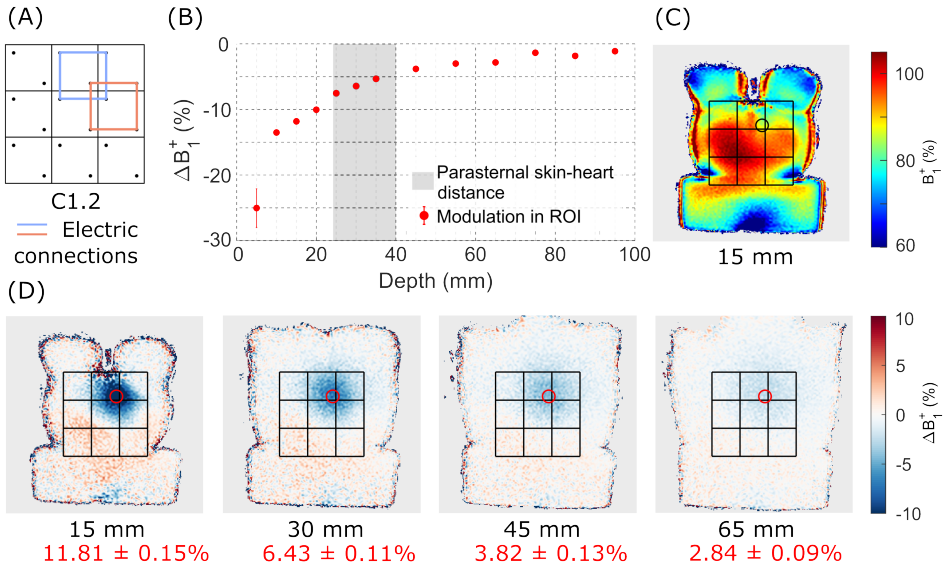

Figure 3.7.: B_1^+ shimming effect in the gel-torso phantom for slices at various depths under the dielectric array. (**A**) The top-right 2×2 blocks were interconnected (C1.2) using a 5 V forward bias voltage. (**B**) B_1^+ modulation as a function of imaging depth, measured in the ROI indicated by a black or red circle in (**C-D**). The shaded gray area shows the parasternal skin-to-heart distance within one standard deviation from the mean distance [91]. (**C**) Absolute B_1^+ map acquired 15 mm below the phantom surface. (**D**) B_1^+ modulation for slices at exemplary depths.

3.5. DISCUSSION

In this study, a proof-of-principle device for adaptive B_1^+ field shimming in MRI was built using an array of interconnected dielectric elements. EM simulations indicated that shifting a set of parallel connections across the shimming array enables targeted spatial modulation of the B_1^+ field. Accordingly, phantom experiments using PIN diode-based RF switches between elements filled with dielectric slurry show significant and controllable spatial modulation of the B_1^+ field. This demonstrates a promising proof-of-principle for realizing adjustable B_1^+ shimming effects using dielectric materials, as a cost-effective solution for B_1^+ shimming in high field MRI.

From the investigated set of different interconnection configurations in EM simulations, four adjacent blocks connected in parallel were chosen for the phantom experiments due to the achieved focal field modulation. Notably, the configuration produced predominantly negative B_1^+ field modulation, i.e. reducing the total B_1^+ field amplitude. This could prove valuable in reducing RF-induced heating around implants [92], or to homogenize the transmit field by locally suppressing hyper-enhanced B_1^+ areas. However, in order to correct areas affected by signal dropout, a positive B_1^+ field modulation would be more beneficial in terms of RF power efficiency. Simulation results indicate that various device properties, such as the exact permittivity of the dielectric material, or the length of the coupling wires can substantially change the modulation pattern, potentially shifting from negative to positive modulation. In addition to the modulation polarity, the absolute magnitude of the induced B_1^+ field modulation also warrants further investigation. In the current design, up to 11% absolute modulation was observed at a depth of 15 mm below the device. Considering the typical levels of B_1^+ inhomogeneity ranging from 30-50 % for body imaging at 3T [8], further improvements in the shimming magnitude are needed to achieve sufficient RF field control in clinical applications. Future device optimization will therefore include tuning of the dielectric properties, as well as the geometry of the dielectric elements and interconnections, in order to fully exploit the potential for B_1^+ field correction.

PIN diode switches were used to enable control of the B_1^+ modulation magnitude in this work, operated either in reverse or forward bias. Based on the bias voltage analysis, where a smooth modulation magnitude function was observed, one might consider driving the diodes close to the activation voltage, to provide intermediate levels of B_1^+ field modulation. While PIN diodes proved to be effective, metal–oxide–semiconductor field-effect transistors (MOSFETs) or microelectromechanical systems (MEMS) switches can be further explored as MR-compatible alternatives to enable RF switching functionalities. These alternatives may benefit from decreased power consumption, potentially enabling completely

wireless implementations of the device. Furthermore, MOSFET or MEMS switches can also reduce ohmic losses in the device and improve efficiency, as it requires a fewer total number of components.

In the current prototype, the B_1^+ field modulation was optimized for modulation magnitude rather than total B_1^+ homogeneity. Improving this requires further tailoring of the element combinations. In an experimental setting, one might start by mapping the initial B_1^+ field, followed by semi-automated activation of dielectric elements close to the region of interest. Iterative application of B_1^+ mapping and adjustment of the switching modes can allow for robust and adaptive RF field homogenization in a subject-specific manner. The duration of such a calibration procedure would be largely determined by the scan time required for B_1^+ mapping, which can be achieved within seconds [90, 93], potentially allowing for automated calibration within a clinically acceptable time-frame of approximately 30 seconds.

Various design improvements are warranted to bring the prototype closer to clinical use. For body and cardiac MRI, larger arrays with an increased number of elements should be considered to provide sufficient coverage and increased degrees of freedom for tailoring the spatial modulation pattern. Furthermore, a flexible body-conforming array can be constructed to improve both patient comfort and effect size due to a decreased separation between the dielectric and the skin. Such a device could also be integrated with receive coil geometries, such as chest arrays or head coils. This would be particularly useful for brain imaging at ultra-high field strengths such as 7T, where the B_1^+ field exhibits even stronger inhomogeneity patterns compared to 3T. To ensure that the device fits the limited space inside the close-fitting head coil, thinner dielectric elements with increased permittivity can be explored.

The current work has several limitations. Firstly, only a small number of potential electrical connections was studied. The current results warrant further investigation to explore additional interconnections with different layouts, the individual dielectric element properties, and the achieved B_1^+ modulation pattern. Furthermore, in EM simulations, the B_1^+ field modulation was only studied in the oil phantom, which can be extended to anatomical body models for further optimization of the effects. Various human body models could be used to establish robust and reproducible shimming across a range of subjects. Finally, the current prototype has only been evaluated in phantom imaging. Further in-vivo studies will be needed to validate the effectiveness and quantify the achieved B_1^+ modulation, while ascertaining safety in terms of RF-induced heating due to the device and adjacent tissue [94].

3.6. CONCLUSION

In this work, a cost-effective method for adaptive modulation of the B_1^+ field in high field MRI using reconfigurable dielectric materials is proposed. The proof-of-principle demonstration shows reproducible and localized modulation of the B_1^+ field in simulations and phantom experiments. A B_1^+ field modulation magnitude of up to 11% was observed in phantom measurements 15 mm below the surface. Further optimization of the material properties and the design parameters is warranted to increase the effectiveness further. This provides a promising alternative towards adaptive and cost-effective B_1^+ shimming without the need for multiple transmit coils and associated hardware and software requirements.

3.7. DATA AVAILABILITY

All experimental data can be found at https://gitlab.tudelft.nl/mars-lab/active-dielectric-shimming.

3.8. SUPPLEMENTARY MATERIALS

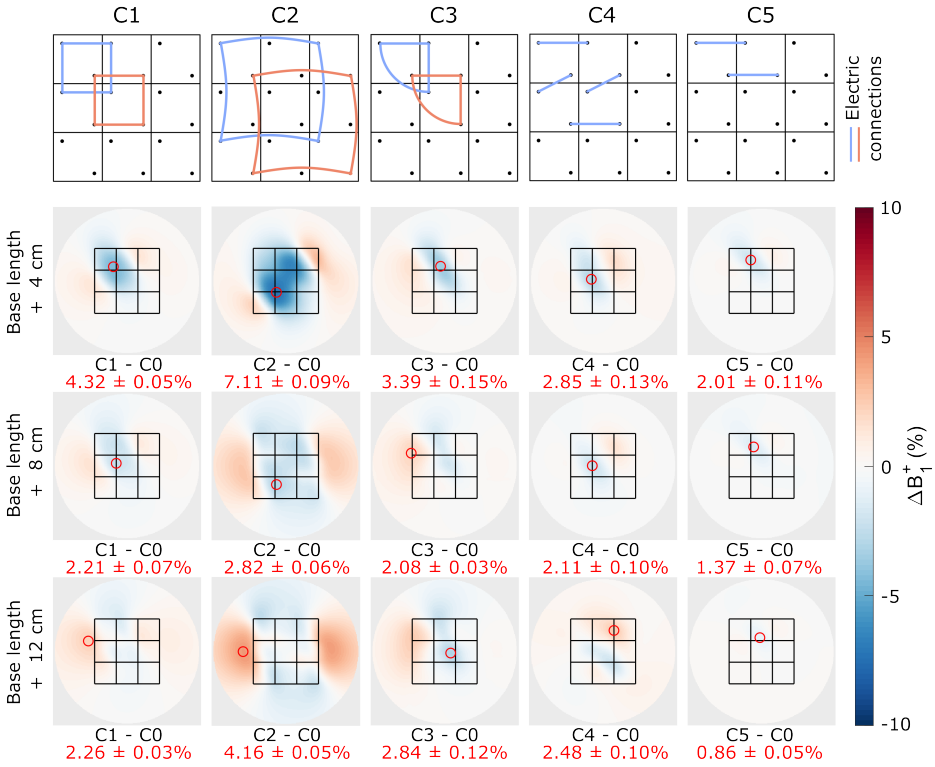

Figure S3.1.: Simulated B_1^+ modulation for several studied coupling configurations. (**A**) Schematic representation of a 3×3 array of dielectric pockets with different coupling configurations. C0 is uncoupled and is provided as a reference case. (**B**) B_1^+ difference maps evaluated at a depth of 15 mm inside the cylindrical phantom and normalized to 1000 W of stimulated power. Each subplot shows the difference in the normalized B_1^+ field of the coupled case (C1-C5) and the baseline C0. The outline of the cask is shown in black, and the considered ROIs are indicated by a red circle. The first subplot shows an absolute B_1^+ map for the uncoupled case C0.

II

PART TWO
MRI PULSE SEQUENCE DESIGN

4

MYOCARDIAL TISSUE CHARACTERIZATION

This chapter is based on the following publication: Guo, R., Weingärtner, S., Šiurytė, P., T. Stoeck, C., Füetterer, M., E. Campbell-Washburn, A., Suinesiaputra, A., Jerosch-Herold, M., Nezafat, R. (2021). Emerging techniques in Cardiac Magnetic Resonance Imaging. Journal of Magnetic Resonance Imaging, 55(4), 1043-1059. https://doi.org/10.1002/jmri.27848.

4.1. ABSTRACT

Cardiovascular disease is the leading cause of death and a significant contributor of health care costs. Noninvasive imaging plays an essential role in the management of patients with cardiovascular disease. Cardiac magnetic resonance (MR) can noninvasively assess heart and vascular abnormalities, including biventricular structure/function, blood hemodynamics, myocardial tissue composition, microstructure, perfusion, metabolism, coronary microvascular function, and aortic distensibility/stiffness. Its ability to characterize myocardial tissue composition is unique among alternative imaging modalities in cardiovascular disease. Significant growth in cardiac MR utilization, particularly in Europe in the last decade, has laid the necessary clinical groundwork to position cardiac MR as an important imaging modality in the workup of patients with cardiovascular disease. Although lack of availability, limited training, physician hesitation, and reimbursement issues have hampered widespread clinical adoption of cardiac MR in the United States, growing clinical evidence will ultimately overcome these challenges. Advances in cardiac MR techniques, particularly faster image acquisition, quantitative myocardial tissue characterization, and image analysis have been critical to its growth. In this review article, we discuss recent advances in established and emerging cardiac MR techniques that are expected to strengthen its capability in managing patients with cardiovascular disease.

4.2. MYOCARDIAL TISSUE CHARACTERIZATION

Cardiac MR can noninvasively assess heart and vascular abnormalities, including biventricular structure/function, blood hemodynamics, myocardial tissue composition, microstructure, perfusion, metabolism, coronary microvascular function, and aortic distensibility/stiffness (Figure 4.1). One of the main advantages of cardiac MR over other cardiac imaging modalities is its ability to noninvasively characterize myocardial tissue composition.

Evaluation of myocardial viability with late gadolinium enhancement (LGE) is the most common indication for a cardiac MR examination. In the LGE sequence, T_1-weighted images are collected after an inversion pulse. Due to differences in T_1 times between healthy and scarred myocardium, the scar appears bright. However, use of an incorrect inversion time may result in artifactual enhancement. Phase-sensitive inversion recovery (PSIR) was introduced to preserve information about longitudinal magnetization polarity [95]. To further improve blood-scar contrast for better visualization of sub-endocardial scars, dark blood LGE (DB-LGE) sequences were developed [96–100]. In DB-LGE, additional contrast mechanisms such as T_2 preparation or magnetization transfer (MT) are exploited to enhance blood-scar contrast. In the first

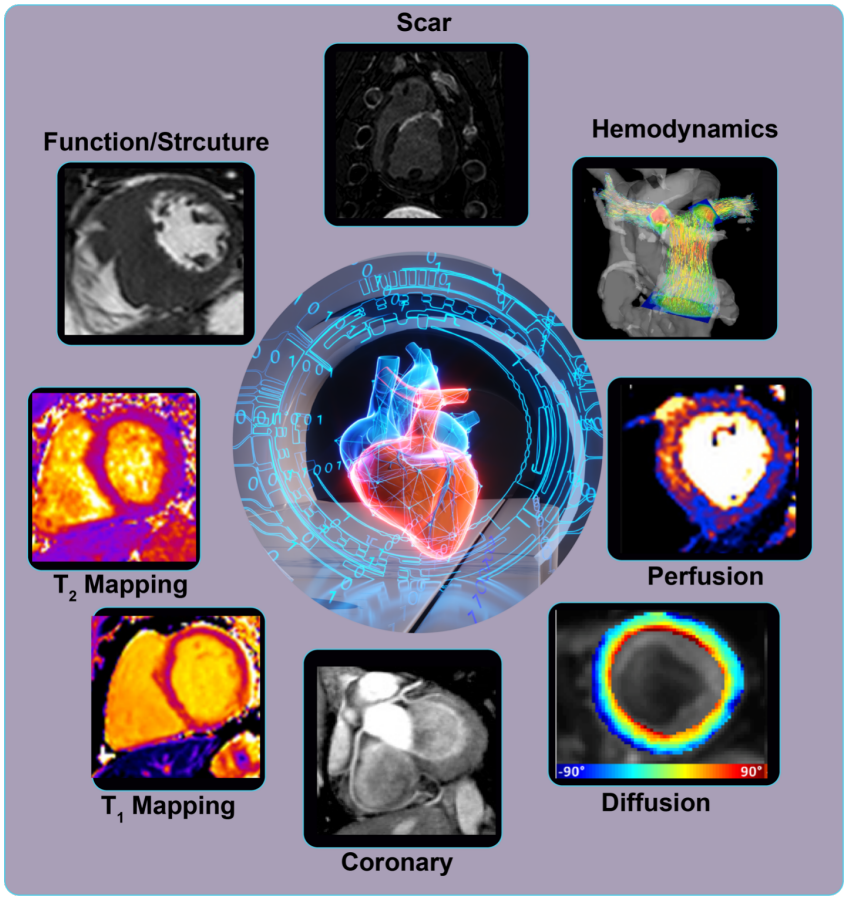

Figure 4.1.: Cardiac MR imaging provides a comprehensive assessment of the structure, function, perfusion, viability, hemodynamics, microstructure, and myocardial mapping via T_1, T_2, and T_2^*. The imaging protocol typically includes basic function, structure, flow, and the remaining necessary sequences are tailored based on the patient indication with a typical scan time of 45–60 minutes.

approach, T_2 preparation is used in addition to inversion pulse, with sequence timings configured to suppress the signal from both the blood and normal myocardium [96, 97]. Similarly, a combination of MT off-resonance excitations and inversion recovery achieves dark-blood contrast [98]. Gray-blood LGE has also been introduced to retain some blood pool signal, with the potential for improved anatomical assessment [99]. These specialized sequences require additional steps to optimize the new imaging parameters and achieve blood signal suppression. A PSIR-specific inversion time optimization has also

been used to achieve DB-LGE without additional preparation sequences [100]. LGE is commonly acquired using a series of twodimensional (2D) slices. However, recent advances in accelerated imaging and respiratory motion correction have enabled whole heart three-dimensional (3D) LGE, allowing higher spatial resolution and whole heart coverage, albeit with significantly longer scan times [101]. Advanced accelerating techniques such as compressed sensing (CS) [101, 102] and, most recently, deep learning (DL)-based reconstructions [103] can be used to further reduce the scan time.

LGE imaging requires the administration of a gadolinium-based contrast agent (GBCA). Indeed, the majority of cardiac MR examinations are performed with GBCA. There are currently two classes of GBCA available for cardiac MR examinations: linear and macrocyclic, each with varying properties and safety profiles. With emerging data on the superior safety of macrocyclic GBCA, cardiac MR examinations are mainly performed using a macrocyclic agent with a favorable safety profile [104]. Intravascular "blood-pool" contrast agents (e.g., gadofosveset trisodium (Ablavar^{TM})) have been previously used for vascular imaging and are highly popular in pediatric cardiac imaging. However, they are no longer clinically available. Therefore, macrocyclic GBCA agents are currently the most widely used agents in cardiac MR.

In addition to myocardial viability, cardiac MR can assess the presence of diffuse interstitial fibrosis via T_1 and extracellular volume mappings, edema via T_2 mapping, and iron via T_2^* mappings [105]. Numerous techniques have been proposed to perform T_1 mapping of the heart [106]. Most of these techniques are based on a T_1 sensitizing preparation, such as inversion or saturation pulse combined with a snapshot imaging readout, each with a distinct profile of advantages and disadvantages. An overview of the typical components of cardiac mapping sequences is provided in Figure 4.2.

Modified Look-Locker Imaging (MOLLI) [107] is the only commercially available cardiac T_1 mapping sequence. Myocardial T_1 mapping with MOLLI is collected during a single breath-hold per slice with coverage of one to three slices. The analysis involves the manual drawing of the region of interest to delineate the myocardial signal for calculating global and regional T_1 values. A septal T_1 measurement is the most reproducible approach for quantification of global diffuse fibrosis in T_1 mapping. Saturation recovery-based T_1 mapping sequences (e.g., SASHA [108] and SAPPHIRE [109]) are alternatives to inversion recovery-based sequences with improved accuracy, albeit reduced precision compared to MOLLI [110]. Despite the potential of alternative existing T_1 sequences to overcome several MOLLI confounders such as T_2 sensitivity, these sequences are only available for research purposes and not offered as a product by any magnetic resonance imaging (MRI) vendor. To improve patient comfort, free-breathing T_1

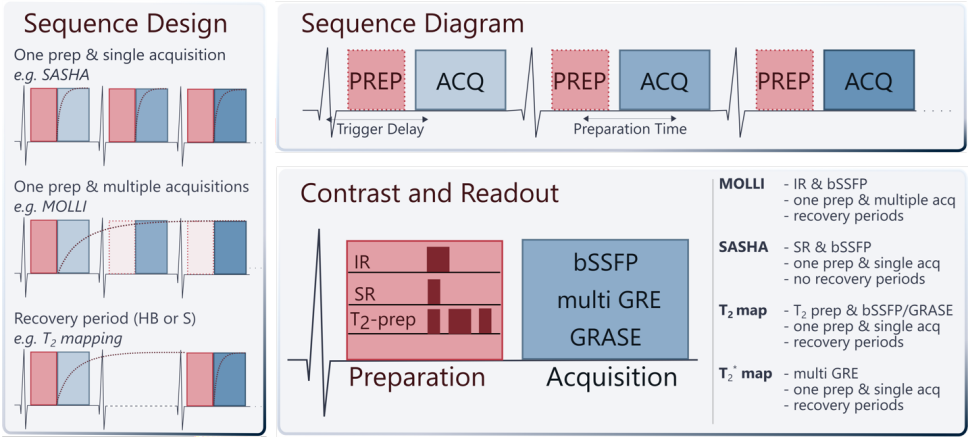

Figure 4.2.: Commonly used myocardial tissue mapping sequences for evaluation of T_1, T_2, and T_2^*. The overall sequence design (left) describes ways of arranging preparation/acquisition blocks throughout the sequence duration and shows a schematic of the magnetization recovery curve (red dashed line). HB (heartbeats) and S (seconds) have been used as a unit for the recovery period. The sequence diagram (top right) depicts the layout of preparation and acquisition modules relative to the ECG. Dashed borders indicate that the preparation blocks may be left out depending on the sequence design. The contrast and readout (bottom right) list common choices for these building blocks. Each mapping sequence has a unique combination of the sequence design, trigger/ preparation delay, preparation, and acquisition block.

mapping, primarily based on the diaphragmatic navigator, has also been implemented.

T_2^* mapping is commonly achieved using multigradient echo readouts with variable echo times. Most modern techniques use dark blood contrast, acquired in the late diastole phase, where a double inversion recovery pulse is employed to null the blood signal and alleviate partial voluming effects [111]. A free-breathing alternative for T_2^* mapping was proposed, using single-shot imaging with multiple repetitions and motion correction in postprocessing [112]. T_2 mapping is commonly based on T_2 magnetization preparation modules combined with single-shot image readouts [113, 114]. Rest periods are inserted between different acquisitions, allowing for signal recovery. Alternatively, saturation preparation avoids rest periods at the cost of reduced signal-to-noise ratio (SNR) [115]. A two- or three-parameter fit model can be used for estimating T_2 values from T_2-weighted images [116]. Alternative sequence designs based on gradient- and spin-echo readout have also been proposed, potentially allowing gains in acquisition efficiency [117].

Finally, several free-breathing T_2 sequences emerged for multislice 2D/3D acquisitions with higher spatial coverage and spatial resolution [115, 118–120].

There have been recent advances in multiparametric mapping to simultaneously measure different tissue contrasts to reduce overall scan time and simplify the examination. Joint T_1 and T_2 mapping has been proposed, by combining T_1 sensitizing sequence elements, such as IR or SR pulses, with a T_2 preparation [121–124]. Cardiac MR fingerprinting (MRF) enables joint parameter mapping by unconventionally sampling with a very high temporal resolution and highly undersampled spiral readout [125]. A combination of preparation modules is used to sensitize the magnetization in cardiac MRF. Voxel-wise maps are then obtained by matching the signal evolution to precalculated dictionaries instead of conventional curve fitting. Multitasking is a new framework for multiparameter imaging of dynamic processes, in which signal dimensions such as T_1 and T_2 contrast or physiological motion are partially sampled, and low-rank tensor reconstructions are used to compensate for missing information [126]. Despite the potential of MRF and multitasking as promising free-running tissue characterization sequences, there are still numerous challenges, including lengthy reconstruction time, sensitivity to field inhomogeneity, and other imaging confounders that warrant further investigation prior to clinical adoption.

In addition to classical relaxometry parameters like T_1, T_2, T_2^*, other cardiac MRI markers for myocardial tissue characterization are emerging. Longitudinal relaxation in the rotating frame ($T_{1\rho}$) probes the molecular environment at intermediate frequencies below the Larmor frequency and is promising for detection of myocardial fibrosis [127]. MT, a well established contrast mechanism for visualizing signals from bound pool protons in macromolecules, has been used for the assessment of myocardial fibrosis. Chemical exchange saturation transfer, based on proton exchange between free water and solute protons in metabolites like creatine, can also assess the metabolic activity and aid detection of infarcted tissue [128]. The sensitivity of these sequences to field inhomogeneity and cardiac motion remain major challenges. In addition, there is currently insufficient evidence to demonstrate the added value of acquisition of these newer contrasts compared to other established and widely available sequences for myocardial tissue characterization.

4.3. FUTURE PERSPECTIVES

Over the past decade, advances in cardiac MR have made this imaging modality an invaluable test in the management of patients with cardiovascular disease. The growth has been particularly evident in Europe, where cardiac MR is now widely used and included in several

clinical guidelines. Recent and ongoing multicenter studies are providing the necessary evidence of the clinical importance of cardiac MR. Recent technical advances in cardiac MR will further advance our field by addressing current shortcomings and obstacles of widespread adoption. Furthermore, development and validation of emerging technologies could provide new insights into cardiovascular pathology. The ongoing two-pronged approach of improving technical capabilities and clinical validation is necessary to better define appropriate use criteria of cardiac MR in daily clinical practice.

4.4. SUPPLEMENTARY MATERIALS

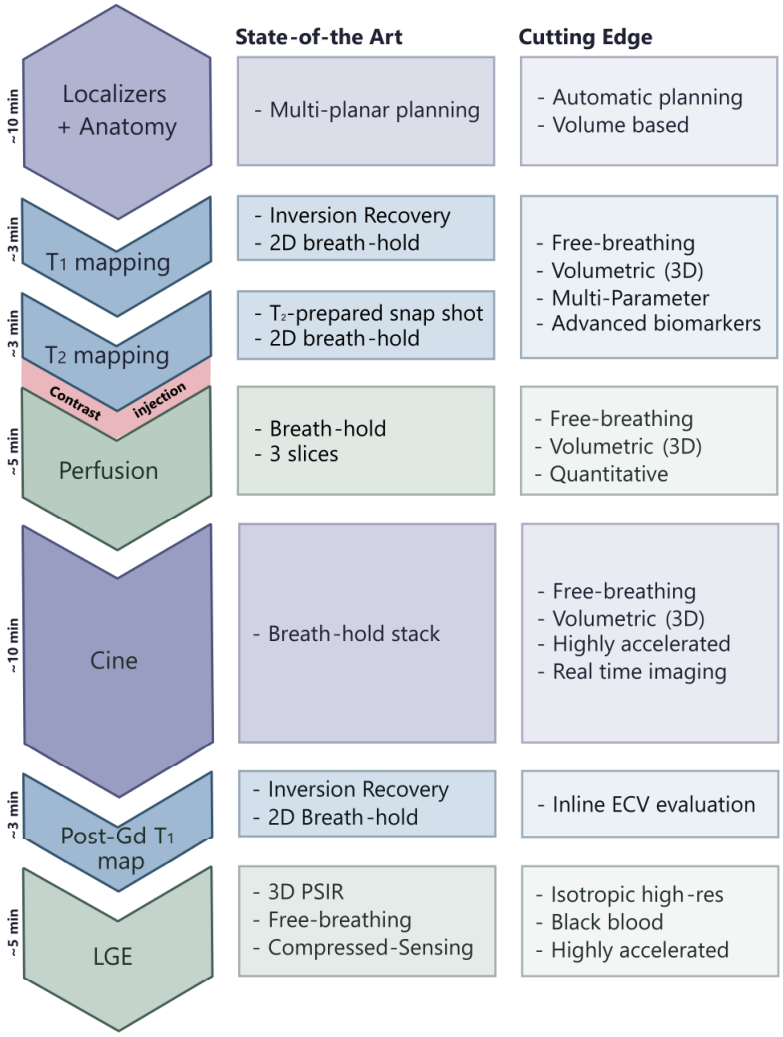

Figure S4.1.: Example imaging protocol scheme for advanced tissue characterization, presenting current state-of-the-art techniques and advanced methods.

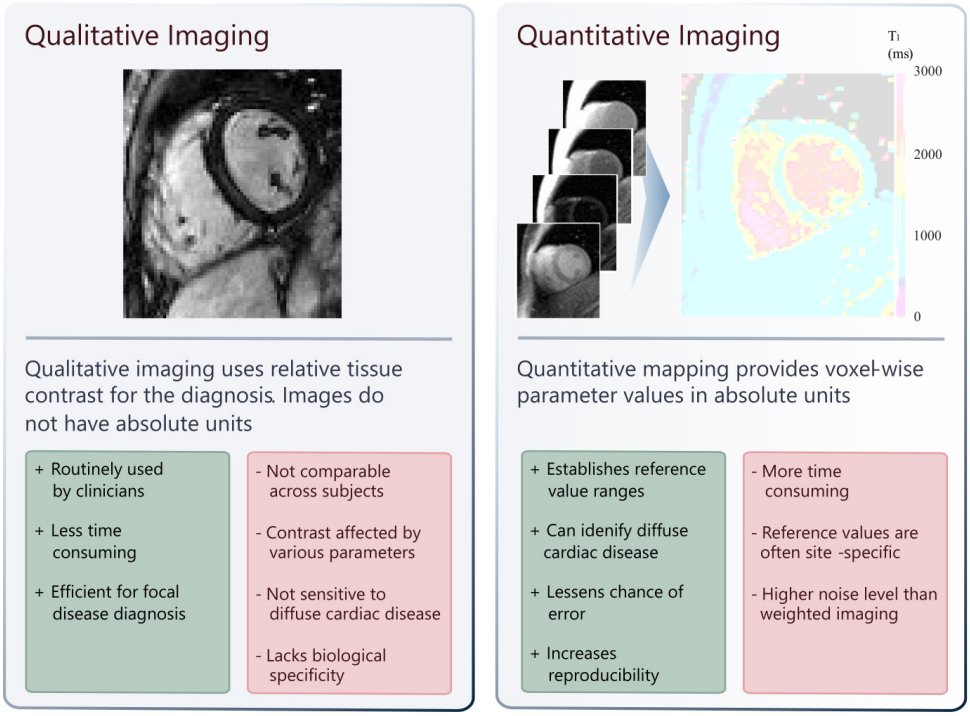

Figure S4.2.: Myocardial tissue characterization can be performed with qualitative (weighted) imaging and quantitative (mapping) techniques, with complimentary advantages. An increasing number of quantitative mapping techniques is being introduced leading to steady uptake in clinical use.

5

PREPARATION-BASED B_1^+ MAPPING IN THE HEART USING BLOCH-SIEGERT SHIFTS

This chapter is published as: Šiurytė, P., Tourais, J., Zhang, Y., Coletti, C., van de Steeg-Henzen, C., Mandija, S., Tao, Q., Henningsson, M., Weingärtner, S. (2024). Preparation-based B_1^+ mapping in the heart using Bloch–Siegert shifts. Magnetic Resonance in Medicine, 1-11. https://doi.org/10.1002/mrm.30232.

5.1. ABSTRACT

Purpose: To develop and evaluate a robust cardiac B_1^+ mapping sequence at 3T, using Bloch-Siegert shift (BSS)-based preparations.

Methods: A longitudinal magnetization preparation module was designed to encode $|B_1^+|$. After magnetization tip-down, off-resonant Fermi pulses, placed symmetrically around two refocusing pulses, induced BSS, followed by tipping back of the magnetization. Bloch simulations were used to optimize refocusing pulse parameters and to assess the mapping sensitivity. Relaxation-induced B_1^+ error was simulated for various T_1/T_2 times. The effective mapping range was determined in phantom experiments, and $|B_1^+|$ maps were compared to the conventional BSS method and sub-adiabatic hyperbolic-secant 8 (HS8) pulse-sensitized method. Cardiac B_1^+ maps were acquired in healthy subjects, and evaluated for repeatability and imaging plane intersection consistency. The technique was modified for 3D acquisition of the whole heart in a single breath-hold, and compared to 2D acquisition.

Results: Simulations indicate that the proposed preparation can be tailored to achieve high mapping sensitivity across various B_1^+ ranges, with maximum sensitivity at the upper B_1^+ range. T_1/T_2-induced bias did not exceed 5.2%. Experimentally reproduced B_1^+ sensitization closely matched simulations for $B_1^+ \geq 0.3B_{1,max}^+$ (mean difference 0.031±0.022, compared to 0.018±0.025 in the HS8-sensitized method), and showed 20-fold reduction in the standard deviation of repeated scans, compared with conventional BSS B_1^+ mapping, and an equivalent 2-fold reduction compared with HS8-sensitization. Robust cardiac B_1^+ map quality was obtained, with an average test-retest variability of 0.027±0.043 relative to normalized B_1^+ magnitude, and plane intersection bias of 0.052±0.031. 3D acquisitions showed good agreement with 2D scans (mean absolute deviation 0.055±0.061).

Conclusion: BSS-based preparations enable robust and tailorable 2D/3D cardiac B_1^+ mapping at 3T in a single breath-hold.

5.2. INTRODUCTION

Cardiac Magnetic Resonance (CMR) imaging at high magnetic fields (≥3T) is commonly used due to the promise of increased signal-to-noise ratios (SNR) compared to 1.5 T [129, 130]. However, body imaging at high magnetic fields suffers from strong inhomogeneities of the transmitted radiofrequency (RF) field B_1^+ [73, 131, 132]. The inhomogeneities arise as RF wavelengths approach the body dimensions, leading to dielectric artifacts causing inadvertent areas of low/high contrast. In cardiac imaging, flip-angle variations reach up to 50% across the area of interest [8, 133], compromising both qualitative

image reading and quantitative measurements [134, 135].

B_1^+ mapping is routinely used for inhomogeneity compensation with shimming [38] or for correction of quantitative measurements [37]. However, the application of most B_1^+ mapping approaches to the heart is complicated by cardiac and respiratory motion. The saturated double angle method (SDAM) has been previously applied in CMR [136], although with limited visual mapping quality. Bloch-Siegert shift (BSS) mapping has shown promise for motion-robust cardiac B_1^+ mapping [137, 138]. Here an off-resonant pulse is played after each excitation to accrue a $|B_1^+|$-dependent phase shift [139]. However, this requires long echo times (TE) making the acquisition sensitive to off-resonances, especially in the presence of implanted devices or other sources of susceptibility.

Preparation-based B_1^+ mapping methods, such as stimulated echo acquisition mode (STEAM) [90], or pre-saturation TurboFLASH [140] have also been explored in cardiac imaging. These offer specific absorption rate (SAR)-efficiency and are promising for fast mapping. STEAM-based dual refocusing echo acquisition mode (DREAM) has been applied to myocardial B_1^+ mapping, but the map quality is limited by the use of echo planar imaging (EPI) readouts [141]. Furthermore, sensitivity to flow hinders B_1^+ mapping in the ventricular blood pools. A pre-saturation TurboFLASH method has achieved robust whole heart mapping [142]. However, with previously proposed sinc or sub-adiabatic hyperbolic-secant (HS) pulses, the method is less sensitive at higher relative B_1^+ power, which is commonly the range of interest.

In this work, we investigate the use of BSS in longitudinal magnetization preparations for tailored $|B_1^+|$ sensitivity, combined with snap-shot imaging for robust and efficient B_1^+ mapping of the heart. The sensitivity, quantification bias, and precision of the proposed preparation-based mapping method were assessed in Bloch simulations and phantom experiments. In-vivo B_1^+ mapping is evaluated in a cohort of healthy subjects and compared to conventional BSS mapping and the sub-adiabatic pulse HS8-sensitized method. Finally, the feasibility of whole-heart, single breath-hold B_1^+ mapping is demonstrated.

5.3. METHODS

5.3.1. B_1^+ PREPARATION MODULE AND MAPPING SEQUENCE

The proposed B_1^+ mapping method uses a preparation module that sensitizes the longitudinal magnetization to a $|B_1^+|$-dependent BSS. The module consists of a tip-down/tip-up pulse pair surrounding four off-resonant pulses, placed symmetrically around two refocusing pulses (Figure 5.1). After the magnetization is tipped by the initial $90^\circ_{0^\circ}$ hard pulse (with underscore indicating the pulse phase), it accumulates $\pm\phi_{BS}$

phase during each of the four off-resonant pulses (Figure 5.1A). This results in a reduced magnetization component along the tip-back axis, depending on the cosine of the accrued phase. The B_1^+-sensitized magnetization is then tipped up with a $90°_{180°+\phi_{TB}}$ hard pulse. The tip-back phase offset ϕ_{TB} can be used to tailor the sensitivity to various B_1^+ ranges. Finally, a spoiler gradient is applied (duration 6.25 ms) to eliminate residual transverse magnetization.

For B_1^+ mapping, three images are acquired to extract the BSS-weighted image contrast in a confounder-resilient manner (Figure 5.1B):

1. $I_{4\phi}$ image with cumulative 4ϕ phase;

2. $I_{0\phi}$ equivalent image with a zero BSS is achieved by selectively flipping the off-resonance pulse frequency shift polarity (BS+ and BS-), to compensate for relaxation and magnetization transfer;

3. I_{sat} image preceded by "Water suppression Enhanced through T_1-effects" (WET) saturation pulse, to compensate for the effect of the snap-shot readout [143].

The ratio of the prepared images can be expressed as:

$$\frac{M_{4\phi}}{M_{0\phi}} = \frac{I_{4\phi} \check{} I_{sat}}{I_{0\phi} \check{} I_{sat}} = \tag{5.1}$$

$$\frac{\sin^2(90°\beta)\cos(4\kappa_{BS}(B_{1,max}^+\beta)^2) + \cos^2(90°\beta)}{\sin^2(90°\beta) + \cos^2(90°\beta)} \tag{5.2}$$

Here β describes the normalized transmit field magnitude ($B_{1,norm}^+$), $B_{1,max}^+$ is the Fermi pulse amplitude and κ_{BS} is the pulse-shape dependent scaling constant [139]. $B_{1,norm}^+$ maps are generated by β parameter voxel-wise fitting of sing a golden section search-based optimization via Matlab (Mathworks, MA, United States). Perfect refocusing was assumed during the reconstruction.

Off-resonant pulses were played at ±7 kHz offset, and a Fermi shape with a full-width-half-maximum (FWHM) of 90% ($\kappa_{BS} = 7.28 \cdot 10^8$ rad/ms). Refocusing was performed using adiabatic tanh/tan pulses placed equidistantly between the tip-down and tip-up pulses.

For cardiac $|B_1^+|$ mapping, single breath-hold, end-diastolic ECG-triggered images were acquired with a 5 s rest period between the BSS-prepared images for longitudinal magnetization recovery (Figure 5.1B).

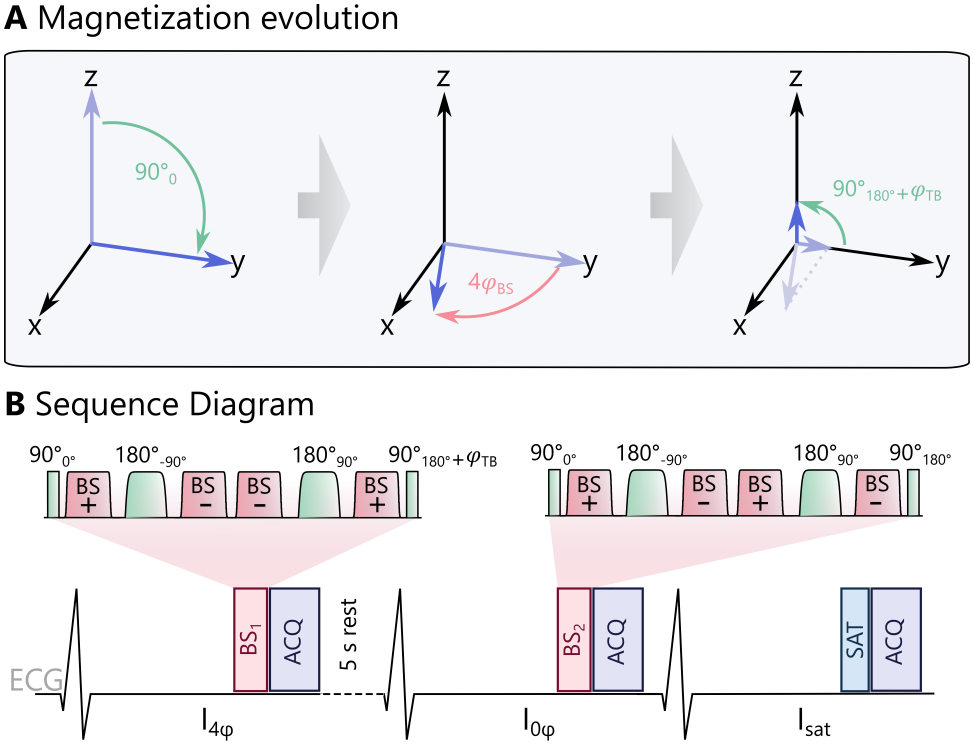

Figure 5.1.: (**A**) Schematic of the magnetization evolution during the BSS preparation during the tip-down (left), during the 4ϕ $|B_1^+|$-dependent phase shift (middle), and the tip-up with reduced transverse magnetization component along the tip-back phase ϕ_{TB} (right). (**B**) Bloch-Siegert shift (BSS)-based preparation modules with effective BSS phase shift of 4ϕ (BS_1) and effective phase shift of 0 (BS_2). Both preparations contain tipping and refocusing pulses (green) and off-resonant Fermi pulses (pink), with variable polarity (plus/minus) of the frequency offset. Below is the sequence diagram of three baseline images ($I_{4\phi}$,$I_{0\phi}$,I_{sat}) required for confounder-resilient B_1^+ map reconstruction. End-diastole imaging (ACQ) is preceded by the preparation module or saturation preparation (SAT). A rest period is played for longitudinal magnetization recovery before the $I_{0\phi}$ image, and all images are acquired in a single breath hold.

5.3.2. SIMULATIONS

Simulations were performed to optimize the Fermi pulse duration d_{BS} for maximum mapping sensitivity and bijective B_1^+ encoding. For a tip-back phase of ϕ_{TB}=0, BSS of 180° was specified at the maximum expected $|B_1^+|$ value. Based on previous literature, 110% of the nominal

RF amplitude was chosen for 3T [8]. Refocusing pulse duration d_{REF} and shape parameters ξ and f_{max} were optimized to yield high B_0/B_1^+ resilience at $B_{1,norm}^+ \in$[0.5,1.1] and off-resonance $\Delta\omega \in$[-200,200] Hz using Bloch simulations of the preparation with $\phi_{BS} = 0$. $B_{1,max}^+$ of 13.5 μT was used for RF pulses to match the scanner hardware limitations.

The B_1^+ sensitivity of the proposed preparation was assessed using Bloch simulations for $B_{1,norm}^+ \in$[0,1.1], and compared to sub-adiabatic HS8 preparation, as previously used in B_1^+ mapping [142]. The B_1^+ sensitivity was obtained as the derivative of the post-preparation longitudinal magnetization with respect to $B_{1,norm}^+$. HS8 pulses were simulated with a time-bandwidth product of 15 and a truncating factor of 5.3 [142, 144, 145]. For the proposed preparation, 45 ms sequence duration, $d_{BS} = 4.6$ ms and $\phi_{TB} = 0$ parameters were used.

To assess the impact of residual relaxation effects, the B_1^+ error was estimated for various T_1 and T_2 combinations: $T_1 \in \{250; 1500\}$ ms and $T_2 \in \{50, 100, 150\}$ ms and $\{50, 150, 250\}$ ms for the two T_1 values, respectively. The post-preparation magnetization was simulated using Bloch simulations including or excluding T_1 and T_2 relaxation effects. The error was estimated as the relative difference in the obtained $B_{1,norm}^+$ values. The preparation parameters were simulated as listed above.

5.3.3. IMAGING

Experiments were performed on a 3T Philips Ingenia scanner (Amsterdam, the Netherlands) without 1st level SAR mode. For 2D mapping, the proposed method used 45-50 ms preparation (unless stated otherwise), followed by a snap-shot balanced steady-state free precession (bSSFP) readout. Imaging was performed with flip angle = 40°, bandwidth BW = 1447 Hz/px, slice thickness s = 10 mm and matrix size = 120×120. In the preparation, d_{REF} = 4 ms refocusing pulses with $\xi = 8$ and $f_{max} = 5400$ Hz were used. Fermi pulse duration was $d_{BS} = 4.6$ ms unless stated otherwise.

5.3.4. PHANTOM EXPERIMENTS

To demonstrate the mapping sensitivity tailoring to different $B_{1,norm}^+$ ranges, three different BSS-preparations were designed. The tip-down/up angle, the Fermi pulse duration d_{BS} and the tip-back phase ϕ_{TB} of the BSS-prepared image with 4ϕ shift were chosen, based on simulations, to achieve peak sensitivity at $B_{1,P,norm}^+ = 0.7/0.8/0.9$, respectively. The preparations were performed with a duration of 65 ms and Fermi pulse amplitude of $B_{1,max}$ = 13.5 μT. Phantom scans were performed in the T1MES phantom [146] with FOV = 300×300 mm^2, s

= 10 mm, TR/TE = 2.5/1.2 ms, and seven repetitions. To simulate B_1^+ inhomogeneities, the power of the RF pulses in the preparation was scaled between $B^+_{1,P,norm}$-0.25 and $B^+_{1,P,norm}$+0.05 in steps of 0.05. The standard deviation of the reconstructed $B^+_{1,norm}$ values, mapped in a manually drawn region of interest (ROI) of the central phantom vial (T_1/T_2 = 1499/49 ms), was calculated for each preparation and scaling. The inverse of the standard deviation values was used as a metric for noise sensitivity, and compared with simulations.

B_1^+ mapping linearity was assessed for the optimized preparation with $\phi_{TB} = 0$, and compared to sub-adiabatic HS8-sensitization. For the proposed BSS-prepared method, the same imaging parameters were used, as listed above, with the exception of flip angle (60°). The HS8 pulse mapping method was performed using the same pulse parameters as in simulations and acquired with a spoiled gradient echo (GRE) readout (flip angle = 7°, TR/TE = 2.7/1.2 ms, BW = 868 Hz/px, identical FOV/matrix, centric k-space ordering). A 5 s rest period was used for the magnetization recovery between the non-prepared and HS8-sensitized images. For both mapping methods, B_1^+ inhomogeneities were simulated with scaling all RF between 5% and 100% in steps of 5%, acquiring two repetitions for each scale. B_1^+ inhomogeneities were simulated with scaling all RF between 5% and 100% in steps of 5%, acquiring two repetitions for each scale. The scale was normalized to the highest sensitivity point for both mapping methods, as determined from the simulations. In a manually drawn ROI in the central vial, the mean and standard deviation of the post-preparation signal ratio were compared to the simulations. The phantom data were compared to the simulations using linear regression and Bland-Altman analysis to determine an effective B_1^+ mapping range.

Noise resilience of the proposed method was compared with a conventional BSS mapping technique and the HS8-prepared technique in a torso-sized, cylindrical systems phantom. Images were acquired with the prepared BSS sequence (FOV = 450×450 mm^2, s = 10 mm, TR/TE = 1.99/0.94 ms), the conventional spoiled GRE BSS sequence (flip angle = 10°, TR/TE = 18/0.99 ms, BW = 1653 Hz/px, identical FOV/matrix) and the HS8-sensitized sequence (identical imaging parameters as above, TR/TE = 2.6/1.15 ms with matched FOV/matrix). For the conventional BSS sequence, 8 ms Fermi pulses were placed after each excitation , with 90% FWHM, ±7 kHz off-resonance, and $B^+_{1,max}$ =6.8 μT to keep within SAR limits [138]. Ten image repetitions were acquired for the three methods to assess the mean and standard deviation of the B_1^+ map within manually drawn ROIs.

5.3.5. IN-VIVO EXPERIMENTS

The study was ethically approved by the competent authority (METC: NL73381.078.20) and written informed consent was obtained from each subject prior to examination.

$|B_1^+|$ maps were acquired in four-chamber (4CH), two-chamber (2CH), and basal/mid/apical short axis orientations (SAXb, SAXm, SAXa) with two repetitions (FOV = 300×300 mm^2, s = 10 mm). 11 subject data (7 female, 25±2 y.o.) were acquired for the proposed technique comparison with the conventional BSS mapping methods, and 6 subject data (female, 24±3 y.o.) for the HS8-sensitization comparison. The conventional BSS technique used a segmented acquisition (TR/TE = 18/1.22-1.33 ms, BW = 1653 Hz/px) with 7-13 k-space lines per heartbeat triggered to the end-diastole in a single breath-hold. Sequential acquisition of all positive off-resonance shift lines, followed by all negative ones was performed. Fermi pulse parameters were equivalent to phantom imaging, with 5.9-7.6 μT amplitude. The HS8-prepared technique used imaging parameters equivalent to the phantom experiments (TR/TE = 2.7-2.8/1.2-1.3 ms with matched FOV/matrix) and a single-shot readout, with end-diastole triggered breath-hold acquisition. The conventional BSS, HS8-prepared and the proposed sequences resulted in 11-16, 7-8 and 8-9 s breath-holds, respectively. For all techniques, baseline image registration was performed in a group-wise manner using principal component analysis [147]. Based on a magnitude image ($I_{0\phi}$ for the proposed technique and HS8-prepared image for the HS8-sensitization), the real/imaginary parts of the baseline images were registered to this template.

Test-retest repeatability was measured as the absolute deviation between two sequence repetitions over a manually drawn ROI covering the whole heart. Additionally, the intersection lines between 4CH, 2CH and SAXm planes were calculated and inspected for the proposed technique in 12 subjects (8 female, 25±2 y.o.).

Finally, the feasibility of a single 20 s breath-hold $|B_1^+|$ 3D mapping of the whole heart with the prepared sequence was demonstrated in one subject (female, 22 y.o.). The proposed sequence was modified to replace the rest period with a saturation pulse at the beginning of each RR cycle for magnetization reset. A segmented bSSFP acquisition with 50 k-space lines per heartbeat was used, with flip angle = 30°, TR/TE=2.5/1.2 ms, BW=1447 Hz/px, FOV = 220×220×120 mm^3 and matrix size = 72×44×12 in SAX view, SENSE = 1.5 in slice and phase-encode directions. The preparation duration was 45 ms,d_{BS} =3.6 ms and $B_{1,max}^+$ =11.5 μT. 3D maps were reformatted for visual comparison to match the 2D imaging slices. Manually drawn ROIs were used for quantitative evaluation.

5.4. RESULTS

5.4.1. SIMULATIONS

Off-resonant pulse duration optimization for a target maximum $B^+_{1,norm}$ = 1.1 yielded an upper bound of d_{BS} =4.6 ms at ϕ_{TB} = 0. Optimal refocusing was achieved with $\xi = 8$ and $f_{max} = 5400$ Hz for the d_{REF} = 4 ms tanh/tan pulses (Figure S5.1). These parameters achieved an average preparation efficiency of 92.38% over the optimization range.

The comparison of the numerical noise sensitivity between HS8 and BSS-based preparations is shown in Figure 5.2A. HS8 pulse achieves better sensitivity in low $B^+_{1,norm}$ region, while the proposed method shows strongly improved sensitivity for the upper range of B^+_1 scaling ($B^+_{1,norm} > 0.64$).

Mean absolute reconstruction bias due to relaxation effects at T_1 = 250 ms was simulated as 0.033±0.016/0.017±0.008/0.013±0.006 for T_2 = 50/100/150 ms, respectively (Figure 5.2B). The biggest bias is observed for B^+_1-scaling ≈0.5, where the bias reaches up to 5.2%. This is reduced for T_1 = 1500 ms, yielding 0.028±0.016/0.009±0.005/0.005±0.003 for T_2 = 50/150/250 ms.

5.4.2. PHANTOM EXPERIMENTS

The tailored preparations with varying peak B^+_1 mapping sensitivity were achieved by simulating the following parameters: d_{BS} = 10/9/8 ms, $\phi_{TB} = -40°/-70°/-90°$, and tip angle of 110°/100°/90°. The simulated/measured post-preparation signals $M_{4\phi}/M_{0\phi}$ are shown in Figure 5.2C, top plot. Experimental data indicate good agreement with simulations (mean difference of 0.05±0.04) for all tailored preparations. As per the design, the highest simulated sensitivity was at $B^+_{1,norm}$ = 0.7/0.8/0.9, respectively (Figure 5.2C, middle plot). The mapping sensitivity obtained various RF scaling confirms the shifting maximum B^+_1 mapping sensitivity peak across the three preparations (Figure 5.2C, bottom plot). With increasing d_{BS} and ϕ_{TB}, better sensitivity is achieved at lower B^+_1 scales.

For both the HS8-sensitized and the proposed technique, phantom experiments show good linearity (Figure 5.3A). The proposed technique shows good linearity and small deviation between the reconstructed $B^+_{1,norm}$ and the input RF scaling, for $B^+_{1,norm} \geq 0.3$ (y=1.07x-0.06, mean absolute difference = 0.031±0.022, Figure 5.3A), when using the default preparation (ϕ_{TB}=0). For $B^+_{1,norm} < 0.3$, mapping accuracy and precision strongly decrease, which coincides with poor refocusing efficiency (Figure S1). For the HS8-sensitized method, good linearity is maintained even for very low $B^+_{1,norm}$ scales (with y = 0.92x+0.04 for $B^+_{1,norm} \geq 0.3$, mean absolute difference 0.018±0.025). However, an increasing underestimation is observed for high $B^+_{1,norm}$ scales, reaching

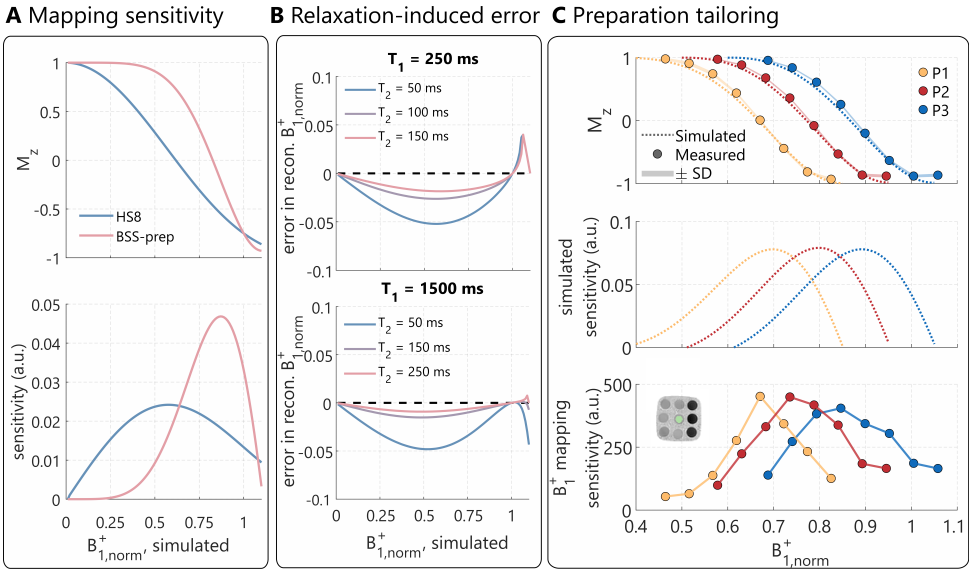

Figure 5.2.: (**A**) Bloch-simulations of $|B_1^+|$ sensitizing preparations based on Bloch-Siegert shift (BSS), with $d_{BS} = 4.6$ ms Fermi pulses, 13.5 μT amplitude, and tip-back phase $\phi_{TB} = 0$ (red) and sub-adiabatic hyperbolic-secant 8 (blue). The top panel shows the post-preparation magnetization as a function of the $|B_1^+|$ strength and the bottom panel shows the sensitivity, defined as the derivative of the post-preparation magnetization with respect to $B^+_{1,norm}$. Increased sensitivity is observed with BSS-based preparations for higher $|B_1^+|$ magnitudes ($|B_1^+| > 0.64$). (**B**) B_1^+ map reconstruction bias due to relaxation effects for various T_2 times in the presence of a short T_1 (top) and long T_1 (bottom). Small underestimation of less than 0.05 is observed, with the largest deviation occurring for $B^+_{1,norm} > 1.0$ or $B^+_{1,norm} \approx 0.5$. (**C**) B_1^+ mapping performance of three different preparations (P1, P2, P3). The preparation parameters were tailored for different peak sensitivities, with Fermi pulse duration $d_{BS} = 10/9/8$ ms, tip-back phase $\phi_{TB} = -40°/-70°/-90°$, and tip angle of 110°/100°/90°, respectively. Post-preparation magnetization $M_{4\phi}/M_{0\phi}$ (top plot) shows good agreement between simulated data (dashed lines) and phantom (solid line). Mapping sensitivity in simulations (middle plot) and experiments (bottom panel) show comparable trends with a shift in peak sensitivity to higher B_1^+ values from P1 to P3. The phantom ROI in the central vial is indicated in the bottom panel.

up to 0.08.

In the cylindrical phantom, preparation-based B_1^+ maps appear visually more homogeneous than conventional BSS (Figure 5.3B), which displays off-resonance artifacts at the edge of the phantom. Meanwhile, the

HS8-sensitized map displays minor fold-over artifacts, and BSS-prepared map shows no visually apparent artifacts. The mean SD with the proposed method (0.002±0.001) was greatly reduced when compared to the conventional BSS mapping (0.048±0.007), and slightly improved compared to the HS8-prepared method (0.004±0.001).

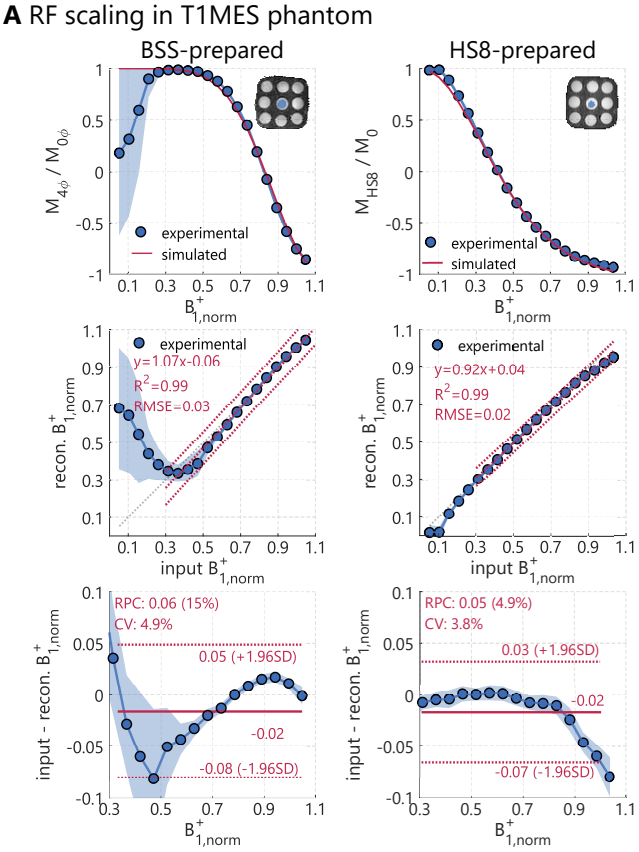

B $|B_1^+|$ & SD maps

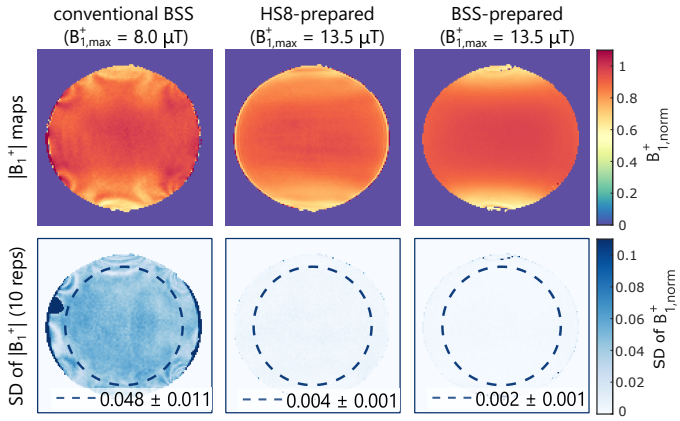

Figure 5.3.: (Continued on the following page.)

Figure 5.3.: (**A**) Overlay of simulation and phantom results of the $|B_1^+|$ dependent signal using the proposed BSS-preparation (left) with $d_{BS} = 4.6$ ms Fermi pulse duration, $B_{1,max}^+ = 13.5$ μT and $\phi_{TB} = 0$, and the HS8-sensitization (right). The top plots illustrate post-preparation longitudinal magnetization ratio $M_{4\phi}/M_{0\phi}$ and M_{HS8}/M_0, while the middle plots show RF scaling and reconstructed B_1^+ linearity (left and) and bottom - the corresponding Bland-Altman analysis. (**B**) B_1^+ maps in the cylindrical phantom obtained using the conventional BSS mapping sequence (top left), the HS8-sensitization (top middle) and the proposed BSS-prepared method (top right). The corresponding SD maps from ten measurements are illustrated in the bottom row, with mean values over the ROI (dashed line) of 0.048±0.007 for the conventional BSS, 0.046±0.001 for the HS8-sensitization, and 0.002±0.001 for the proposed method.

5.4.3. IN-VIVO EXPERIMENTS

Images in subjects show visually improved B_1^+ mapping quality and uniformity in the proposed preparation-based mapping, particularly in comparison to the conventional BSS method. While both preparation-based techniques achieve good mapping quality, the HS8-sensitization results in visually apparent tissue contrast. The characteristic trend of B_1^+ reduction towards the right ventricle and the apex is visible visible. The absolute test-retest difference was greatly reduced with the proposed technique when compared to the conventional BSS: from 0.135±0.113/ 0.175±0.135/ 0.134±0.109/ 0.132±0.110/ 0.147±0.119 across all subjects for 4CH/2CH/SAXb/SAXm/SAXa orientations (0.140±0.117 across all orientations), to 0.029±0.041/ 0.033±0.061/ 0.024±0.036/ 0.023±0.033/ 0.027±0.045 (0.027±0.043 across all orientations).Similar to phantom experiments, a slight improvement was achieved when compared to HS8-sensitized method: from 0.038±0.044/ 0.035±0.040/ 0.025±0.030/ 0.044±0.063/ 0.028±0.043 (0.035±0.047 across all orientations) to 0.024±0.030/ 0.016±0.017/ 0.018±0.022/ 0.019±0.026/ 0.022±0.043 (0.020±0.028 across all orientations). The SAR burden of the conventional BSS sequence was 2.6-2.7 W/Kg. The proposed BSS-prepared method yields a reduced SAR burden of 1.6-1.7 W/kg in the proposed sequence, despite the use of high flip angles in the bSSFP readout. The HS8-prepared sequence with spGRE readout results in the lowest SAR burden (0.2 W/kg).

Figure 5.4C illustrates 4CH/2CH/SAXm intersection of the B_1^+ maps for a representative subject. Inspection reveals good overall agreement

between different imaging planes, with a mean absolute difference of 0.050±0.039/0.054±0.028/0.050±0.027 in 4CH-2CH, 2CH-SAXm, and 4CH-SAXm comparisons, respectively, across all subjects (0.052±0.031 across all orientations).

The 3D acquisition shows good visual mapping quality (Figure 5.5A). A comparison between 2D maps and reformatted 3D imaging shows good agreement, with an absolute mean difference of 0.075±0.065/0.168±0.254/0.057±0.135 for 4CH/2CH/SAXm views (0.055±0.061 across all orientations), across the ROIs (Figure 5.5B).

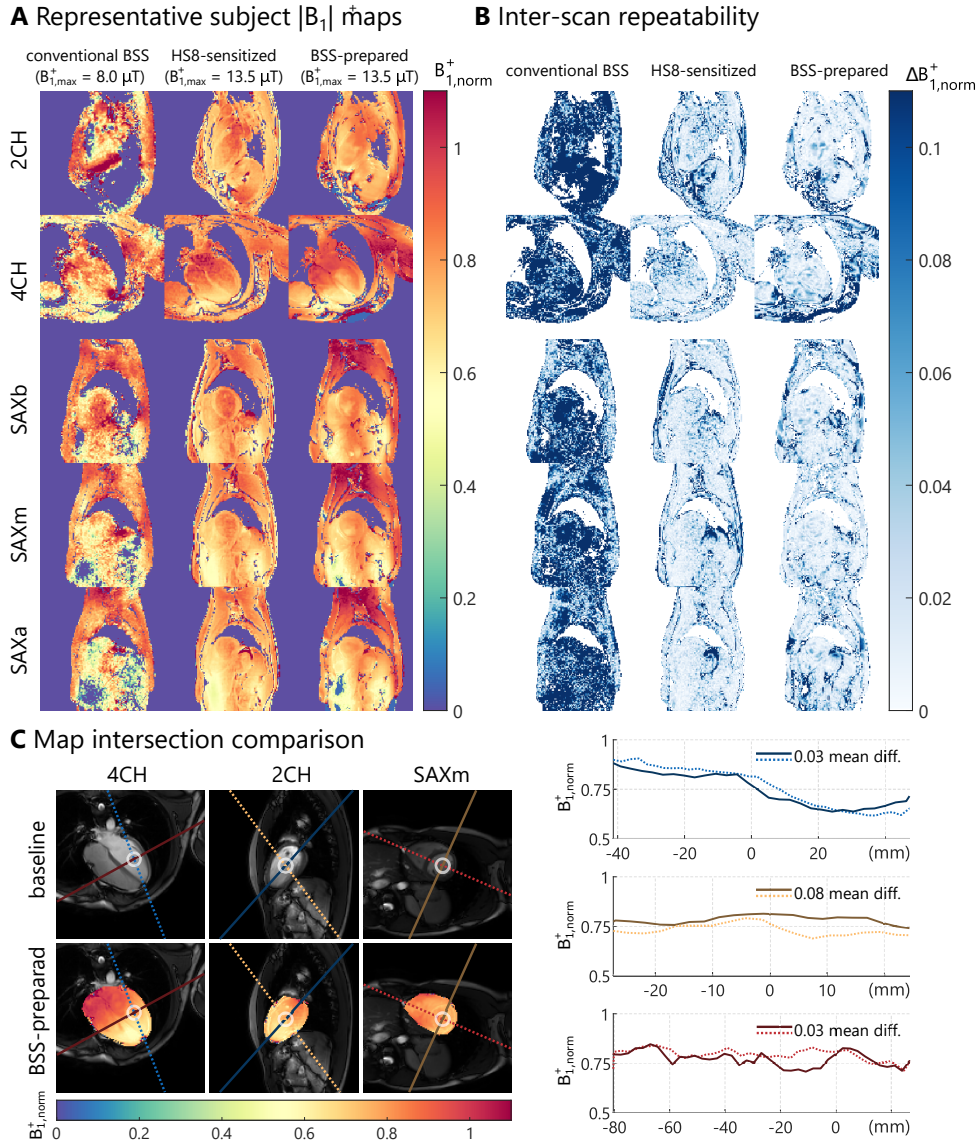

Figure 5.4.: (Continued on the following page.)

Figure 5.4.: (**A**) B_1^+ maps of a representative subject for the conventional phase-based Bloch-Siegert shift (BSS) sequence (left column), the HS8-sensitized sequence (middle column) and the proposed BSS-prepared mapping sequence(right column), for five different orientations. (**B**) Corresponding maps of the absolute test-retest deviation. (**C**) B_1^+ map intersection analysis example for another subject. Imaging views are shown on the left side with baseline image and intersection line illustration (top) in blue (4CH-2CH), yellow (2CH-SAXm), and red (4CH-SAXm) lines. The bottom plots illustrate the BSS-preparation-based B_1^+ maps overlayed on the manually drawn heart ROIs. B_1^+ map intersection lines are plotted on the right side for a single subject. Across all subjects, the resulting mean absolute deviation values were 0.063±0.052, 0.070±0.030 and 0.046±0.022 for 4CH-2CH, 2CH-SAXm and 4CH-SAXm intersections, respectively.

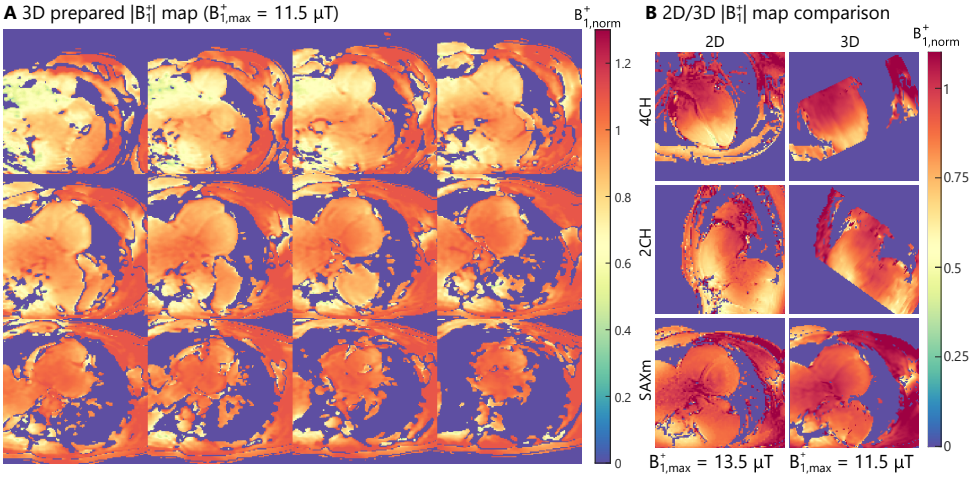

Figure 5.5.: (**A**) Reconstructed 3D B_1^+ maps in the short axis view, obtained using the modified BSS-prepared sequence. (**B**) A side-by-side comparison of 2D and a reformatted 3D B_1^+ map reconstructions in 4CH (top), 2CH (middle), and SAXm (bottom) orientations, with 2D maps cropped to reduced FOV to match the 3D acquisition. The mean absolute difference between the reformatted 2D and 3D maps was measured as 0.075±0.065/0.168±0.254/0.057±0.135 for 4CH/2CH/SAXm orientations.

5.5. DISCUSSION

In this study, a cardiac B_1^+ mapping sequence based on Bloch-Siegert shift preparations was introduced and investigated at 3T. The proposed preparation allowed for tailorable B_1^+ mapping sensitivity, and demonstrated strongly improved mapping quality compared with phase-based BSS mapping, and less relaxation-induced reconstruction bias compared with sub-adiabatic HS8 pulse-based preparation. Phantom results show good mapping accuracy down to 30% of the maximum B_1^+. In-vivo data indicate robust and efficient mapping of the B_1^+ transmit field magnitude at 3T in 2D and 3D measurements.

B_1^+ mapping with the proposed preparation parameters is particularly sensitive to the upper range of B_1^+ values. This offers better sensitivity in the inhomogeneity range of interest at 3T. In contrast, previously used preparations with sub-adiabatic HS8 pulses showed the highest sensitivity to low B_1^+, which may be less desirable [142]. In the proposed BSS-preparation, the tip-back phase ϕ_{TB} and Fermi pulse amplitude can be tailored to increase mapping sensitivity at lower B_1^+ areas. This may be useful for ultra-high field imaging, where the inhomogeneity range is expected to increase.

The main sensitization mechanism in the proposed preparation is based on the phase shift of the transverse magnetization. However, the use of hard pulses for tipping introduces sensitivity to B_1^+ inhomogeneities. This results in a mixed contrast, introducing a square cosine component in Equation (5.2). This factor can be avoided by implementing more robust tipping, such as adiabatic B_1-insensitive rotation (BIR) pulses, albeit at the cost of increased sequence SAR. Imperfect tipping introduces a slight dependence on the relaxation effects. Due to the compensation intrinsic to the imaging scheme, this residual effect was neglected in B_1^+ reconstruction. Numerical simulations have shown that the T_1/T_2 relaxation-induced error does not exceed 5.2% under realistic conditions. However, evaluation of various tip down/up pulses, for a trade-off between SAR, a simplified reconstruction, and increased resilience against residual relaxation remains the subject of future work.

Compared with conventional BSS-based B_1^+ mapping, the proposed sequence employs a lower number of off-resonant pulses. This allowed for a shorter TE, increasing off-resonance artifact resilience, as evident from the systems phantom acquisitions. Additionally, it reduces the SAR burden, and, importantly, decouples the B_1^+ sensitization from the readout. As a result, the proposed approach is suitable for increased spatial resolution or coverage. While these benefits are also offered by lower-SAR HS8-sensitization, the lack of $T_1\rho$ relaxation compensation during the sub-adiabatic pulse results in a significant tissue contrast. The spoiled GRE readout, used in HS8-sensitization, could be considered in the proposed sequence to enable lower SAR.

To enable whole heart coverage with 3D imaging in a single breath-hold, the proposed mapping sequence was modified to replace the rest period with a saturation pulse at the beginning of each RR cycle. The visual map quality of the acquired 3D maps proved to be largely satisfactory, indicating sufficient noise resilience. However, the rest periods enable higher SNR due to more robust imaging readouts with lower parallel imaging factors, as evident by the direct 2D-3D comparison. In addition, imperfect saturation in the presence of low B_1^+ may compromise the mapping accuracy. Thus, the use of saturation or rest periods presents a viable trade-off between spatial coverage, scan time efficiency, and noise resilience.

The proposed B_1^+ mapping method and this study have several limitations. Firstly, hard tip-down/tip-up pulses are compromised in the presence of strong B_0 inhomogeneities, leading to a bias in B_1^+ reconstruction. The quantification of this bias, as well as a search for alternative and more robust tipping pulses warrants future investigation. Similarly, strong B_1^+ inhomogeneities lead to incomplete refocusing and saturation, limiting the effective B_1^+ mapping range. This is particularly relevant for ultra-high magnetic field applications (7 T and above), where further sequence optimization may be required for application to the increased range of B_1^+ inhomogeneities. Finally, only a small dataset of healthy subjects was presented in this work. To further establish clinical robustness and mapping reproducibility, investigation in a larger cohort of clinical patients is warranted.

Different applications of B_1^+ mapping can have divergent requirements on the B_1^+ map resolution, coverage, and noise resilience. While multi-transmit coil shimming can be performed at relatively low resolution and SNR, quantitative map corrections require higher SNR to avoid compromising the quantification precision. Emerging applications such as cardiac Electrical Properties Tomography (EPT) [10, 148] require even higher noise resilience to cater to spatial derivatives that are highly susceptible to noise. In the proposed technique, tailored preparations and acquisition parameters enable different trade-offs between noise resilience, bias, and coverage. Further investigation in the context of specific B_1^+ mapping applications is warranted to further optimize the B_1^+ map quality.

5.6. CONCLUSIONS

In this study, a BSS preparation-based B_1^+ mapping sequence was investigated for cardiac application. The preparations allow for customization of the B_1^+ mapping sensitivity, with particularly good sensitivity at high B_1^+ values. Excellent map quality was demonstrated in phantom and in-vivo experiments at 3T across the inhomogeneity range, with robust mapping extension to 3D imaging of the whole heart.

When compared to phase-based BSS imaging, the proposed sequence achieved greatly reduced noise and visually improved mapping quality. Thus, the proposed method is a promising candidate for robust B_1^+ mapping for various applications at high fields.

5.7. SUPPLEMENTARY MATERIALS

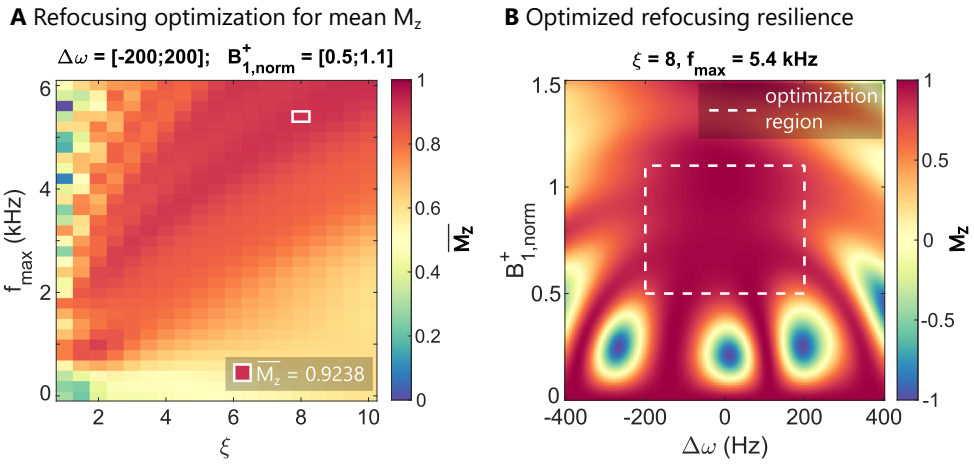

Figure S5.1.: The results of the refocusing pulse (duration d_{REF} = 5 ms) parameter optimization for high B_0/B_1^+ resilience at $B_{1,norm}^+ \in$[0.5,1.1] and off-resonance $\Delta\omega \in$[-200,200] Hz using Bloch simulations of the preparation with $\phi_{BS} = 0$. (**A**) Mean post-preparation magnetization M_z plotted for a range of tanh/tan pulse parameters ξ and f_{max}. (**B**) The optimal refocusing yields ξ = 8 and f_{max} = 5.4 kHz with 0.9238 mean post-preparation magnetization over the optimization region (dashed).

6

COMPLEX B_1^+ FIELD-BASED CONDUCTIVITY MAPPING IN THE HUMAN MYOCARDIUM AT 3T

This chapter is in proceedings: Šiurytė, P., Meerbothe, T., Zhang, Yi, Henningsson, M., Tourais, J., van de Steeg-Henzen, C., Tao, Q., Weingärtner, S., Mandija, S. (2024). Complex B_1^+ field-based conductivity mapping in the human myocardium at 3T. Proc. Intl. Soc. Mag. Reson. Med. 30. ISMRM. Singapore, 2024

6.1. SYNOPSIS

While electrical property tomography is gaining popularity, cardiac applications are limited due to inadequate cardiac B_1^+ mapping. Thus, conductivity mapping in the heart using complex B_1^+ maps is yet unexplored. To measure myocardial conductivity from the complex B_1^+ distribution in the heart at 3T, a novel $|B_1^+|$ mapping method was adapted for free-breathing B1+ maps, followed by conductivity reconstruction via 1D polynomial fitting in saline phantoms and four healthy subjects. Phantom results show excellent correlation with expected values (R^2=0.95). In-vivo, conductivity is largely homogeneous with 0.69±0.13 S/m average in-plane conductivity across all subjects, in line with the literature.

6.2. IMPACT

Electrical properties are a valuable biomarker, however, the translation to cardiac imaging remains limited. In this work, complex B_1^+ field-based conductivity is reported in the human myocardium at 3T, using a novel Bloch-Siegert shift-prepared cardiac B_1^+ mapping technique.

6.3. INTRODUCTION

While electrical property tomography (EPT) has gained attention in neuro and breast imaging, its translation to the heart is greatly limited [41]. High inherent sensitivity to residual motion and noise of the EPT reconstruction render poor B_1^+ mapping quality a major limitation. Previous efforts to map conductivity in the heart have relied on transceive phase maps, albeit requiring limiting assumption of constant B_1^+ magnitude [10]. In this work, we aim to reconstruct myocardial conductivity by adapting a recently proposed free-breathing B_1^+ mapping technique to obtain complex B_1^+ magnitude and phase maps.

6.4. METHODS

B_1^+ field magnitude and phase maps were obtained using a novel Bloch-Siegert (BS) shift-prepared cardiac B_1^+ mapping technique [149]. The sequence acquires three baseline images for the magnitude maps (Figure 6.1A-B): one with BS preparation inducing $4\phi_{BS}$ phase shift (I_{BS1}); one with equivalent preparation leading to zero phase shift (I_{BS2}), for magnetization transfer effect compensation; and a saturation-prepared image for capturing image readout (I_{SAT}). To increase the SNR in magnitude and phase B_1^+ maps, n_{BS} repetitions were obtained for I_{BS1}/P_{BS1} and I_{BS2}/P_{BS2}. Finally, to obtain additional phase data, n_P

extra non-prepared images were acquired. The B_1 transceive phase was reconstructed as the average of P_{BS1} and P_P phase images. B_1^+ phase was assumed to be equal to half of the measured transceive phase [150] (Figure 6.1C).

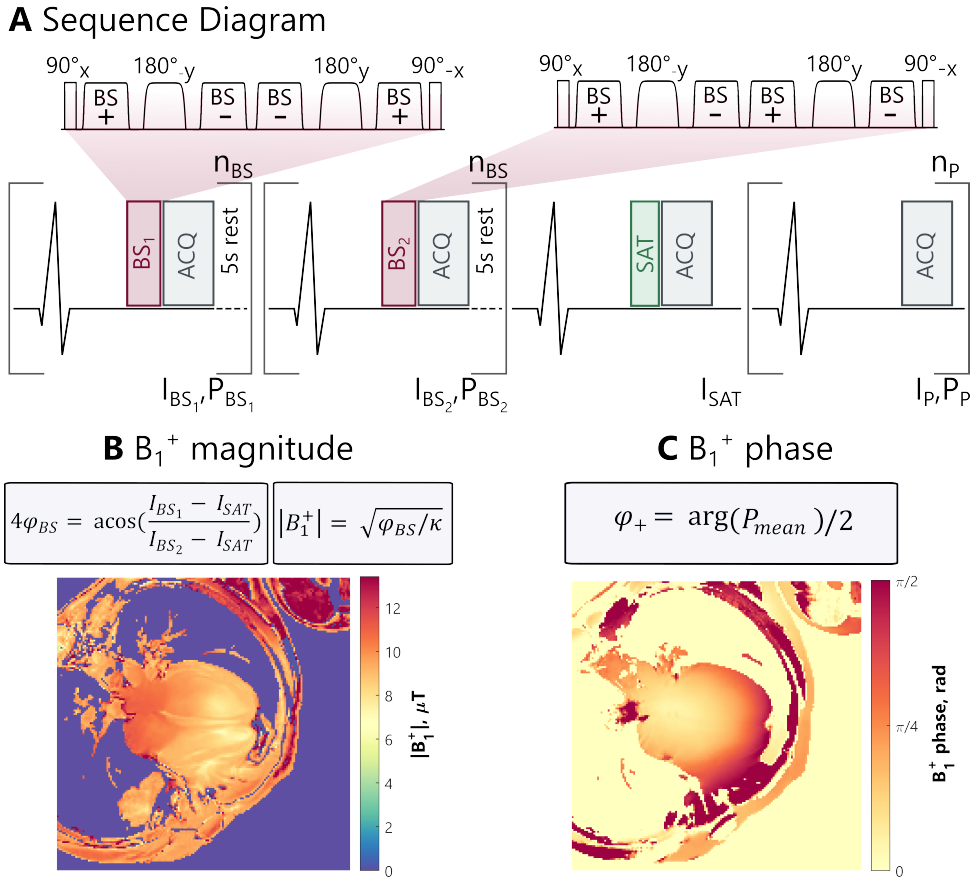

Figure 6.1.: (**A**) B_1^+ mapping sequence diagram, illustrating the preparation block RF pulses (top) with interleaved 90° tip down/up and 180° tanh/tan refocusing pulses, and Fermi pulses (BS). The sequence consists of $2n_{BS}$ prepared images (I_{BS1}, I_{BS2}), a saturation-prepared image (I_{SAT}) and n_P extra images for the transceive phase (P_P). Reconstruction model of $|B_1^+|$ magnitude (**B**) and phase ϕ^+ (**C**), using transceive phase assumption along with a representative map (four-chamber view). Here, P_{mean} denotes the mean phase image over P_{BS1} and P_P.

All imaging was performed at 3T (Ingenia, Philips). The B_1^+ maps were acquired in a custom-made phantom (coronal and transverse plane),

with 9 vials containing different saline solutions. In-vivo data were acquired in the four-chamber view for 4 healthy subjects (3 male, age 29±3). B_1^+ mapping was performed with ECG-triggering (end-diastole) and during free-breathing using a pencil beam diaphragmatic navigator. Single-shot bSSFP readout with 40° flip angle was used (TR/TE = 2.4/1.2 ms, 1.9×1.9×10/300×300×10 mm^3 resolution/FOV). The BS preparation block comprised a Fermi pulse with 4.5 ms duration and 7 kHz off-resonance. n_{BS}=20/n_{BS}=19 baseline preparations were used in phantom/in-vivo, with n_P=9 additional images. Rest periods of 5s were used after each BS-prepared image for magnetization recovery resulting in a total scan time of 4 minutes (assuming 100% navigator efficiency). Groupwise registration was applied to the real and imaginary part of the acquired images to minimize residual motion [147].

Conductivity (σ) was reconstructed using a 1D polynomial fitting approach [151] on the complex-valued B_1^+ data (Figure 6.2). For the phantom, 1D reconstructions were done in all three directions and subsequently summed. In-vivo data region of interest (ROI) was manually drawn in the septum, excluding voxels affected by partial volume effects. This was followed by polynomial 1D conductivity fitting along the longest direction of the mask, multiplied by 2 for in-plane conductivity. Equal contributions from the two in-plane directions were assumed to prevent noisy contributions from the short-axis direction.

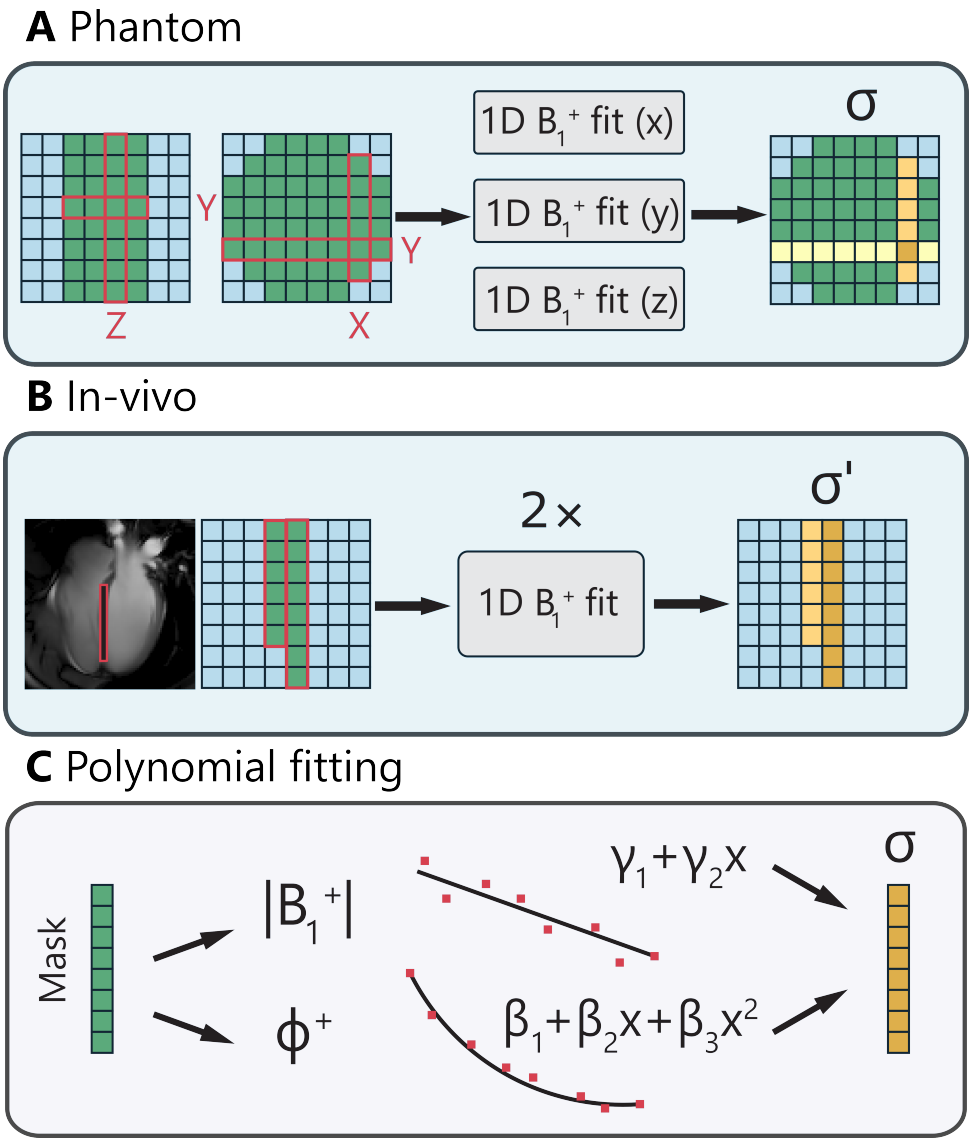

Figure 6.2.: Reconstruction schematic for (**A**) phantom conductivity σ (3×1D), and (**B**) in-vivo (2×1D) conductivity σ'. Phantom values in ROIs are reconstructed as 1D fit summed across all three directions and the mean along the Z direction. In contrast, in-vivo values are fitted along the long axis of the mask, assuming equal contribution from all directions for in-plane conductivity (2×1D). (**C**) First- and second-order polynomial coefficients representing $|B_1^+|$ and ϕ^+ were estimated using 1D fitting. Conductivity was then derived from the resulting coefficients of the polynomial fit.

6.5. RESULTS

Masked complex B_1^+ component maps are illustrated in Figure 6.3A. A consistent field curvature is clearly visible in the phase images, and, to a lesser extent in the magnitude maps. Phantom conductivity maps (Figure 6.3B) show a low in-vial variation (<0.06 S/m) and clear contrast between the different saline concentrations. Excellent correlation (R^2=0.95) with the values expected from the prepared salinity (0.4-1.2 S/m) is observed [152].

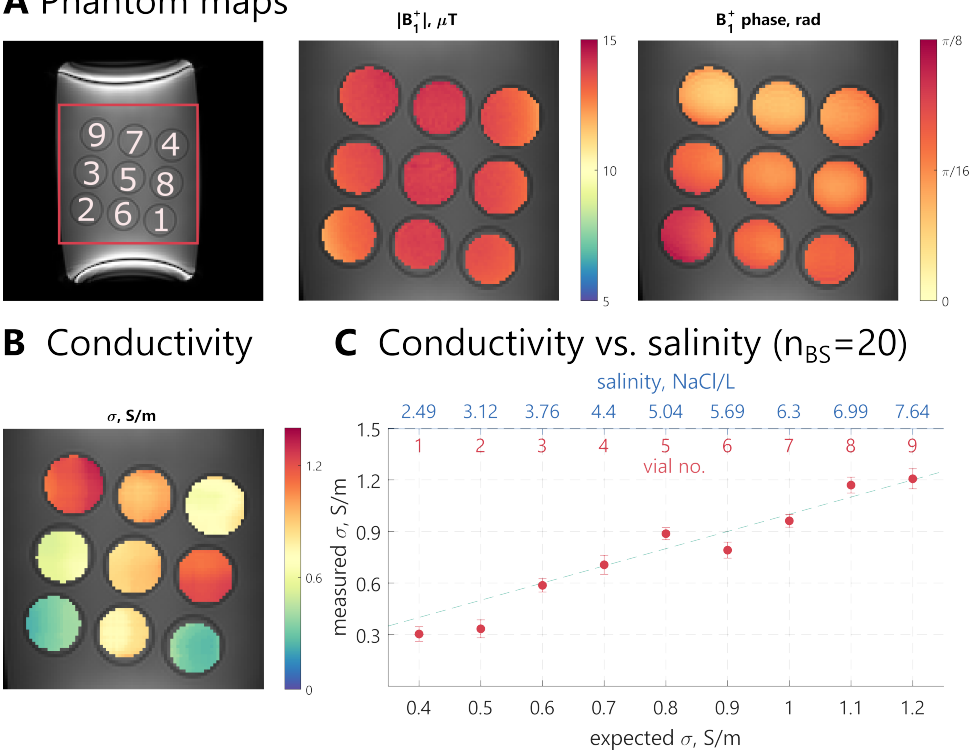

Figure 6.3.: Phantom results. (**A**) Representative baseline image, and corresponding masked $|B_1^+|$ and ϕ^+ maps acquired with the proposed method. (**B**) Corresponding filtered conductivity σ map, (**C**) Excellent correlation (R^2=0.95) between the measured conductivity in each vial against the expected conductivity at used saline concentration values (top) [152]. The green dashed line indicates the identity reference.

Representative subject maps are shown in Figure 6.4A. The B_1^+ magnitude and phase in the septum (masked region) exhibit a gradient along the long axis. Reconstructed in-plane (2×1D) conductivity σ' (0.74±0.02 S/m) is homogeneous throughout the ROI.The reconstructed σ' values showed an overall mean of 0.69±0.13 S/m across all subjects

(Figure 6.5).

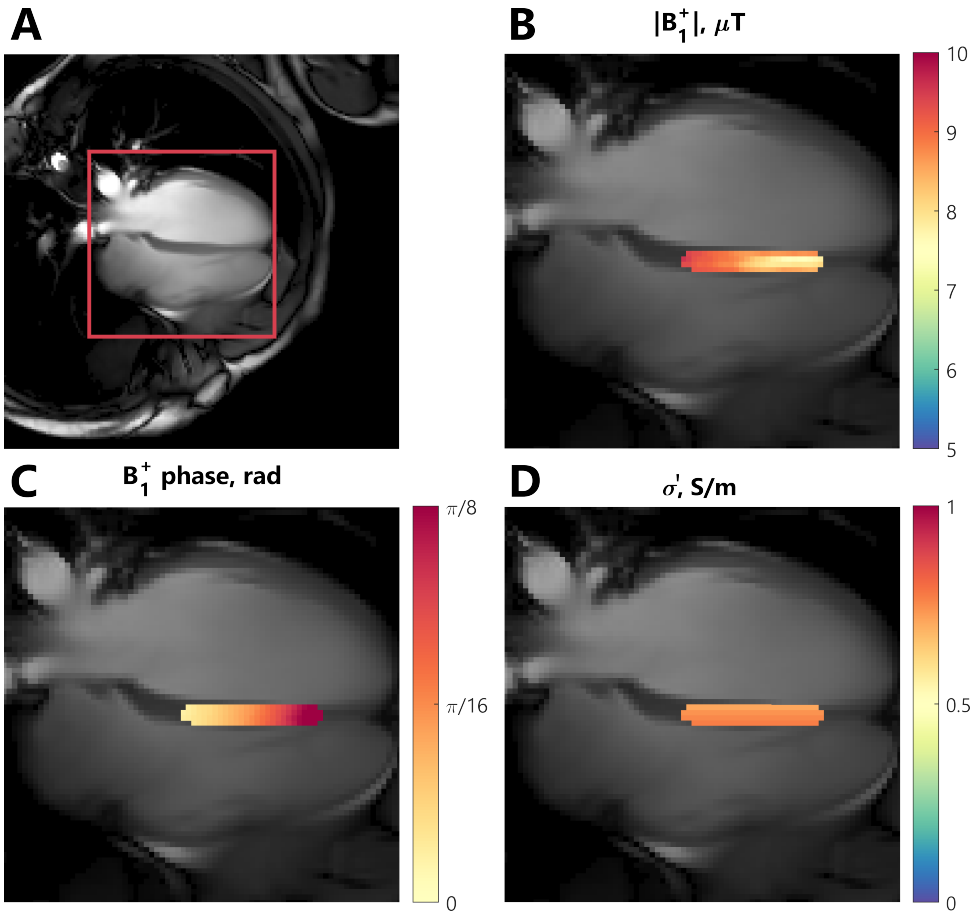

Figure 6.4.: Representative subject baseline image (**A**), B_1^+ magnitude (**B**) and phase (**C**) maps, as well as the reconstructed in-plane (2×1D) conductivity (**D**) in the septum of the myocardium (masked region of interest).

6.6. DISCUSSION

In this work, we present a new method for robust cardiac conductivity mapping using B_1^+ magnitude and phase extracted from a BS-prepared cardiac B_1^+ mapping sequence. In-vivo, an excellent agreement was achieved with the previously measured phase-based conductivity of 0.69 S/m [10]. Only conductivity was extracted from the acquired complex B_1^+ maps. Additional permittivity reconstruction is also feasible,

however, it is more sensitive to noise in B_1^+ magnitude. To provide sufficient $|B_1^+|$ quality, an increased number of baseline images can be acquired with the proposed free-breathing mapping technique by scaling the scan time. Thus, its application for robust cardiac conductivity and permittivity imaging warrants further investigation.

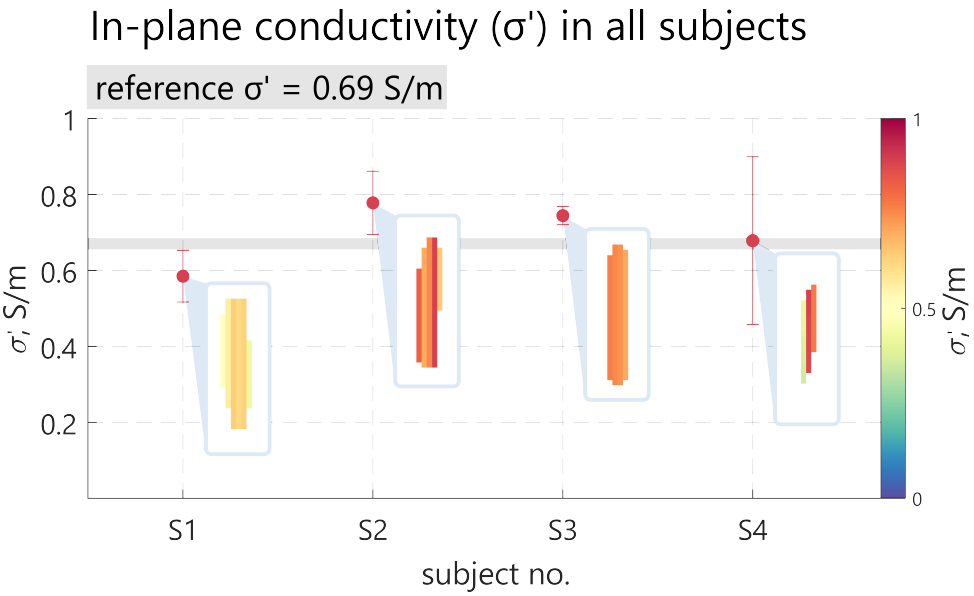

Figure 6.5.: Average reconstructed conductivity values across all four subjects, with the corresponding conductivity maps (mask along the septal ROI). The gray bar indicates the literature reference value of conductivity in the myocardium.

The proposed technique was acquired in 2D, thus, requiring boundary assumptions in the electrical property reconstruction. However, as the B_1^+ preparation is independent from the readout, the acquisition can easily be scaled to volumetric imaging. This warrants an exploration for more accurate cardiac EPT without the need for spatial assumptions.

6.7. CONCLUSION

The proposed complex B_1^+ mapping enables robust reconstruction of conductivity maps in the human heart from a single free-breathing acquisition.

7

ROBUST CARDIAC T_2^* MAPPING USING RF PHASE-CYCLED TRANSVERSE-MAGNETIZATION DECAY PREPARATIONS

This chapter is in proceedings: Šiurytė, P., Tourais, J., Zhao, Y., van de Steeg-Henzen, C., Tao, Q., Weingärtner, S., Henningsson, M. (2024). Robust cardiac T_2^* mapping using RF phase-cycled transverse-magnetization decay preparations. Proc. Journal of Cardiovascular Magnetic Resonance 26 (2024). London, 2024

7.1. BACKGROUND

T_2^* mapping is the clinical gold standard for myocardial iron assessment [153], and blood pool quantification is emerging as a promising marker for chamber oxygenation [154]. Clinically, T_2^* is typically measured with multi-gradient echo (mGRE) sequences that require long repetition times (TR) to sufficiently sample the decay [155]. This is particularly challenging for long T_2^* values, limiting resolution and/or coverage. Here, we investigate a novel method for cardiac T_2^* mapping, based on a radiofrequency (RF) phase-cycled T_2^* preparation module.

7.2. METHODS

The proposed module contains two 90° pulses, tipping the magnetization into and back from the transverse plane. The pulses are separated by time τ to facilitate T_2^* decay (Figure 7.1B). While the tip-down phase is fixed, tip-back phase α is varied between 0°-360° in n linear phase-cycling steps, so that the magnetization forms a sinusoidal function of α. This accounts for off-resonance $\Delta\omega$ induced phase shifts. The full imaging scheme (Figure 7.1A) includes: a non-prepared image (I_0), n T_2^*-prepared images, and a saturation-prepared image (I_s). After correcting for the readout using I_s, a sinusoid is fitted to the polarity restored prepared images, and its amplitude is compared to I_0 to estimate T_2^*.

T1MES phantom [146] and 3 healthy subjects (3 males, 26.0±2.2 y.o.) were imaged at 3T (Ingenia, Philips). The proposed method used ECG-triggered bSSFP single-shot images and was compared to mGRE (TE = 1,2,...,15 ms).

In phantom, τ=TE ms (n=36) prepared maps were acquired for direct comparison with mGRE. In addition, T_2^* maps were acquired in phantom (n = 36, τ = 80 ms) and in-vivo (n = 4, τ = 45,80,120 ms). Phantom data were studied for root mean square error (RMSE) between n = 36 and retrospectively undersampled data with n = 1,2,...35, to determine an adequate n for in-vivo imaging.

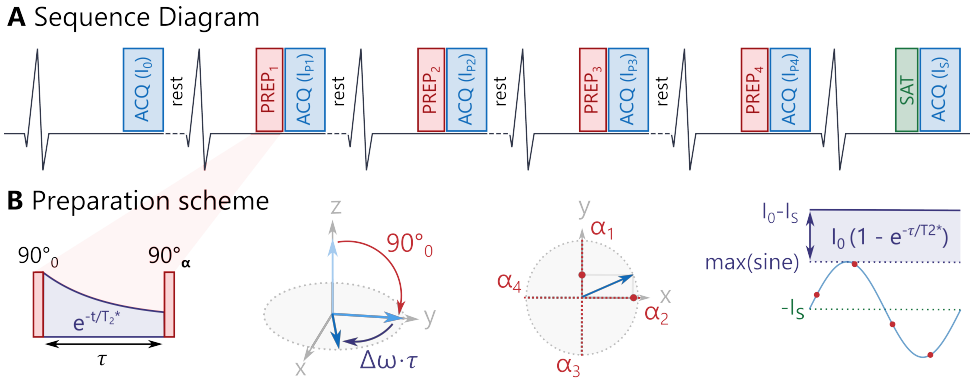

Figure 7.1.: (**A**) Pulse sequence diagram for the proposed preparation-based cardiac T_2^* mapping. 6 images (ACQ) are acquired in the end-diastole in a single breath-hold: one image without preparation (I_0), n images using a preparation module (I_{pn}) with cycled RF-pulse phase α (PREP$_n$), and one image (I_S) preceded by a saturation (SAT) pulse. A rest period of 3.5 s is performed before each prepared image. (**B**) Preparation scheme of the proposed approach. A 90°_0 RF pulse tips the magnetization to the transverse plane, followed by a T_2^* relaxation during a time τ where the magnetization dephases by $\Delta\omega \cdot \tau$. Finally, a 90_α° tip-back pulse is played. Pixel-wise T_2^* values are computed by fitting a sine curve to the phase-cycled data, correcting it for the effect of the imaging readout, and comparing it to the intensity in the non-prepared image.

7.3. RESULTS

Good mapping quality was achieved in phantom (Figure 7.2A), with the T_2^* decay closely matching mGRE sampled at τ=TE (Figure 7.2B). Due to limited sampling, mGRE shows poor quantification of long T_2^*, with strong overestimation compared with the proposed approach. When compared to a densely sampled map (n = 36), low RMSE (< 13 ms) was achieved for n > 3 (Figure 7.2C).

The proposed approach achieved more robust mapping in-vivo (Figure 7.3A). Across all subjects, mean myocardial T_2^* measured with τ = 45/80/120 ms was 16.4/20.0/27.1 ms, compared to 26.0 ms in mGRE, but with 61/68/59% reduced standard deviation (SD), respectively. Longer T_2^* times are measured for longer τ, as expected in the presence of non-exponential transverse decay [156].

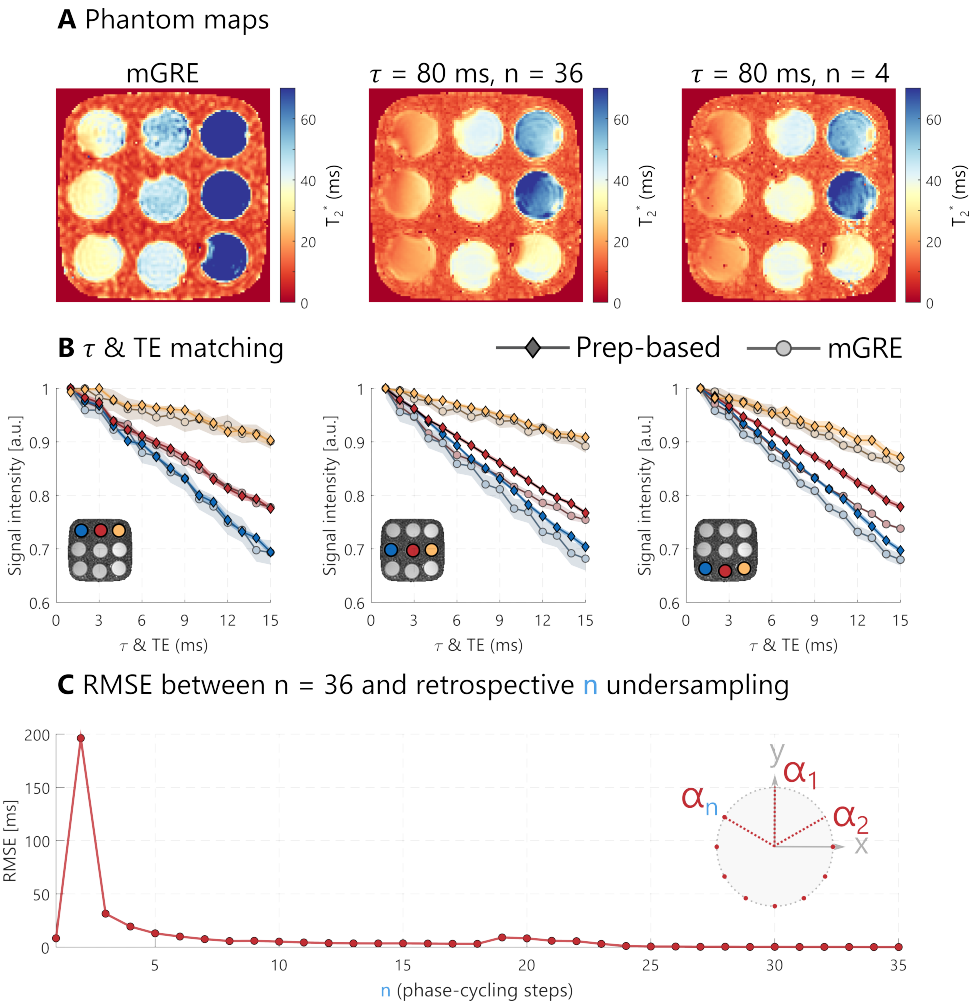

Figure 7.2.: (**A**) Phantom T_2^* maps were obtained with the mGRE (left), and the proposed approach with n = 36 (middle) and n = 4 (right). Very long T_2^* times are overestimated in the mGRE, compared with the T_2^*-prepared sequence. (**B**) T_2^* decay measured with the proposed preparation-based (diamonds) and mGRE (circles) sequences in all 9 T1MES phantom vials. **(C)** Root mean square error (RMSE) was measured between the correlation of the proposed method with n = 36 and n = 1,2,...,35. Imaging parameters: FOV = 300×300 mm^2, 2×2 mm^2 resolution, 10 mm slice thickness, SENSE factor of 2, flip angle = 40° (proposed) and 25° (mGRE), TR = 2.3 ms (proposed) and 16 ms (mGRE).

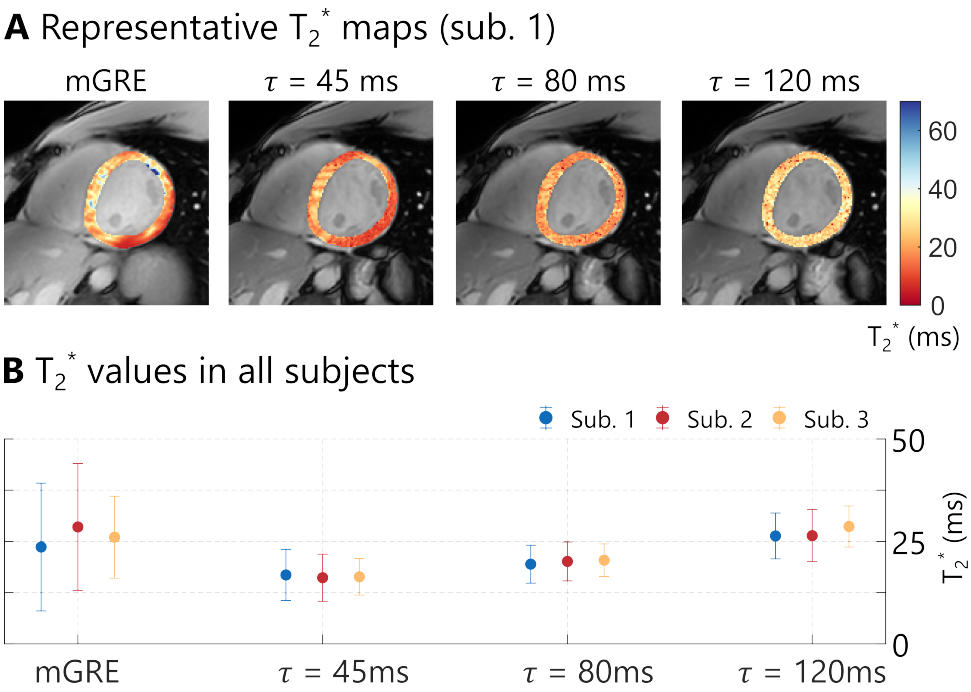

Figure 7.3.: Myocardial (**A**) T_2^* maps for a representative healthy subject, and (**B**) average T_2^* values for three healthy subjects. A multi-gradient echo (mGRE) approach was acquired (left column) and compared with the proposed approach for three different τ values (n = 4, resulting in a breath-hold duration of 18-20 s). The error bars represent the measured standard deviation (SD) in the respective region of interest. Image segmentation was performed using a deep learning-based approach (nnU-Net framework with Bayesian uncertainty estimation) [157]. Imaging parameters were equivalent to the phantom imaging.

7.4. CONCLUSION

The proposed T_2^* mapping approach provides robust quantification and visually improved quality. The proposed scheme allows tailored preparation times, flexibility in choosing the imaging readout, compatibility with retrospective image registration, and can be extended to high-resolution and/or 3D cardiac T_2^* mapping.

8

OUTLOOK AND CONCLUSION

8.1. RESEARCH OVERVIEW

This thesis tackles the challenges that arise from acoustic and electromagnetic wave field interactions in MR imaging at high magnetic field strengths. Today, around 50,000 MRI units exist worldwide, and while up to 70% of them operate at 1.5 T, systems at ≥3T are rapidly gaining popularity [13]. The associated issues of extremely high acoustic noise and non-uniform transmit field distribution hamper the smooth application of the latest high-field MRI hardware. To develop universal solutions, two research directions were explored: hardware-based system supplements and pulse sequence development.

Part I, containing Chapters 2 and 3, explored hardware-based solutions. In Chapter 2, a novel method for reducing the gradient acoustic noise was presented. Predictive Noise Canceling (PNC) utilized the Linear Time Invariant (LTI) model to predict the acoustic noise prior to its creation. The predicted anti-noise was superimposed to create a reduced noise zone at the target location. Using an experimental prototype based on pneumatic sound transmission, this approach achieved up to 13 dB noise reduction inside the scanner bore. Despite some sensitivity to MRI sequence parameters, the method showed robust noise reduction across a range of scanning procedures of varying duration.

In Chapter 3, a novel method for adaptive B_1^+ shimming was explored by using actively-coupled dielectric pads. In this method, the B_1^+ field was modulated by switching the electrical connections between small high-permittivity pockets. Up to 13 % B_1^+ magnitude modulation was achieved in electromagnetic field simulations when considering a slice at 15 mm depth. This was comparable to phantom experiments, where up to 11% field modulation was observed. The results have also demonstrated modular shimming with the ability to tune the shimming 'hotspot' location based on the selection of coupled pockets.

Part II, containing Chapters 4-7, described pulse sequence-based solutions for MRI. Particular emphasis was placed on cardiac MR (CMR) imaging. Due to the reduced RF wavelength in tissue at higher field strengths, the torso area is particularly affected by aggravated transmit field B_1^+ inhomogeneities. Additionally, extra difficulties are posed by the cardiac and respiratory motion. In CMR, the need to reduce motion-induced artifacts and to minimise the acquisition times is imminent, compared to more inert applications like neuroimaging.

The particular relevance of the CMR application and latest advances in this field are elaborated on in Chapter 4. In addition to qualitative imaging and relaxometry to measure T_1, T_2 and T_2^*, novel biomarkers are appearing, such as $T_{1\rho}$ and $T_{2\rho}$, magnetization transfer (MT), chemical exchange saturation transfer (CEST) or electrical properties tomography (EPT) [10, 158–162]. Some common pitfalls of robust cardiac sequence design were highlighted. Specifically, B_0/B_1^+ field inhomogeneities and cardiac motion were recognised as prevailing challenges.

To allow for B_1^+ mapping in the heart with improved map quality and robustness, Chapter 5 presented a novel transmit field mapping technique targeted for CMR. The method, based on Bloch-Siegert shift (BSS) preparations, was studied using Bloch simulations, phantom, and in-vivo experiments. Simulations have shown the versatility of the proposed preparation module, enabling custom high-sensitivity B_1^+ mapping ranges by varying preparation pulse parameters. In phantoms and in-vivo, the proposed BSS-prepared method greatly outperformed the conventional phase-based BSS mapping. The method has also shown robust performance in whole-heart 3D acquisition of B_1^+ map in a single breath hold.

Adapting the proposed B_1^+ mapping technique, Chapter 6 demonstrates the possibility of complex B_1^+ map-based EPT. To this end, conductivity was reconstructed from complex B_1^+ maps in a saline phantom and in four healthy subjects. Phantom results have shown great correlation with the expected conductivity based on the input salt concentrations. In vivo, the reconstructed in-plane conductivity values were found to be in agreement with the reported literature.

Finally, Chapter 7 presents a novel cardiac mapping sequence for T_2^* mapping. To overcome the limitations of the conventional multi-gradient echo (mGRE) method with long repetition times (TRs), a preparation-based method was explored. The method has shown good agreement with mGRE method in phantom and in-vivo experiments, as well as greatly reduced noise across the myocardium.

8.2. CURRENT DEVELOPMENTS

8.2.1. ACOUSTIC NOISE

Novel compensation strategies to reduce the acoustic noise in MRI remain an active research area. Silent gradient coils have been proposed, utilizing ultra-fast switching modes to push the sound above the hearing threshold [163]. Initial studies in this field reported little to no risk of peripheral nerve stimulation (PNS), although the potential hearing damage risk due to exposure to ultrasonic frequencies requires further assessment. While ultra-fast gradient switching requires complex acquisition mechanisms, this approach may be promising for advanced applications, such as in functional MRI research [14].

Advanced gradient hardware has also been developed in the form of insert gradient coils - additional inserts designed for a particular anatomy to enhance performance. Due to the reduced gradient coil size, high amplitudes and slew rates are achieved, enabling imaging at particularly high resolution. Notably, the reduced mass may also lead to amplified mechanical vibrations, causing higher perceived acoustic noise, particularly in head-coil use [14]. Nevertheless,

advanced reduced-noise head gradient inserts for 7 T systems have been suggested, making the insert gradients promising for ultra-high resolution imaging without further elevated acoustic noise [164].

Acoustic noise reduction via pulse sequence gradient input adjustment remains popular in research [165, 166]. Reduced-noise pulse sequence modes are also commonly implemented by MRI vendors [167]. Nevertheless, the adjustments to regular scanning protocols may affect acquisition speeds or imaging quality. While this trade-off requires additional consideration, sequence adjustments offer substantial noise reduction without the need for additional equipment.

Active noise canceling (ANC) in MRI is gaining interest, with the first appearing ANC systems available for commercial use [61, 62]. In this area, novel products for ultra-high field applications are developed. Compact ANC hardware is particularly useful in functional MRI studies, where the space inside the head coil is highly limited [61].

8.2.2. B_1^+ field

Currently, multiple transmit coil systems present the most complete method for B_1^+ shimming in high magnetic field strengths. However, only single transmit channel 7 T systems have been approved by the US Food and Drug Administration (FDA). As a result, clinical applications of ultra-high field systems are limited by prevalent RF field inhomogeneity [168].

Dielectric pads used for the RF shimming in MRI have conventionally employed homogeneous slabs of high permittivity materials. However, common constituent materials, such as barium titanate, are toxic to humans, costly, and the stability of dielectric pad properties may change over time. To address these challenges, the use of artificial dielectrics has been suggested [81, 169]. These materials are composed as capacitive grids, and present a viable alternative to tailored, static dielectric pads.

To cater for the B_1^+ inhomogeneities at higher magnetic field strengths, sequences that are accurate across larger dynamic ranges are of interest [170]. Recent efforts in pulse sequence development for B_1^+ mapping have been focused on efficient transmit field calibration schemes for multi-transmit systems, by either performing simultaneous multi-channel mapping [171, 172] or by accelerating channel-wise B_1^+ map acquisition [173].

8.2.3. Low-field MRI

Notably, low-field MRI (e.g. 50-80 mT) research is gaining popularity as an accessible alternative to costly superconducting magnets required at high magnetic field strengths [174–176]. This approach offers

great advantage due to low gradient acoustic noise and minimal RF inhomogeneity. Furthermore, it reduces the associated costs, device portability and power consumption, albeit at the expense of reduced SNR. As a result, advanced, noise-resilient acquisition and reconstruction strategies are required. The trend towards low magnetic field strengths highlights the need for cost-effective MRI equipment. Similarly, the need for accessible MR solutions is also applicable to mid- and high-field MRI, where building and power consumption costs are greatly inflated.

8.3. RESEARCH IMPACT

8.3.1. HARDWARE-BASED SOLUTIONS

Most recent MRI hardware, such as gradient coils with advanced mechanical vibration damping, or multi-transmit coils, is tailored to alleviate the challenges of high magnetic field MRI. Nevertheless, the latest technology is currently only available in newly-installed, top-of-the-line scanners. The majority of current clinical scanning sites suffer from unwanted acoustic and electromagnetic field interactions. One solution to this could be timely updates of the integral scanner hardware. However, such upgrades prior to the end of the typical MRI scanner lifetime of 10-15 years [177] are neither sustainable nor cost-efficient. Instead, adaptive add-on solutions to mitigate the issues of the extreme acoustic noise and B_1^+ field inhomogeneity could fill the gap in commercially available methodologies for universal field corrections. Both PNC and active dielectric shimming therefore have a potential for high-demand in modern MRI applications.

PNC, as a headphone-based method, could be particularly easy to install, when combined with standard patient communication headsets in MRI. We have shown that substantial noise reduction can be achieved with pneumatic systems, currently used in clinical scanners. However, this approach would still require the installation of high-fidelity microphones to obtain precise gradient coil acoustic transfer functions. More realistically, PNC could be applied in the form of a complete headphone product, with integrated microphones and optical-fiber sound transmission for higher sound output accuracy, compared to pneumatic drivers. Overall, this would still present an affordable add-on solution to the imminent issue of noise reduction. In addition to the subjective noise-canceling for the patient, such a product would also help to improve gradient noise filtering in patient-to-technician communication.

As discussed in Chapter 3, B_1^+ shimming with actively coupled dielectric arrays could also be smoothly integrated, for instance, in the form of an independent plug-in device, or, in combination with the RF coils. Nevertheless, the current method falls behind in technology readiness for widespread application. In order to present a viable alternative to multi-transmit coil method, a large number of shimming

fine-tuning options may be required. Since the goal of the work in this thesis was to provide a proof-of-concept, the extensive range of possible coupling configurations and shimming device parameters was not yet explored. On the other hand, even a limited selection of shimming modes presents great advantage compared to static dielectric pads for remote tuning of the B_1^+ field.

8.3.2. MRI PULSE SEQUENCE DESIGN

Since the selection of B_1^+ mapping techniques suitable for cardiac imaging remains limited, novel robust methods are of high interest. To this end, preparation-based mapping methods are promising, as they offer complete readout customization, as well as an easy extension to 3D imaging. BSS preparation presented in this thesis has shown successful and robust mapping at 3T, although the sequence poses a few considerations in practical application. Firstly, while the BSS-prepared B_1^+ mapping has shown superior resilience to reconstruction bias due to tissue relaxation properties, the eight-pulse preparation module leads to in considerable specific absorption rate (SAR), when compared to sub-adiabatic pulse-prepared sequences [142]. Furthermore, the method has been optimized for a typical RF inhomogeneity range observed at 3T body imaging. An optimal implementation in other magnetic field strengths warrants further tuning to optimize the sequence sensitivity to noise.

Complex B_1^+ mapping based conductivity reconstruction, described in Chapter 6, presents an advent of full cardiac electrical properties mapping. While only the conductivity value was evaluated, further studies are warranted to present the feasibility of mapping tissue permittivity. As evident from Equation (1.5), for a small conductivity-induced imaginary component, permittivity can be approximated as dependent on the magnitude of B_1^+ only. Since mapping the phase of B_1^+ field in the heart is far more established than the magnitude quantification, only primarily phase-dependent conductivity reconstruction has been explored so far [10]. The development of novel cardiac B_1^+ magnitude mapping sequences, such as presented in this thesis, are therefore highly promising for the full evaluation of electrical properties of the heart. Nevertheless, for cardiac EPT integration in clinical practice, further improvements in sequence robustness and validation are needed. In addition, further research is required to establish the pathological indications of cardiac EPT.

The conductivity reconstruction introduced in this thesis presents an in-plane (2D) value, assuming that the omitted third dimension does not introduce considerable measurement bias. It has been shown that the distribution of the three orthogonal axes components of EPs is determined by the relative anatomy dimension lengths [178]. Therefore,

for similar inter-subject heart anatomies, this assumption is expected to be valid [10]. Nevertheless, further comparison across various subjects would verify the robustness of reduced-dimensionality EPT in the heart.

Another possible source of bias in EPT reconstruction is posed by the assumption that the phase of B_1^+ field can be approximated as half of the measured transceive phase. While this assumption is mostly valid at 3T, it is increasingly violated at ultra-high magnetic field strengths, where the circular polarization of the B_1^+ becomes more distorted to an elliptical geometry due to scattered RF fields [150]. Alternative transmitted field phase measurement methods for EPT, such as relative phase derivation from multi-transmit coil measurements, might be considered.

T_2^* mapping method, presented in Chapter 7, has shown more robustness to noise compared to a conventional mGRE method. The proposed sequence has the intrinsic advantage of a long preparation time option, which is difficult to achieve with mGRE method without greatly prolonged acquisition times. This may be of particular interest to characterize long T_2^* times, such as in the cardiac blood pools. Here, mapping the transverse-magnetization relaxation rates may be promising for quantifying the chamber oxygenation levels [154]. To verify potential applications of the proposed sequence, further experiments for the use in the heart are required.

8.4. FUTURE DIRECTIONS

The research presented in this thesis opens up a new range of methodologies and gives grounds for further research work. In particular, the following directions could be considered for the next immediate steps:

- **Predictive Noise Canceling.** The current work has presented noise reduction based on a pneumatic prototype with a single audio channel. A simultaneous dual-channel headphone experiment design could be applied for the first in-vivo measurements. This could be used to evaluate the subjective sound pressure levels with/without PNC and to disentangle the noise reduction contributions from passive reduction (earplugs) and the applied anti-noise. Furthermore, the effect of various in-scan parameters, such as potential gradient heating, and subject motion, should be assessed to establish the need for PNC re-calibration. In a presented pilot study, a one-minute calibration procedure has been proposed. This may be greatly optimized in future studies, by reducing the pulse-to-pulse breaks or the number of averaging. Alternatively, non-linear acoustic noise modeling could also present the next immediate steps in improving the maximum theoretical noise reduction. Finally, PNC could be explored for the creation

of larger silent zones. In this approach, an array of spatially distributed speakers would be utilized, negating the sound pressure waves within a defined volume around the subject's head.

- **Active dielectric shimming.** To explore the full potential of the proposed actively-coupled dielectric array, further array optimization should be conducted. In simulations, B_1^+ field modulation in human models warrant systematic investigation, with various sets of shimming array geometries and electrical properties. To improve the magnitude of B_1^+ shimming at the anatomies of interest, such as the heart, the use of ultra-high permittivity materials ($\epsilon_r \geq 1000$) may be utilized. Due to their compact nature, these may be of particular interest for neuroimaging in ultra-high magnetic field strengths.

- **Cardiac B_1^+ mapping.** The proposed preparation-based sequence using Bloch-Siegert shifts could be further evaluated at lower or higher magnetic field strengths, such as 1.5 T or 7 T, where the dynamic range of B_1^+ greatly differs. This would require additional preparation sensitivity tailoring to improve the noise resilience. Nonetheless, the work in this thesis has presented several options for tailored preparations to shift the B_1^+ range with optimal sensitivity. Furthermore, future research efforts targeting the development of B_1^+ mapping methods with further reduced SAR are warranted. This would be particularly useful for fast calibration of multi-channel systems, as well as for high-resolution applications such as EPT.

- **Cardiac EPT.** Using the proposed complex B_1^+ mapping methodology, permittivity mapping in the human myocardium could be performed. To expand the method validation in inert anatomy, calf-muscle imaging may be considered for both conductivity and permittivity mapping. This could be followed by patient-study validation, establishment of indicative cardiomyopathies, as well as comparison with other relevant biomarkers. Faster and higher-resolution B_1^+ mapping methods could also be explored to enable more robust EP quantification. The use of 3D acquisitions would also enable the full evaluation of the electrical properties in the heart, as well as the comparison with reduced-dimensionality EPT. Finally, > 3T applications could be explored, resulting in larger B_1^+ field curvature in tissue, and hence an increased contrast.

- **Preparation-based T_2^* mapping.** To improve the proposed sequence resilience to magnetic field inhomogeneities, the use of adiabatic pulses could be explored. Replacing the hard 90° tip-down and tip-up pulses with, for instance, half-passage hyperbolic-secant pulses warrants future investigation. Imaging data in a larger

cohort of healthy subjects and clinical patients should be acquired to establish the sequence robustness. Finally, the evaluation of blood-pool T_2^* values should be explored.

8.5. CONCLUSION

This thesis has presented novel methods to measure and characterize the acoustic and electromagnetic waves in MRI. In particular, the proposed solutions tackled the issues of extreme acoustic noise and the transmitted RF field inhomogeneity in high magnetic field strengths. The proposed acoustic noise reduction method, predictive noise canceling, has enabled robust sound pressure attenuation, and is highly promising as a cost-efficient and universal solution. Similarly, active dielectric shimming has enabled adaptive remote modulation of B_1^+ field, and could be utilized as an accessible alternative to multiple-transmit coils. The proposed B_1^+ mapping technique has shown robust results in heart imaging, and has shown to enable the reconstruction of complex B_1^+ field-based conductivity values of the myocardium. This paves the way for future EPT applications in cardiac MRI, where full complex permittivity can be mapped. Finally, the described T_2^* mapping method improved resilience to noise and field inhomogeneities, when compared to a conventional mapping method, and is promising for robust mapping of slower relaxation rates in the heart.

BIBLIOGRAPHY

[1] Oecd. *OECD statistics*. https://stats.oecd.org/. Accessed on April 8, 2024. 2024.

[2] S. R. More, T. C. Lim, M. Li, C. K. Holland, S. E. Boyce, and J.-H. Lee. “Acoustic noise characteristics of a 4 Telsa MRI scanner”. In: *Journal of Magnetic Resonance Imaging* 23.3 (2006), pp. 388–397.

[3] M. J. McJury. “Acoustic Noise and Magnetic Resonance Imaging: A Narrative/Descriptive Review”. In: *Journal of Magnetic Resonance Imaging* 55.2 (2022), pp. 337–346.

[4] R. E. Brummett, J. M. Talbot, and P. Charuhas. “Potential hearing loss resulting from MR imaging.” In: *Radiology* 169.2 (1988). PMID: 3175004, pp. 539–540.

[5] F. G. Shellock and J. V. Crues. “MR procedures: biologic effects, safety, and patient care”. In: *Radiology* 232.3 (2004), pp. 635–652.

[6] O. Dietrich, M. F. Reiser, and S. O. Schoenberg. “Artifacts in 3-T MRI: physical background and reduction strategies”. In: *European journal of radiology* 65.1 (2008), pp. 29–35.

[7] N. T. Roberts, L. A. Hinshaw, T. J. Colgan, T. Ii, D. Hernando, and S. B. Reeder. “B0 and B1 inhomogeneities in the liver at 1.5 T and 3.0 T”. In: *Magnetic resonance in medicine* 85.4 (2021), pp. 2212–2220.

[8] K. Sung and K. S. Nayak. “Measurement and characterization of RF nonuniformity over the heart at 3T using body coil transmission”. In: *Journal of Magnetic Resonance Imaging: An Official Journal of the International Society for Magnetic Resonance in Medicine* 27.3 (2008), pp. 643–648.

[9] U. Katscher, D.-H. Kim, and J. K. Seo. “Recent progress and future challenges in MR electric properties tomography”. In: *Computational and mathematical methods in medicine* 2013.1 (2013), p. 546562.

[10] U. Katscher and S. Weiss. “Mapping electric bulk conductivity in the human heart”. In: *Magnetic Resonance in Medicine* 87.3 (2022), pp. 1500–1506.

[11] R. W. Brown, Y.-C. N. Cheng, E. M. Haacke, M. R. Thompson, and R. Venkatesan. *Magnetic resonance imaging: physical principles and sequence design*. John Wiley & Sons, 2014.

[12] J. Tourais, C. Coletti, and S. Weingärtner. “Brief Introduction to MRI Physics”. In: *Advances in Magnetic Resonance Technology and Applications*. Vol. 7. Elsevier, 2022, pp. 3–36.

[13] R. P.A. *Magnetic Resonance in Medicine. The Basic Textbook of the European Magnetic Resonance Forum*. Digital version 14.2, 14th edition, 2024.

[14] N. Gudino and S. Littin. “Advancements in gradient system performance for clinical and research MRI”. In: *Journal of Magnetic Resonance Imaging* 57.1 (2023), pp. 57–70.

[15] B. Heismann, M. Ott, and D. Grodzki. “Sequence-based acoustic noise reduction of clinical MRI scans”. In: *Magnetic Resonance in Medicine* 73.3 (2015), pp. 1104–1109.

[16] G. J. Hoiting. “Measuring MRI noise”. In: (2005).

[17] D. Tomasi and T. Ernst. “A simple theory for vibration of MRI gradient coils”. In: *Brazilian Journal of Physics* 36 (2006), pp. 34–39.

[18] R. C. Katz, L. Wilson, and N. Frazer. “Anxiety and its determinants in patients undergoing magnetic resonance imaging”. In: *Journal of behavior therapy and experimental psychiatry* 25.2 (1994), pp. 131–134.

[19] G. Tazegul, E. Etcioglu, F. Yildiz, R. Yildiz, and D. Tuney. “Can MRI related patient anxiety be prevented?” In: *Magnetic resonance imaging* 33.1 (2015), pp. 180–183.

[20] M. E. Quirk, A. J. Letendre, R. A. Ciottone, and J. F. Lingley. “Anxiety in patients undergoing MR imaging.” In: *Radiology* 170.2 (1989). PMID: 2911670, pp. 463–466.

[21] E. Kanal, F. G. Shellock, and L. Talagala. “Safety considerations in MR imaging.” In: *Radiology* 176.3 (1990). PMID: 2202008, pp. 593–606.

[22] R. Salvi and A. Sheppard. “Is Noise in the MR Imager a Significant Risk Factor for Hearing Loss?” In: *Radiology* 286.2 (2018). PMID: 29356640, pp. 609–610.

[23] O. Safety, H. Administration, *et al.* “1910.95, Occupational noise exposure”. In: *United States Department of Labor*. United States Department of Labor Washington DC, 2011.

[24] NHS. *MRI scan*. https://www.nhs.uk/conditions/mri-scan. Accessed on April 8, 2024. 2024.

[25] M. E. Ravicz, J. R. Melcher, and N. Y.-S. Kiang. “Acoustic noise during functional magnetic resonance imaging”. In: *The Journal of the Acoustical Society of America* 108.4 (2000), pp. 1683–1696.

[26] S. A. Winkler, A. Alejski, T. Wade, C. A. McKenzie, and B. K. Rutt. “On the accurate analysis of vibroacoustics in head insert gradient coils”. In: *Magnetic resonance in medicine* 78.4 (2017), pp. 1635–1645.

[27] F. Schmitt, S. Nowak, and E. Eberlein. *An Attempt to Reconstruct the History of Gradient-System Technology at Siemens*. 2020.

[28] R. A. Hedeen and W. A. Edelstein. “Characterization and prediction of gradient acoustic noise in MR imagers”. In: *Magnetic Resonance in Medicine* 37.1 (1997), pp. 7–10.

[29] C. V. Rizzo Sierra, M. J. Versluis, J. M. Hoogduin, and H. Duifhuis. “Acoustic fMRI Noise: Linear Time-Invariant System Model”. In: *IEEE Transactions on Biomedical Engineering* 55.9 (2008), pp. 2115–2123.

[30] Z. Wu, Y.-C. Kim, M. C. Khoo, and K. S. Nayak. “Evaluation of an independent linear model for acoustic noise on a conventional MRI scanner and implications for acoustic noise reduction”. In: *Magnetic Resonance in Medicine* 71.4 (2014), pp. 1613–1620.

[31] T. Hamaguchi, T. Miyati, and e. a. Ohno. “Acoustic noise transfer function in clinical MRI: a multicenter analysis”. In: *Academic radiology* 18.1 (2011), pp. 101–106.

[32] S. R. More, T. C. Lim, M. Li, C. K. Holland, S. E. Boyce, and J.-H. Lee. “Acoustic noise characteristics of a 4 Telsa MRI scanner”. In: *Journal of Magnetic Resonance Imaging* 23.3 (2006), pp. 388–397.

[33] L. Shtrepi, V. F. D. Poggetto, C. Durochat, M. Dubois, D. Bendahan, F. Nistri, M. Miniaci, N. M. Pugno, and F. Bosia. “Acoustic noise levels and field distribution in 7 T MRI scanners”. In: *Frontiers in Physics* 11 (2023), p. 1284659.

[34] C. M. Collins, W. Liu, W. Schreiber, Q. X. Yang, and M. B. Smith. “Central brightening due to constructive interference with, without, and despite dielectric resonance”. In: *Journal of Magnetic Resonance Imaging* 21.2 (2005), pp. 192–196.

[35] F. Schick. “Whole-body MRI at high field: technical limits and clinical potential”. In: *European radiology* 15 (2005), pp. 946–959.

[36] T.-K. Truong, D. W. Chakeres, D. Q. Beversdorf, D. W. Scharre, and P. Schmalbrock. “Effects of static and radiofrequency magnetic field inhomogeneity in ultra-high field magnetic resonance imaging”. In: *Magnetic resonance imaging* 24.2 (2006), pp. 103–112.

[37] R. Pohmann and K. Scheffler. “A theoretical and experimental comparison of different techniques for B1 mapping at very high fields”. In: *NMR in Biomedicine* 26.3 (2013), pp. 265–275.

[38] D. I. Hoult. “Sensitivity and power deposition in a high-field imaging experiment”. In: *Journal of Magnetic Resonance Imaging* 12.1 (2000), pp. 46–67.

[39] V. L. Yarnykh. “Actual flip-angle imaging in the pulsed steady state: a method for rapid three-dimensional mapping of the transmitted radiofrequency field”. In: *Magnetic Resonance in Medicine: An Official Journal of the International Society for Magnetic Resonance in Medicine* 57.1 (2007), pp. 192–200.

[40] S. Gavazzi, Y. Shcherbakova, L. W. Bartels, L. J. Stalpers, J. J. Lagendijk, H. Crezee, C. A. van den Berg, and A. L. van Lier. “Transceive phase mapping using the PLANET method and its application for conductivity mapping in the brain”. In: *Magnetic resonance in medicine* 83.2 (2020), pp. 590–607.

[41] U. Katscher and C. A. van den Berg. “Electric properties tomography: Biochemical, physical and technical background, evaluation and clinical applications”. In: *NMR in Biomedicine* 30.8 (2017), e3729.

[42] J. Liu, Y. Wang, U. Katscher, and B. He. “Electrical properties tomography based on B1 maps in MRI: principles, applications, and challenges”. In: *IEEE Transactions on Biomedical Engineering* 64.11 (2017), pp. 2515–2530.

[43] X. Zhang, J. Liu, and B. He. “Magnetic-resonance-based electrical properties tomography: a review”. In: *IEEE reviews in biomedical engineering* 7 (2014), pp. 87–96.

[44] R. Leijsen, W. Brink, C. van den Berg, A. Webb, and R. Remis. “Electrical properties tomography: A methodological review”. In: *Diagnostics* 11.2 (2021), p. 176.

[45] I. E. Commission *et al.* “Medical electrical equipment-Part 2-33: Particular requirements for the basic safety and essential performance of magnetic resonance equipment for medical diagnosis”. In: *IEC 60601-2-33 Ed. 3.0* (2010).

[46] P. Lanzer, C. Barta, E. Botvinick, H. Wiesendanger, G. Modin, and C. Higgins. “ECG-synchronized cardiac MR imaging: method and evaluation.” In: *Radiology* 155.3 (1985), pp. 681–686.

[47] R. L. Ehman and J. P. Felmlee. “Adaptive technique for high-definition MR imaging of moving structures.” In: *Radiology* 173.1 (1989), pp. 255–263.

[48] T. D. Nguyen, P. Spincemaille, M. D. Cham, J. W. Weinsaft, M. R. Prince, and Y. Wang. “Free-breathing 3D steady-state free precession coronary magnetic resonance angiography: Comparison of diaphragm and cardiac fat navigators”. In: *Journal of Magnetic Resonance Imaging: An Official Journal of the International Society for Magnetic Resonance in Medicine* 28.2 (2008), pp. 509–514.

[49] Medicines and H. P. R. A. (MHRA). *Safety guidelines for magnetic resonance imaging equipment in clinical use*. 2021.

[50] R. E. Evans, S. A. Taylor, S. Beare, S. Halligan, A. Morton, A. Oliver, A. Rockall, and A. Miles. “Perceived patient burden and acceptability of whole body MRI for staging lung and colorectal cancer; comparison with standard staging investigations”. In: *The British journal of radiology* 91.1086 (2018), p. 20170731.

[51] Z. Cho, S. Park, J. Kim, S. Chung, S. Chung, J. Chung, C. Moon, J. Yi, C. Sin, and E. Wong. “Analysis of acoustic noise in MRI”. In: *Magnetic Resonance Imaging* 15.7 (1997), pp. 815–822. issn: 0730-725X.

[52] S. A. Winkler, F. Schmitt, H. Landes, J. de Bever, T. Wade, A. Alejski, and B. K. Rutt. “Gradient and shim technologies for ultra high field MRI”. In: *NeuroImage* 168 (2018). Neuroimaging with Ultra-high Field MRI: Present and Future, pp. 59–70. issn: 1053-8119.

[53] M. E. Ravicz and J. R. Melcher. “Isolating the auditory system from acoustic noise during functional magnetic resonance imaging: examination of noise conduction through the ear canal, head, and body”. In: *The Journal of the Acoustical Society of America* 109.1 (2001), pp. 216–231.

[54] Y. Yamashita. “Quiet Technology of MRI.” In: *Igaku Butsuri: Nihon Igaku Butsuri Gakkai Kikanshi= Japanese Journal of Medical Physics: an Official Journal of Japan Society of Medical Physics* 36.2 (2016), pp. 110–112.

[55] S. M. Jacobs, E. Versteeg, A. G. van der Kolk, L. N. Visser, Í. A. Oliveira, E. van Maren, D. W. Klomp, and J. C. Siero. “Image quality and subject experience of quiet T1-weighted 7-T brain imaging using a silent gradient coil”. In: *European radiology experimental* 6.1 (2022), p. 36.

[56] M. McJury, R. Stewart, D. Crawford, and E. Toma. “The use of active noise control (ANC) to reduce acoustic noise generated during MRI scanning: Some initial results”. In: *Magnetic Resonance Imaging* 15.3 (1997), pp. 319–322. issn: 0730-725X.

[57] M. Li, B. Rudd, T. C. Lim, and J.-H. Lee. “In situ active control of noise in a 4 T MRI scanner”. In: *Journal of Magnetic Resonance Imaging* 34.3 (2011), pp. 662–669.

[58] N. Lee, Y. Park, and G. W. Lee. “Frequency-domain active noise control for magnetic resonance imaging acoustic noise”. In: *Applied Acoustics* 118 (2017), pp. 30–38. issn: 0003-682X.

[59] M. Inc. *MRI Stereo*. https://mriaudio.com/. Accessed on April 8, 2024. 2024.

[60] M. Stereo. *MRI Stereo*. https://mristereo.com/. Accessed on April 8, 2024. 2024.

[61] OptoAcoustics. *OptoActive II ANC Headphones*. https://www.optoacoustics.com/medical/optoactive-ii. Accessed on April 8, 2024. 2024.

[62] N. AS. *nordicAudio*. https://www.nordicneurolab.com/nordicaudio/. Accessed on April 8, 2024. 2024.

[63] I. Juvanna and U. Ramachandraiah. “Acoustic noise reduction in MRI-A Review”. In: *Indian J Sci Technol* 9 (2016), p. 39.

[64] J. Nussbaum, B. E. Dietrich, B. J. Wilm, and K. P. Pruessmann. “Thermal variation in gradient response: measurement and modeling”. In: *Magnetic Resonance in Medicine* 87.5 (2022), pp. 2224–2238.

[65] R. T. Inc. *Audio Stimulation*. http://www.mrivideo.com/audio-stimulation.php. Accessed on April 8, 2024. 2024.

[66] C. R. S. Ltd. *BOLDfonic*. https://www.crsltd.com/tools-for-functional-imaging/audio-for-fmri/boldfonic/. Accessed on April 8, 2024. 2024.

[67] E. Berger and J. Kerivan. “Influence of physiological noise and the occlusion effect on the measurement of real-ear attenuation at threshold”. In: *The Journal of the Acoustical Society of America* 74.1 (1983), pp. 81–94.

[68] J. Chambers, D. Bullock, Y. Kahana, A. Kots, and A. Palmer. “Developments in active noise control sound systems for magnetic resonance imaging”. In: *Applied Acoustics* 68.3 (2007). Application of Acoustics to Medicine, pp. 281–295. issn: 0003-682X.

[69] D. L. Price, J. P. De Wilde, A. M. Papadaki, J. S. Curran, and R. I. Kitney. “Investigation of acoustic noise on 15 MRI scanners from 0.2 T to 3 T”. In: *Journal of Magnetic Resonance Imaging* 13.2 (2001), pp. 288–293.

[70] A. Moelker, P. A. Wielopolski, and P. M. Pattynama. “Relationship between magnetic field strength and magnetic-resonance-related acoustic noise levels”. In: *Magnetic Resonance Materials in Physics, Biology and Medicine* 16 (2003), pp. 52–55.

[71] J. McNulty and S. McNulty. “Acoustic noise in magnetic resonance imaging: An ongoing issue”. In: *Radiography* 15.4 (2009), pp. 320–326. issn: 1078-8174.

[72] M. Dewey, T. Schink, and C. F. Dewey. “Claustrophobia during magnetic resonance imaging: Cohort study in over 55,000 patients”. In: *Journal of Magnetic Resonance Imaging* 26.5 (2007), pp. 1322–1327.

[73] M. A. Bernstein, J. Huston III, and H. A. Ward. “Imaging artifacts at 3.0 T”. In: *Journal of Magnetic Resonance Imaging: An Official Journal of the International Society for Magnetic Resonance in Medicine* 24.4 (2006), pp. 735–746.

[74] M. Kataoka, H. Isoda, Y. Maetani, Y. Nakamoto, T. Koyama, S. Umeoka, K. Tamai, A. Kido, N. Morisawa, T. Saga, *et al.* “MR imaging of the female pelvis at 3 Tesla: evaluation of image homogeneity using different dielectric pads”. In: *Journal of Magnetic Resonance Imaging: An Official Journal of the International Society for Magnetic Resonance in Medicine* 26.6 (2007), pp. 1572–1577.

[75] B. J. Soher, B. M. Dale, and E. M. Merkle. “A review of MR physics: 3T versus 1.5 T”. In: *Magnetic resonance imaging clinics of North America* 15.3 (2007), pp. 277–290.

[76] M. Gutberlet, B. Spors, M. Grothoff, P. Freyhardt, K. Schwinge, M. Plotkin, H. Amthauer, R. Noeske, and R. Felix. “Comparison of different cardiac MRI sequences at 1.5 T/3.0 T with respect to signal-to-noise and contrast-to-noise ratios-initial experience”. In: *RöFo-Fortschritte auf dem Gebiet der Röntgenstrahlen und der bildgebenden Verfahren*. Vol. 176. 06. © Georg Thieme Verlag KG Stuttgart· New York. 2004, pp. 801–808.

[77] C. M. Deniz. “Parallel transmission for ultrahigh field MRI”. In: *Topics in Magnetic Resonance Imaging* 28.3 (2019), pp. 159–171.

[78] W. M. Brink, V. Gulani, and A. G. Webb. “Clinical applications of dual-channel transmit MRI: A review”. In: *Journal of Magnetic Resonance Imaging* 42.4 (2015), pp. 855–869.

[79] L. L. Wald and E. Adalsteinsson. “Parallel transmit technology for high field MRI”. In: *Magnetom Flash* 40.1 (2009), p. 2009.

[80] S. N. Williams, P. McElhinney, and S. Gunamony. “Ultra-high field MRI: parallel-transmit arrays and RF pulse design”. In: *Physics in Medicine & Biology* 68.2 (2023), 02TR02.

[81] V. Vorobyev, A. Shchelokova, I. Zivkovic, A. Slobozhanyuk, J. D. Baena, J. P. Del Risco, R. Abdeddaim, A. Webb, and S. Glybovski. “An artificial dielectric slab for ultra high-field MRI: Proof of concept”. In: *Journal of Magnetic Resonance* 320 (2020), p. 106835.

[82] W. Teeuwisse, W. Brink, K. Haines, and A. Webb. “Simulations of high permittivity materials for 7 T neuroimaging and evaluation of a new barium titanate-based dielectric”. In: *Magnetic resonance in medicine* 67.4 (2012), pp. 912–918.

[83] A. G. Webb. “Dielectric materials in magnetic resonance”. In: *Concepts in magnetic resonance part A* 38.4 (2011), pp. 148–184.

[84] K. Koolstra, P. Börnert, W. Brink, and A. Webb. “Improved image quality and reduced power deposition in the spine at 3 T using extremely high permittivity materials”. In: *Magnetic resonance in medicine* 79.2 (2018), pp. 1192–1199.

[85] A. Webb, A. Shchelokova, A. Slobozhanyuk, I. Zivkovic, and R. Schmidt. “Novel materials in magnetic resonance imaging: high permittivity ceramics, metamaterials, metasurfaces and artificial dielectrics”. In: *Magnetic Resonance Materials in Physics, Biology and Medicine* 35.6 (2022), pp. 875–894.

[86] W. M. Brink, R. F. Remis, and A. G. Webb. “A theoretical approach based on electromagnetic scattering for analysing dielectric shimming in high-field MRI”. In: *Magnetic resonance in medicine* 75.5 (2016), pp. 2185–2194.

[87] W. M. Brink and A. G. Webb. “High permittivity pads reduce specific absorption rate, improve B1 homogeneity, and increase contrast-to-noise ratio for functional cardiac MRI at 3 T”. In: *Magnetic resonance in medicine* 71.4 (2014), pp. 1632–1640.

[88] P. de Heer, M. B. Bizino, M. J. Versluis, A. G. Webb, and H. J. Lamb. “Improved cardiac proton magnetic resonance spectroscopy at 3 T using high permittivity pads”. In: *Investigative radiology* 51.2 (2016), pp. 134–138.

[89] A. L. Neves, L. Leroi, Z. Raolison, N. Cochinaire, T. Letertre, R. Abdeddaïm, S. Enoch, J. Wenger, J. Berthelot, A.-L. Adenot-Engelvin, N. Malléjac, F. Mauconduit, A. Vignaud, and P. Sabouroux. “Compressed perovskite aqueous mixtures near their phase transitions show very high permittivities: New prospects for high-field MRI dielectric shimming”. In: *Magnetic resonance in medicine* (2018).

[90] K. Nehrke and P. Börnert. “DREAM—a novel approach for robust, ultrafast, multislice B1 mapping”. In: *Magnetic resonance in medicine* 68.5 (2012), pp. 1517–1526.

[91] P. S. Rahko. “Evaluation of the skin-to-heart distance in the standing adult by two-dimensional echocardiography”. In: *Journal of the American Society of Echocardiography* 21.6 (2008), pp. 761–764.

[92] P. S. Jacobs, N. E. Wilson, W. M. Brink, A. Swain, A. Hanumapur, N. Panchal, S. Mehta, M. A. Elliott, and R. Reddy. “Reduction of Radiofrequency Induced Heating around Passive Implants via Flexible Metasurface Shielding at 7T”. In: *Proceedings of the International Society for Magnetic Resonance in Medicine*. Vol. 1215. 2024.

[93] P. Šiurytė, J. Tourais, Y. Zhang, C. Coletti, C. van de Steeg-Henzen, S. Mandija, Q. Tao, M. Henningsson, and S. Weingärtner. “Preparation-based B [Formula: see text] mapping in the heart using Bloch-Siegert shifts”. In: *Magnetic resonance in medicine* (2024).

[94] W. M. Brink, R. F. Remis, and A. G. Webb. “Radiofrequency safety of high permittivity pads in MRI—Impact of insulation material”. In: *Magnetic resonance in medicine* 89.5 (2023), pp. 2109–2116.

[95] P. Kellman, A. E. Arai, E. R. McVeigh, and A. H. Aletras. “Phase-sensitive inversion recovery for detecting myocardial infarction using gadolinium-delayed hyperenhancement”. In: *Magnetic Resonance in Medicine: An Official Journal of the International Society for Magnetic Resonance in Medicine* 47.2 (2002), pp. 372–383.

[96] T. A. Basha, M. C. Tang, C. Tsao, C. M. Tschabrunn, E. Anter, W. J. Manning, and R. Nezafat. “Improved dark blood late gadolinium enhancement (DB-LGE) imaging using an optimized joint inversion preparation and T2 magnetization preparation”. In: *Magnetic Resonance in Medicine* 79.1 (2018), pp. 351–360.

[97] C.-Y. Liu, O. Wieben, J. H. Brittain, and S. B. Reeder. “Improved delayed enhanced myocardial imaging with T2-Prep inversion recovery magnetization preparation”. In: *Journal of Magnetic Resonance Imaging: An Official Journal of the International Society for Magnetic Resonance in Medicine* 28.5 (2008), pp. 1280–1286.

[98] H. W. Kim, W. G. Rehwald, E. R. Jenista, D. C. Wendell, P. Filev, L. van Assche, C. J. Jensen, M. A. Parker, E.-l. Chen, A. L. C. Crowley, *et al.* “Dark-blood delayed enhancement cardiac magnetic resonance of myocardial infarction”. In: *JACC: Cardiovascular Imaging* 11.12 (2018), pp. 1758–1769.

[99] A. S. Fahmy, U. Neisius, C. W. Tsao, S. Berg, E. Goddu, P. Pierce, T. A. Basha, L. Ngo, W. J. Manning, and R. Nezafat. “Gray blood late gadolinium enhancement cardiovascular magnetic resonance for improved detection of myocardial scar”. In: *Journal of Cardiovascular Magnetic Resonance* 20.1 (2018), p. 22.

[100] R. J. Holtackers, A. Chiribiri, T. Schneider, D. M. Higgins, and R. M. Botnar. “Dark-blood late gadolinium enhancement without additional magnetization preparation”. In: *Journal of Cardiovascular Magnetic Resonance* 19.1 (2016), p. 64.

[101] T. A. Basha, M. Akcakaya, C. Liew, C. W. Tsao, F. N. Delling, G. Addae, L. Ngo, W. J. Manning, and R. Nezafat. “Clinical performance of high-resolution late gadolinium enhancement imaging with compressed sensing”. In: *Journal of Magnetic Resonance Imaging* 46.6 (2017), pp. 1829–1838.

[102] M. Akçakaya, H. Rayatzadeh, T. A. Basha, S. N. Hong, R. H. Chan, K. V. Kissinger, T. H. Hauser, M. E. Josephson, W. J. Manning, and R. Nezafat. “Accelerated late gadolinium enhancement cardiac MR imaging with isotropic spatial resolution using compressed sensing: initial experience”. In: *Radiology* 264.3 (2012), pp. 691–699.

[103] H. El-Rewaidy, U. Neisius, J. Mancio, S. Kucukseymen, J. Rodriguez, A. Paskavitz, B. Menze, and R. Nezafat. “Deep complex convolutional network for fast reconstruction of 3D late gadolinium enhancement cardiac MRI”. In: *NMR in Biomedicine* 33.7 (2020), e4312.

[104] J. Uhlig, O. Al-Bourini, R. Salgado, M. Francone, R. Vliegenthart, J. Bremerich, J. Lotz, and M. Gutberlet. “Gadolinium-based contrast agents for cardiac MRI: use of linear and macrocyclic agents with associated safety profile from 154 779 European patients”. In: *Radiology: Cardiothoracic Imaging* 2.5 (2020), e200102.

[105] D. R. Messroghli, J. C. Moon, V. M. Ferreira, L. Grosse-Wortmann, T. He, P. Kellman, J. Mascherbauer, R. Nezafat, M. Salerno, E. B. Schelbert, *et al.* “Clinical recommendations for cardiovascular magnetic resonance mapping of T1, T2, T2* and extracellular volume: a consensus statement by the Society for Cardiovascular Magnetic Resonance (SCMR) endorsed by the European Association for Cardiovascular Imaging (EACVI)”. In: *Journal of Cardiovascular Magnetic Resonance* 19.1 (2016), p. 75.

[106] E. Aherne, K. Chow, and J. Carr. “Cardiac T1 mapping: techniques and applications”. In: *Journal of Magnetic Resonance Imaging* 51.5 (2020), pp. 1336–1356.

[107] D. R. Messroghli, A. Radjenovic, S. Kozerke, D. M. Higgins, M. U. Sivananthan, and J. P. Ridgway. “Modified Look-Locker inversion recovery (MOLLI) for high-resolution T1 mapping of the heart”. In: *Magnetic Resonance in Medicine: An Official Journal of the International Society for Magnetic Resonance in Medicine* 52.1 (2004), pp. 141–146.

[108] K. Chow, J. A. Flewitt, J. D. Green, J. J. Pagano, M. G. Friedrich, and R. B. Thompson. “Saturation recovery single-shot acquisition (SASHA) for myocardial T1 mapping”. In: *Magnetic resonance in medicine* 71.6 (2014), pp. 2082–2095.

[109] S. Weingärtner, M. Akçakaya, T. Basha, K. V. Kissinger, B. Goddu, S. Berg, W. J. Manning, and R. Nezafat. “Combined saturation/inversion recovery sequences for improved evaluation of scar and diffuse fibrosis in patients with arrhythmia or heart rate variability”. In: *Magnetic resonance in medicine* 71.3 (2014), pp. 1024–1034.

[110] S. Roujol, S. Weingärtner, M. Foppa, K. Chow, K. Kawaji, L. H. Ngo, P. Kellman, W. J. Manning, R. B. Thompson, and R. Nezafat. “Accuracy, precision, and reproducibility of four T1 mapping sequences: a head-to-head comparison of MOLLI, ShMOLLI, SASHA, and SAPPHIRE”. In: *Radiology* 272.3 (2014), pp. 683–689.

[111] P. Triadyaksa, M. Oudkerk, and P. E. Sijens. “Cardiac T2* mapping: Techniques and clinical applications”. In: *Journal of Magnetic Resonance Imaging* 52.5 (2020), pp. 1340–1351.

[112] P. Kellman, H. Xue, B. S. Spottiswoode, C. M. Sandino, M. S. Hansen, A. Abdel-Gadir, T. A. Treibel, S. Rosmini, C. Mancini, W. P. Bandettini, *et al.* “Free-breathing T2* mapping using respiratory motion corrected averaging”. In: *Journal of Cardiovascular Magnetic Resonance* 17.1 (2015), p. 3.

[113] T.-Y. Huang, Y.-J. Liu, A. Stemmer, and B. P. Poncelet. “T2 measurement of the human myocardium using a T2-prepared transient-state TrueFISP sequence”. In: *Magnetic Resonance in Medicine: An Official Journal of the International Society for Magnetic Resonance in Medicine* 57.5 (2007), pp. 960–966.

[114] S. Giri, Y.-C. Chung, A. Merchant, G. Mihai, S. Rajagopalan, S. V. Raman, and O. P. Simonetti. “T2 quantification for improved detection of myocardial edema”. In: *Journal of cardiovascular magnetic resonance* 11.1 (2009), p. 56.

[115] H. Ding, L. Fernandez-de-Manuel, M. Schär, K. H. Schuleri, H. Halperin, L. He, M. M. Zviman, R. Beinart, and D. A. Herzka. “Three-dimensional whole-heart T2 mapping at 3T”. In: *Magnetic resonance in medicine* 74.3 (2015), pp. 803–816.

[116] M. Akçakaya, T. A. Basha, S. Weingärtner, S. Roujol, S. Berg, and R. Nezafat. “Improved quantitative myocardial T2 mapping: Impact of the fitting model”. In: *Magnetic resonance in medicine* 74.1 (2015), pp. 93–105.

[117] A. M. Sprinkart, J. A. Luetkens, F. Träber, J. Doerner, J. Gieseke, B. Schnackenburg, G. Schmitz, D. Thomas, R. Homsi, W. Block, *et al.* “Gradient Spin Echo (GraSE) imaging for fast myocardial T2 mapping”. In: *Journal of Cardiovascular Magnetic Resonance* 17 (2015), pp. 1–9.

[118] R. B. Van Heeswijk, H. Feliciano, C. Bongard, G. Bonanno, S. Coppo, N. Lauriers, D. Locca, J. Schwitter, and M. Stuber. “Free-breathing 3 T magnetic resonance T2-mapping of the heart”. In: *JACC: Cardiovascular Imaging* 5.12 (2012), pp. 1231–1239.

[119] A. Bustin, A. Hua, G. Milotta, O. Jaubert, R. Hajhosseiny, T. F. Ismail, R. M. Botnar, and C. Prieto. “High-spatial-resolution 3D whole-heart MRI T2 mapping for assessment of myocarditis”. In: *Radiology* 298.3 (2021), pp. 578–586.

[120] T. A. Basha, S. Bellm, S. Roujol, S. Kato, and R. Nezafat. “Free-breathing slice-interleaved myocardial T2 mapping with slice-selective T2 magnetization preparation”. In: *Magnetic resonance in medicine* 76.2 (2016), pp. 555–565.

[121] U. Blume, T. Lockie, C. Stehning, S. Sinclair, S. Uribe, R. Razavi, and T. Schaeffter. “Interleaved T1 and T2 relaxation time mapping for cardiac applications”. In: *Journal of Magnetic Resonance Imaging: An Official Journal of the International Society for Magnetic Resonance in Medicine* 29.2 (2009), pp. 480–487.

[122] S. Kvernby, M. Warntjes, J. Engvall, C.-J. Carlhäll, and T. Ebbers. “Clinical feasibility of 3D-QALAS–Single breath-hold 3D myocardial T1-and T2-mapping”. In: *Magnetic resonance imaging* 38 (2017), pp. 13–20.

[123] M. Akçakaya, S. Weingärtner, T. A. Basha, S. Roujol, S. Bellm, and R. Nezafat. “Joint myocardial T1 and T2 mapping using a combination of saturation recovery and T2-preparation”. In: *Magnetic resonance in medicine* 76.3 (2016), pp. 888–896.

[124] R. Guo, X. Cai, S. Kucukseymen, J. Rodriguez, A. Paskavitz, P. Pierce, B. Goddu, R. B. Thompson, and R. Nezafat. “Free-breathing simultaneous myocardial T1 and T2 mapping with whole left ventricle coverage”. In: *Magnetic Resonance in Medicine* 85.3 (2021), pp. 1308–1321.

[125] Y. Liu, J. Hamilton, S. Rajagopalan, and N. Seiberlich. “Cardiac magnetic resonance fingerprinting: technical overview and initial results”. In: *JACC: Cardiovascular Imaging* 11.12 (2018), pp. 1837–1853.

[126] A. G. Christodoulou, J. L. Shaw, C. Nguyen, Q. Yang, Y. Xie, N. Wang, and D. Li. “Magnetic resonance multitasking for motion-resolved quantitative cardiovascular imaging”. In: *Nature biomedical engineering* 2.4 (2018), pp. 215–226.

[127] H.-S. N. Musthafa, G. Dragneva, L. Lottonen, M. Merentie, L. Petrov, T. Heikura, E. Ylä-Herttuala, S. Ylä-Herttuala, O. Gröhn, and T. Liimatainen. “Longitudinal rotating frame relaxation time measurements in infarcted mouse myocardium in vivo”. In: *Magnetic resonance in medicine* 69.5 (2013), pp. 1389–1395.

[128] Z. Zhou, C. Nguyen, Y. Chen, J. L. Shaw, Z. Deng, Y. Xie, J. Dawkins, E. Marbán, and D. Li. “Optimized CEST cardiovascular magnetic resonance for assessment of metabolic activity in the heart”. In: *Journal of cardiovascular magnetic resonance* 19 (2017), pp. 1–7.

[129] P. S. Rajiah, C. J. François, and T. Leiner. “Cardiac MRI: state of the art”. In: *Radiology* 307.3 (2023), e223008.

[130] C. M. Kramer, J. Barkhausen, C. Bucciarelli-Ducci, S. D. Flamm, R. J. Kim, and E. Nagel. “Standardized cardiovascular magnetic resonance imaging (CMR) protocols: 2020 update”. In: *Journal of Cardiovascular Magnetic Resonance* 22.1 (2020), pp. 1–18.

[131] H. Wen, T. Denison, R. Singerman, and R. Balaban. “The intrinsic signal-to-noise ratio in human cardiac imaging at 1.5, 3, and 4 T”. In: *Journal of magnetic resonance* 125.1 (1997), pp. 65–71.

[132] O. Wieben, C. Francois, and S. B. Reeder. “Cardiac MRI of ischemic heart disease at 3 T: potential and challenges”. In: *European journal of radiology* 65.1 (2008), pp. 15–28.

[133] R. L. Greenman, J. E. Shirosky, R. V. Mulkern, and N. M. Rofsky. “Double inversion black-blood fast spin-echo imaging of the human heart: a comparison between 1.5 T and 3.0 T”. In: *Journal of Magnetic Resonance Imaging* 17.6 (2003), pp. 648–655.

[134] G. Buonincontri and S. J. Sawiak. “MR fingerprinting with simultaneous B1 estimation”. In: *Magnetic resonance in medicine* 76.4 (2016), pp. 1127–1135.

[135] M. Boudreau, C. L. Tardif, N. Stikov, J. G. Sled, W. Lee, and G. B. Pike. “B1 mapping for bias-correction in quantitative T1 imaging of the brain at 3T using standard pulse sequences”. In: *Journal of magnetic resonance imaging* 46.6 (2017), pp. 1673–1682.

[136] C. H. Cunningham, J. M. Pauly, and K. S. Nayak. “Saturated double-angle method for rapid B1+ mapping”. In: *Magnetic Resonance in Medicine: An Official Journal of the International Society for Magnetic Resonance in Medicine* 55.6 (2006), pp. 1326–1333.

[137] W. T. Clarke, M. D. Robson, and C. T. Rodgers. “Bloch-Siegert-mapping for human cardiac 31P-MRS at 7 Tesla”. In: *Magnetic resonance in medicine* 76.4 (2016), pp. 1047–1058.

[138] S. Weingärtner, F. Zimmer, G. J. Metzger, K. Uğurbil, P.-F. Van de Moortele, and M. Akçakaya. “Motion-robust cardiac mapping at 3T using interleaved Bloch-Siegert shifts”. In: *Magnetic resonance in medicine* 78.2 (2017), pp. 670–677.

[139] L. I. Sacolick, F. Wiesinger, I. Hancu, and M. W. Vogel. “B1 mapping by Bloch-Siegert shift”. In: *Magnetic resonance in medicine* 63.5 (2010), pp. 1315–1322.

[140] S. Chung, D. Kim, E. Breton, and L. Axel. “Rapid B1+ mapping using a preconditioning RF pulse with TurboFLASH readout”. In: *Magnetic resonance in medicine* 64.2 (2010), pp. 439–446.

[141] K. Nehrke and P. Börnert. *Fast B1 mapping using a STEAM-based Bloch-Siegert preparation pulse*. 2011.

[142] J. L. Kent, I. Dragonu, L. Valkovič, and A. T. Hess. “Rapid 3D absolute B1+ mapping using a sandwiched train presaturated TurboFLASH sequence at 7 T for the brain and heart”. In: *Magnetic Resonance in Medicine* 89.3 (2023), pp. 964–976.

[143] R. J. Ogg, R. Kingsley, and J. S. Taylor. “WET, a T1-and B1-insensitive water-suppression method for in vivo localized 1H NMR spectroscopy”. In: *Journal of Magnetic Resonance, Series B* 104.1 (1994), pp. 1–10.

[144] A. Tannús and M. Garwood. “Adiabatic pulses”. In: *NMR in Biomedicine: An International Journal Devoted to the Development and Application of Magnetic Resonance In Vivo* 10.8 (1997), pp. 423–434.

[145] D. Idiyatullin, C. Corum, S. Moeller, and M. Garwood. “Gapped pulses for frequency-swept MRI”. In: *Journal of Magnetic Resonance* 193.2 (2008), pp. 267–273.

[146] G. Captur, P. Gatehouse, K. E. Keenan, F. G. Heslinga, R. Bruehl, M. Prothmann, M. J. Graves, R. J. Eames, C. Torlasco, G. Benedetti, *et al.* “A medical device-grade T1 and ECV phantom for global T1 mapping quality assurance—the T1 Mapping and ECV Standardization in cardiovascular magnetic resonance (T1MES) program”. In: *Journal of Cardiovascular Magnetic Resonance* 18.1 (2016), p. 58.

[147] Q. Tao, P. van der Tol, F. F. Berendsen, E. H. Paiman, H. J. Lamb, and R. J. van der Geest. “Robust motion correction for myocardial T1 and extracellular volume mapping by principle component analysis-based groupwise image registration”. In: *Journal of Magnetic Resonance Imaging* 47.5 (2018), pp. 1397–1405.

[148] J. Liu, Y. Wang, U. Katscher, and B. He. “Electrical properties tomography based on B1 maps in MRI: principles, applications, and challenges”. In: *IEEE Transactions on Biomedical Engineering* 64.11 (2017), pp. 2515–2530.

[149] P. Šiurytė, M. Henningsson, C. Coletti, C. van de Steeg-Henzen, and S. Weingärtner. “|B1+|-prepared imaging for efficient cardiac transmit field mapping”. In: *Proc. ISMRM 2023;* 2023.

[150] A. L. van Lier, A. Raaijmakers, T. Voigt, J. J. Lagendijk, P. R. Luijten, U. Katscher, and C. A. van den Berg. “Electrical properties tomography in the human brain at 1.5, 3, and 7T: a comparison study”. In: *Magnetic resonance in medicine* 71.1 (2014), pp. 354–363.

[151] A. Karsa and K. Shmueli. “New approaches for simultaneous noise suppression and edge preservation to achieve accurate quantitative conductivity mapping in noisy images”. In: *Proceedings of the International Society for Magnetic Resonance in Medicine*. Vol. 3774. 2021.

[152] A. Stogryn. “Equations for calculating the dielectric constant of saline water (correspondence)”. In: *IEEE transactions on microwave theory and Techniques* 19.8 (1971), pp. 733–736.

[153] L. Anderson, S. Holden, B. Davis, E. Prescott, C. Charrier, N. Bunce, D. Firmin, B. Wonke, J. Porter, J. Walker, *et al.* “Cardiovascular T2-star (T2*) magnetic resonance for the early diagnosis of myocardial iron overload”. In: *European heart journal* 22.23 (2001), pp. 2171–2179.

[154] T. Emrich, V. Bordonaro, U. J. Schoepf, A. Petrescu, G. Young, M. Halfmann, T. Schoeler, J. Decker, I. Abidoye, A. L. Emrich, *et al.* “Right/left ventricular blood pool T2 ratio as an innovative cardiac MRI screening tool for the Identification of left-to-right shunts in patients with right ventricular disease”. In: *Journal of Magnetic Resonance Imaging* 55.5 (2022), pp. 1452–1458.

[155] P. Triadyaksa, M. Oudkerk, and P. E. Sijens. “Cardiac T2* mapping: Techniques and clinical applications”. In: *Journal of Magnetic Resonance Imaging* 52.5 (2020), pp. 1340–1351.

[156] J. Zapp, S. Domsch, S. Weingärtner, and L. R. Schad. “Gaussian signal relaxation around spin echoes: Implications for precise reversible transverse relaxation quantification of pulmonary tissue at 1.5 and 3 Tesla”. In: *Magnetic Resonance in Medicine* 77.5 (2017), pp. 1938–1945.

[157] Y. Zhao, C. Yang, A. Schweidtmann, and Q. Tao. “Efficient Bayesian uncertainty estimation for nnU-Net”. In: *International Conference on Medical Image Computing and Computer-Assisted Intervention*. Springer. 2022, pp. 535–544.

[158] A. Bustin, W. R. Witschey, R. B. van Heeswijk, H. Cochet, and M. Stuber. “Magnetic resonance myocardial T1ρ mapping: Technical overview, challenges, emerging developments, and clinical applications”. In: *Journal of Cardiovascular Magnetic Resonance* 25.1 (2023), p. 34.

[159] M. Gram, T. Williams, P. Albertova, P. Jakob, B. Gerull, W. Bauer, P. Nordbeck, and M. Christa. “T1rho and T2rho based myocardial tissue characterisation in small animals at high-field MRI”. In: *European Heart Journal* 44.Supplement_2 (2023), ehad655–163.

[160] K. López, R. Neji, R. K. Mukherjee, J. Whitaker, A. Phinikaridou, R. Razavi, C. Prieto, S. Roujol, and R. Botnar. “Contrast-free high-resolution 3D magnetization transfer imaging for simultaneous myocardial scar and cardiac vein visualization”. In: *Magnetic Resonance Materials in Physics, Biology and Medicine* (2020), pp. 1–14.

[161] K. López, R. Neji, A. Bustin, I. Rashid, R. Hajhosseiny, S. J. Malik, R. P. A. G. Teixeira, R. Razavi, C. Prieto, S. Roujol, and R. M. Botnar. “Quantitative magnetization transfer imaging for non-contrast enhanced detection of myocardial fibrosis”. In: *Magnetic Resonance in Medicine* 85.4 (2021), pp. 2069–2083.

[162] Z. Zhou, C. Nguyen, Y. Chen, J. L. Shaw, Z. Deng, Y. Xie, J. Dawkins, E. Marbán, and D. Li. “Optimized CEST cardiovascular magnetic resonance for assessment of metabolic activity in the heart”. In: *Journal of cardiovascular magnetic resonance* 19.1 (2017), pp. 1–7.

[163] E. Versteeg, D. W. Klomp, and J. C. Siero. “A silent gradient axis for soundless spatial encoding to enable fast and quiet brain imaging”. In: *Magnetic Resonance in Medicine* 87.2 (2022), pp. 1062–1073.

[164] N. Boulant, S. Ma, E. Walker, A. Beckett, A. T. Vu, S. Gunamony, and D. A. Feinberg. “Acoustic noise reduction in the NexGen 7 T scanner”. In: *Magnetic Resonance in Medicine* (2024).

[165] Z. Zhou, A. Alfayad, T. C. Chao, and J. G. Pipe. “Acoustic noise reduction for spiral MRI by gradient derating”. In: *Magnetic Resonance in Medicine* 90.4 (2023), pp. 1547–1554.

[166] Y. Wang, P. Xu, J. Zeng, J. Zhang, Y. Zhu, S. Che, C. Yao, Y. Ge, and C. Wang. “Sequence optimization for MRI acoustic noise reduction”. In: *Journal of Physics: Conference Series*. Vol. 2591. 1. IOP Publishing. 2023, p. 012034.

[167] T. Yamashiro, Y. Takatsu, K. Morita, M. Nakamura, Y. Yukimura, and K. Nakajima. “Effect of acoustic noise reduction technology on image quality: a multivendor study”. In: *Radiological Physics and Technology* 16.2 (2023), pp. 235–243.

[168] S. N. Williams, P. McElhinney, and S. Gunamony. “Ultra-high field MRI: parallel-transmit arrays and RF pulse design”. In: *Physics in Medicine & Biology* 68.2 (2023), 02TR02.

[169] P. S. Jacobs, W. Brink, and R. Reddy. “A review of recent developments and applications of high-permittivity dielectric shimming in magnetic resonance”. In: *NMR in Biomedicine* 37.4 (2024), e5094.

[170] W. M. Brink, V. Gulani, and A. G. Webb. “Clinical applications of dual-channel transmit MRI: A review”. In: *Journal of Magnetic Resonance Imaging* 42.4 (2015), pp. 855–869.

[171] B. A. Runderkamp, T. Roos, W. van der Zwaag, G. J. Strijkers, M. W. Caan, and A. J. Nederveen. “Whole-liver flip-angle shimming at 7 T using parallel-transmit k T-point pulses and Fourier phase-encoded DREAM B 1+ mapping”. In: *Magnetic resonance in medicine* 91.1 (2024), pp. 75–90.

[172] J. L. Kent, M. H. de Buck, I. Dragonu, M. Chiew, L. Valkovič, and A. T. Hess. “Accelerated 3D multi-channel B1+ mapping at 7 T for the brain and heart”. In: *Magnetic Resonance in Medicine* (2024).

[173] N. Egger, S. Nagelstraßer, S. Wildenberg, A. Bitz, L. Ruck, J. Herrler, C. Meixner, R. Kimmlingen, T. Lanz, S. Schmitter, *et al.* “Accelerated B1+ mapping and robust parallel transmit pulse design for heart and prostate imaging at 7 T.” In: *Magnetic Resonance in Medicine* (2024).

[174] C. Z. Cooley, P. C. McDaniel, J. P. Stockmann, S. A. Srinivas, S. F. Cauley, M. Śliwiak, C. R. Sappo, C. F. Vaughn, B. Guerin, M. S. Rosen, *et al.* “A portable scanner for magnetic resonance imaging of the brain”. In: *Nature biomedical engineering* 5.3 (2021), pp. 229–239.

[175] Y. Zhao, Y. Ding, V. Lau, C. Man, S. Su, L. Xiao, A. T. Leong, and E. X. Wu. “Whole-body magnetic resonance imaging at 0.05 Tesla”. In: *Science* 384.6696 (2024), eadm7168.

[176] A. E. Campbell-Washburn, J. Varghese, K. S. Nayak, R. Ramasawmy, and O. P. Simonetti. “Cardiac MRI at low field strengths”. In: *Journal of Magnetic Resonance Imaging* 59.2 (2024), pp. 412–430.

[177] A. Sahu, H. Vikas, and N. Sharma. “Life cycle costing of MRI machine at a tertiary care teaching hospital”. In: *Indian Journal of Radiology and Imaging* 30.02 (2020), pp. 190–194.

[178] T. Meerbothe, K.-J. Jung, C. Cui, D.-H. Kim, C. van den Berg, and S. Mandija. “2D vs 3D Electrical Properties Tomography reconstruction: The impact of disregarding the third dimension”. In: *Proceedings of the International Society for Magnetic Resonance in Medicine*. Vol. 3684. 2024.

ACKNOWLEDGEMENTS

While research during the PhD journey is largely individual, it would not have been the same without many wonderful people that have been there along the way. These years have been truly formative to me, and I would like to sincerely thank everyone who has been a part of them.

Firstly, I would like to thank my mentors. When looking for advice on where to do my PhD, the main comment I kept hearing is 'if you have a great supervisor, it is likely that you will have a great overall experience'. To my supervisor and co-promotor **Sebastian**, thank you for inviting me to be a part of a brand new lab, and to help build it over the years by performing incredible research and by forming a closely-knit team. You have an incredible talent to inspire others to use curiosity and excitement for research as an endless fuel for daily hard work. Your guidance through these years has greatly contributed to my growth. Needless to say, I am happy that I took the advice during my PhD search. To my promotor **Frans**, thank you for your continuous support throughout the years, for always having a kind word and being there during the biggest moments. Your advice, positivity and encouragement helped me feel at home when I moved in to a new country.

Next, I cannot understate how blessed I was to share my daily struggles with the wonderful MarsLab team. **Chiara**, **Maša** and **Ayda**, thank you for being there from (mostly) the very beginning until the end. The last five years have been a rollercoaster full of hard work, self doubt, wins and many setbacks, but we were always together in this ride, lifting up each other. You have grown to be like 'PhD sisters' to me, and you all inspire me as incredibly intelligent, funny and warm people. Chiara and Maša, I am sorry that I chose a defence date for which you are both unavailable, and I request a proper celebration once you are both back. Ayda, thank you for the warmest friendship through the years, your kindness and dedication have brightened up many hard days and I am honored to have you as my paranymph. To **Martina**, for your bright and friendly presence, and for always being there for a chat. While you have only started one year ago, I cannot imagine the lab without you. To **Joao**, another 'first generation' MarsLab member, thank you for incredibly sober and stable presence in our chaos, and for continuous support when I started navigating the world of MRI. It has always been a pleasure working with you. **Berat** and **Niccolò**, I am very happy to have met you as the 'MarsLab 2.0' members before leaving.

It is especially satisfying to see you take over the previous research, to know that it does not simply end with the first generation, but continues on. I wish you all the best during your own journeys. To the students I have supervised, **Robert**, **Jasper** and **Friso**, thank you for building a relatively challenging project from the ground up. Considering that none of us in the lab were experts in building MR-compatible devices or setting up electromagnetic field simulations, you have shown an incredible independence and perseverance in your daily work.

The research in TU Delft was never constrained to the bounds of the lab. Many people on the way have contributed to the work in this book. First and foremost, I would like to acknowledge **Christal**, who has supported our MRI research in Holland PTC every week by arranging the volunteer scans and by scouring the schedule for extra scanning time when we were close to deadlines. I thank you also for making long scanning days even more enjoyable by your company. Additionally, I thank **Christal**, **Paul** and **Patricia** for the ongoing technical support, patience with setting up the experiments, and for going along with the strangest requests like bringing a garden hose or a ballistic gel torso inside the MRI room. To everyone in the ImPhys department, thank you for presence and support. **Henry**, thank you for universal help with various technical requests and particularly for your input in designing the noise cancelling setup. **Angela**, **Annelies** and **Ronald**, thank you for the help with a large variety of administrative and technical matters, and for numerous small chats on the hallway. To **Qian**, **Yi** and **Yidong**, for beating the cardiac motion with your amazing registration methods. To **Eric**, for invaluable early input in pneumatic headphone model design and frequency level equalization.

Additionally, I thank the PIs who were not directly involved in my research - **David**, **Eric**, **Guillaume**, **Rik**, **Miriam**, **Bernd**, **Martin** and **Sjoerd** - for contributing to my development as a researcher. To the special "Beach people" who never go to the beach - **Agis**, **Djalma**, **Eszter**, **Jazmine**, **Ilaria**, **Chih-Hsien**, **Rick**, **Fabian**, **Dion**, **Gabrielle**, **Eleonora**, **Hugues**, **Moein**, **Xiufeng**, **Jack**, **Lorenzo** and **Liam** - thank you for charging my social battery during drinks, board game nights, and, that one time, a beach trip.

Lastly, I would like to acknowledge my family and friends, who are an unwavering pillar I can rely on. **Victor**, my love and life partner, I am deeply grateful for your support through these years. From being my audience during the PhD interview presentation practice, and continuous scientific discussions as a fellow physicist, to your incredible warmth and patience while I would be a big ball of PhD stress. I feel truly blessed to share my life with you, and I cannot wait to see what the next chapter has in store for us. **Aistė** and **Evelina**, I thank you for over two decades of friendship that cannot be diminished by time or space. While we continued to grow as people, we did not outgrow each

other. Thank you for keeping the mutual feeling of responsibility to be there for each other. **Aurelija**, thank you for many shared memories when we found ourselves "reunited" in the Netherlands. You made this country feel more like home from day one. **Lukas** and **Rytis**, thank you for the high quality uplifting content in group chats, shared laughs, fun parties and the Slovakia trip. To **Odile**, thank you for being incredibly supportive and welcoming. And to my cat, **Naga**, thank you for being a great therapist and for showing me how to rest.

To my godmother **Birutė**, *ačiū už nuolatinį palaikymą ir paskatinimą. Tu buvai šalia pačiais svarbiausiais mano gyvenimo momentais, ir aš esu už tai be galo dėkinga*. To my sister **Aidana**, thank you for continuously investing in our relationship while being miles away. Your support and encouragement have always helped me to recognize when I can do better, and when I should slow down and take better care of myself. I am honored to have you as my second paranymph. To my **dad**, *tete, ačiū tau už tuos skambučius, kai man reikėjo patarimo, kaip konstruoti garsiakalbius. Ačiū už palaikymą pakeliui, ir už paveldėtą polinkį konstruoti, spręsti problemas ir nepasiduoti.* To my **mum**, thank you for nudging me to look for opportunities to challenge myself from early on in life. You and Aidana have always set a great example by learning new things continuously and bravely doing whatever you set out to do. Finally, thank you for that beautiful moment 30 minutes before I officially submitted my thesis, when you, Aidana and Victor walked in quietly and ceremoniously with coffee and blueberry cake, giving a me big warm hug.

CURRICULUM VITæ

Paulina Šiurytė

RESEARCH

MARS LAB (TU DELFT, NETHERLANDS) - 2020–2024

PhD thesis	Acoustic and Electromagnetic Waves in MRI: Novel Strategies for Acoustic Noise Reduction, Transmit Field Characterization and Correction
Research	Novel methods for MRI acoustic noise reduction, B_1^+ field characterization and correction, pulse sequence development for quantitative biomarkers
Awards	ISMRM, 2034 and 2024 – Travel stipend award ; ISMRM, 2023 – Summa Cum Laude Merit Awar, Shark Tank winner (Predictive Noise Canceling) ESMRMB, 2021 - Registration award

TRIUMF (VANCOUVER, CANADA) - 2018

Master's thesis	Coulomb Excitation Study of Neutron-Deficient Erbium Isotopes
Research	Supporting Gamma-Ray Spectroscopy Group by contributing to daily laboratory work or working on shifts during beam-time.

EDUCATION

UNIVERSITY OF SURREY (GUILDFORD, UK) - 2015–2019

MPhys course	Obtained Master's degree in Physics with 1st class honours
Laboratory prize	Best performance in laboratory work at level 5 of the Physics undergraduate programmes

OLDTOWN GYMNASIUM (JONAVA, LITHUANIA) - 2011–2015

Exams passed	Physics (100/100), Mathematics (100/100), Lithuanian Language and Literature (82/100), English Language (100/100)
Academic award	Awarded by Lithuanian Prime Minister as an outstanding student in 2015

NATIONAL STUDENT ACADEMY (LITHUANIA) - 2009–2014

Advanced education	Supplementary education in advanced levels of mathematics, physics and astronomy

LIST OF PUBLICATIONS

JOURNAL PAPERS

1. **P. Šiurytė** , J. Tourais, Y. Zhang, C. Coletti, C. van de Steeg-Henzen, S.Mandija, Q. Tao, M. Henningsson and S. Weingärtner, 2024. Preparation-based B_1^+ mapping in the heart using Bloch–Siegert shifts. Magnetic Resonance in Medicine, 92(6), pp.2596-2606.

2. R. Guo, S. Weingärtner, **P. Šiurytė**, C. T. Stoeck, M. Füetterer, A. E. Campbell-Washburn, A. Suinesiaputra, M. Jerosch-Herold and R. Nezafat, 2022. Emerging techniques in cardiac magnetic resonance imaging. Journal of Magnetic Resonance Imaging, 55(4), pp.1043-1059.

3. S. A. Gillespie, J. Henderson, K. Abrahams, F. A. Ali,L. Atar, G. C. Ball, N, Bernier, S.S. Bhattcharjee, R. Caballero-Folch, M. Bowry, A. Chester, R. Coleman, T. Drake, E. Dunling, A. B. Garnsworthy, B. Greaves, G. F. Grinyer, G. Hackman, E. Kasanda, R. LaFleur, S. Masango, D. Muecher, C. Ngwetsheni, S. S. Ntshangase, B. Olaizola,J. N. Orce, T. Rockman, Y. Saito,L. Sexton, **P. Šiurytė** , J. Smallcombe,J. K. Smith,C. E. Svensson, E. Timakova, R. Wadsworth, J. Williams, M. S. C. Winokan, C. Y. Wu and T. Zidar, 2021. Coulomb excitation of Kr 80, 82 and a change in structure approaching N= Z= 40. Physical Review C, 104(4), p.044313.

4. J. Williams, C. Andreoiu, G.C. Ball, N. Bernier, M. Bowry, S.S. Bhattacharjee, C. Burbadge, R. Caballero-Folch, A. Chester, F.H. Garcia, A.B. Garnsworthy, S.A. Gillespie, G. Hackman, R. Henderson, B. Jigmeddorj, C. Jones, P. Kowalski, R. Lafleur, A.D. MacLean, M. Morrison, B. Olaizola, Y. Saito, L. Sexton, **P. Šiurytė**, J. Smallcombe, K. Starosta, C.E. Svensson, M. Spencer, E. Timakova, K. Van Wieren, P. Voss, M. Winokan, F. Wu, 2019. The CsI ball ancillary detector array for TIP and TIGRESS at TRIUMF. Nuclear Instruments and Methods in Physics Research Section A: Accelerators, Spectrometers, Detectors and Associated Equipment, 939, pp.1-9.

5. Y. Ayyad,B. Olaizola,W. Mittig,G. Potel,V. Zelevinsky,M. Horoi, S. Beceiro-Novo, M. Alcorta,C. Andreoiu,T. Ahn, M. Anholm, L. Atar, A. Babu, D. Bazin, N. Bernier, S. S. Bhattacharjee, M. Bowry, R. Caballero-Folch, M. Cortesi, C. Dalitz, E. Dunling, A. B. Garnsworthy, M. Holl, B. Kootte, K. G. Leach, J. S. Randhawa, Y. Saito, C. Santamaria, **P. Šiurytė**, C.E. Svensson, R. Umashankar, N. Watwood, and D. Yates, 2019. Direct observation of proton emission in be 11. Physical Review Letters, 123(8), p.082501.

PRE-PRINTS

1. **P. Šiurytė**, R. van de Velde, J. van Leeuwen, O. C. Akgun, W. Brink and S. Weingärtner, 2024. Adaptive Radiofrequency Shimming in MRI using Reconfigurable Dielectric Materials. arXiv preprint arXiv:2410.01501.

2. **P. Šiurytė** and S. Weingärtner, 2024. Lowering The Acoustic Noise Burden in MRI with Predictive Noise Canceling. medRxiv, pp.2024-04.

PATENTS

1. O.C. Akgün, S. Weingärtner, and **P. Šiurytė**, 2023. Shim for mitigating effects of field Inhomogeneities in magnetic resonance Imaging and method thereof.

2. S. Weingärtner, **P. Šiurytė** and J. Tourais, Technische Universiteit Delft, 2024. Method and apparatus for magnetic resonance imaging. U.S. Patent Application 18/250,370.

CONFERENCE PAPERS AND ABSTRACTS

1. **P. Šiurytė**, J. Tourais, and S. Weingärtner. "Improving Patient Comfort in MRI with Predictive Acoustic Noise Cancelling". In: 2022 44th Annual International Conference of the IEEE Engineering in Medicine and Biology Society (EMBC). IEEE. 2022, pp. 1468–1471.

2. **P. Šiurytė**, T. Meerbothe, Y. Zhang, M. Henningson, J. Tourais, C. van de Steeg-Henzen, Q. Tao, S. Mandija and S. Weingärtner. "Complex B_1^+ field-based conductivity mapping in the human myocardium at 3T". In: Proc. ISMRM 2024; ISMRM Benelux 2024. 2024.

3. R. van de Velde, **P. Šiurytė**, J. van Leeuwen, W. Brink and S. Weingärtner. "Feasibility of active B1+ shimming using remote switching of coupled dielectric pads". In: Proc. ISMRM 2024; ISMRM Benelux 2024. 2024.

4. **P. Šiurytė**, J. Tourais, Y. Zhao, C. van de Steeg-Henzen, Q. Tao, S. Weingärtner and M. Henningsson. "Robust cardiac T_2^* mapping using RF phase-cycled transverse-magnetization decay preparations". In: Proc. Proc. SCMR 2024. 2024.

5. **P. Šiurytė**, M. Henningsson, C. Coletti, C. van de Steeg-Henzen, and S. Weingärtner. "B_1^+-prepared imaging for efficient cardiac transmit field mapping". In: Proc. ISMRM 2023. 2023.

6. **P. Šiurytė**, F. de Boer, C. Akgun and S. Weingärtner. "Actively coupled dielectric pads for adaptive B_1^+ field shimming". In: Proc. ISMRM 2022. 2022.

7. **P. Šiurytė**, J. Tourais and S. Weingärtner. "Reducing MRI acoustic noise burden with Predictive Noise Cancelling". In: Proc. ISMRM 2022; ISMRM Benelux 2022. 2022.

8. **P. Šiurytė**, J. Tourais and S. Weingärtner. “MRI Acoustic Noise: Limits of the Linear Time-Independent Model”. In: Proc. ESMRMB 2021. 2021.

Invitation

To attend the public defence of the thesis

Acoustic and Electromagnetic Waves in MRI:

Novel Strategies for Acoustic Noise Reduction, Transmit Field Characterization and Correction

by

Paulina Šiurytė

Thursday, January 9th, 2025,
in the Senate Hall, Aula
Conference Center, TU Delft

9:30 AM Layman's talk
10:00 AM Public defence

Paranymphs

Ayda Arami
Aidana Šiurytė

Propositions

accompanying the dissertation

Acoustic and Electromagnetic Waves in MRI

Novel Strategies for Acoustic Noise Reduction, Transmit Field Characterization and Correction

by

Paulina ŠIURYTĖ

1. With current measurement techniques, it is possible to acquire cardiac B_1^+ maps that enable the extraction of electrical properties with the quality needed to distinguish healthy and diseased tissue. (This thesis)
2. Implementing Predictive Noise Canceling will increase the patient acceptance rates of MRI. (This thesis)
3. The remote coupling of dielectric pads can be used instead of multi-transmit coils to enable high-field body MRI. (This thesis)
4. As long as 90% female lab raises more comments of surprise than 90% male lab, there is prevailing gender bias.
5. The most cost-effective and customizable building blocks for MRI-compatible noise-canceling equipment are wall cabinets and garden hoses, as available in IKEA, for instance.
6. Questions that can't be answered inspire more creativity than answers that can't be questioned (inspired by Richard Feynman).
7. A purely hectic rush only reproduces and compounds what is already available. (inspired by Byung-Chul Han, 'The Burnout Society')
8. Curiosity is the main driver of scientific progress.
9. The use of digital media led to more social connection than isolation during the Covid-19 pandemic.
10. The world is a dangerous place, not because of those who do evil, but because of those who look on and do nothing. (inspired by Sam Esmail, 'Mr. Robot')

These propositions are regarded as opposable and defendable, and have been approved as such by the promotor Prof. dr. F.M. Vos.